Master's Thesis

AdS/CFT Introduction & Properties of Anti-de Sitter Black Holes: Quasinormal Mode Calculation in Various Black Hole Models

Santanu Pradhan

AdS/CFT Introduction & Properties of Anti-de Sitter Black Holes: Quasinormal Mode Calculation in Various Black Hole Models

A thesis submitted in
partial fulfillment of the requirements
for the award of the degree

of

Master of Science

by

Santanu Pradhan

Under the supervision of

Dr. Manavendra Mahato

DEPARTMENT OF PHYSICS
INDIAN INSTITUTE OF TECHNOLOGY INDORE
INDORE - 452020, INDIA
May 2024

©2024 Santanu Pradhan. All rights reserved.

Dedicated to,

My beloved family, without whose endless love and support, I could not achieve this.

भौतिकी विभाग / Department of Physics
भारतीय प्रौद्योगिकी संस्थान इंदौर / Indian Institute of Technology Indore
इंदौर-452020 / Indore–452020, सिमरोल / Simrol, एमपी, भारत / MP, India

CERTIFICATE

This is to certify that the thesis entitled "**AdS/CFT Introduction & Properties of Anti-de Sitter Black Holes: Quasinormal Mode Calculation in Various Black Hole Models**", submitted by **Santanu Pradhan** to **Indian Institute of Technology Indore**, is a record of bona fide and authentic research work carried out during the time period from June 2023 to June 2024 under my supervision and guidance. I consider it worthy of consideration for the award of the degree of *Master of Science* of the Institute.

Date: 13/05/2024
Place: Indore

Dr. Manavendra Mahato
(Supervisor)
Designation
Department of Physics
Indian Institute of Technology Indore
Indore, India

Name: Dr. Manavendra N Mahato
(Convener, DPGC)
Designation
Department of Physics
Indian Institute of Technology Indore
Indore, India

DECLARATION

I certify that

a. The content presented in this thesis is entirely original and has been personally undertaken by me, under the overall guidance of my supervisor.

b. The work has not been presented to any other institution in pursuit of any academic degree or diploma.

c. I have adhered to the instructions and guidelines outlined by the institution while composing this thesis.

d. I have abided by the standards and regulations stipulated in the ethical code of conduct established by the institution.

e. Whenever I've incorporated materials such as data, theoretical analysis, or text from external sources, proper acknowledgment has been provided through citations within the thesis text, accompanied by detailed references.

f. Whenever I've directly quoted written materials sourced from external references, I've enclosed them within quotation marks and appropriately attributed them by citing the sources and providing comprehensive details in the reference section.

Santanu Pradhan

Date: 13/05/2024
Place: IIT INDORE

Santanu Pradhan
Roll No.: 2203151019

Acknowledgements

Acknowledgments:

I extend my heartfelt appreciation to all those who contributed to the successful completion of this project. Foremost, I am immensely grateful to Manav Sir at IIT Indore for their invaluable vision, guidance, and unwavering support throughout this endeavor.

I am also indebted to my dear friend for their consistent encouragement and dedication. Lastly, I extend my thanks to the Indian Institute of Technology Indore for furnishing the essential resources and infrastructure that enabled me to execute this project to the best of my capacity.

Santanu Pradhan

Date: 13/05/2024
Place: IIT INDORE

Santanu Pradhan
Roll No.: 2203151019

Abstract

This thesis delves into a comprehensive study of Anti-de Sitter (AdS) black holes, focusing on their properties and calculation of Quasi Normal Frequencies of various black holes. Beginning with a thorough exploration of black hole physics, including the holographic principle, large N expansion of gauge theories, and string theory. I reviewed the QCD connection to string theory and the Physics of D branes. I derive the AdS/CFT correspondence and examine its implications.

A significant portion of the research is dedicated to investigating the thermal equilibrium of AdS black holes and perturbations of Schwarzschild AdS black holes in d dimensions. I analyze scalar, gravitational, and electromagnetic perturbations, computing their quasinormal frequencies to understand the dynamic behavior of AdS black holes.

Moreover, I delve into the thermodynamic quantities of AdS black holes and extend my analysis to rotating black holes, employing a novel numerical technique which avoids traditional root-finding routines for computing quasinormal frequencies. By applying the continued fraction method proposed by Leaver with my new technique (i.e. using Padé approximation and modified Lent's algorithm rather than using the conventional computation method directly), I achieved excellent accuracy in evaluating the angular eigenvalues of Teukolsky's angular equation, enabling the calculation of both slowly and rapidly damped quasinormal frequencies.

Furthermore, I explored the Kerr-Sen black hole, studying the correspondence between its shadow radius and quasinormal modes. Through rigorous analysis, I derive expressions for the real part of quasinormal modes related to the shadow radius, particularly focusing on the eikonal limit.

By employing advanced mathematical techniques and numerical methods, this research contributes to a deeper understanding of AdS black holes, their dynamic behavior, and their QNM properties. These findings enrich my understanding of fundamental principles in theoretical physics and pave the way for further exploration in this fascinating field especially in the field of gravitational waves.

Keywords— AdS, Quasi Normal Frequencies, Black Hole.

Table of Contents

Dedication **i**

Certificate **iii**

Declaration **v**

Acknowledgements **vii**

Abstract **ix**

Table of Contents **xi**

List of Figures **xv**

List of Tables **xvii**

List of Abbreviations **xix**

I **1**

Chapter 1 Introduction **3**

1.1 Hints For Holography 4

1.1.1 Prelude 5

1.1.2 Emergence of Gravity 6

1.2 Black Holes 9

1.2.1 Schwarzschild Radius 10

1.2.2 Classical Black Hole Geometry 11

1.2.3 Rindler Spacetime and Causal Structure 13

1.2.4 Penrose Diagram 16

1.2.5 Temperature of a black hole 18

1.2.6 Black Hole Thermodynamics 21

Chapter 2 Holographic Duality 25

2.1 Holographic Principle 25

2.2 Expansion at large N in gauge theories 27

2.2.1 Vaccum Energy 29

2.2.2 General Observables 32

2.3 Large N Expansion As a String Theory 36

2.3.1 String Theory 36

Chapter 3 AdS/CFT Conjecture 45

3.1 String Theory in the Perturbative (Bosonic) Regime . . 45

3.1.1 Overall Framework 45

3.2 Light-Cone Quantization 48

3.2.1 Light Cone Gauge 50

3.2.2 Quantization : 53

3.3 D-Branes 58

II 63

Chapter 4 Introduction 65

Chapter 5 The AdS spacetime 67

5.1 Spacetimes with constant curvature 67

5.2 Various coordinate systems of AdS spacetime 69

5.3 Maximally symmetric spacetimes 71

Chapter 6 The AdS black hole 73

6.1 Thermodynamic quantities of AdS black hole 74

6.2 AdS Black Holes and Thermality 76

Chapter 7 Properties of AdS Black Holes 77

7.1 How anti-de Sitter black holes reach thermal equilibrium 77

7.2 Perturbations of anti-de Sitter black holes 80

7.2.1 Perturbations 81

Scalar perturbations: 82

Gravitational perturbations 84

Electromagnetic perturbations: 93

Chapter 8 A detailed study of quasinormal frequencies of Kerr black hole 95

8.1 Introduction 95

8.1.1 Rotating Black Holes 97

8.1.2 Kerr metric 98

Important surfaces 99

Ring singularity 100

8.2 Angular and radial continued fractions equations 101

8.2.1 New technique for the angular equation 106

8.2.2 Radial equation and numerical results 110

Chapter 9 A detailed study of quasi-normal frequencies of Kerr Sen black hole 115

9.1 Kerr Sen Spacetime 115

9.2 Quasi-Normal Modes (QNMs) of the Kerr-Sen Black Hole 118

9.2.1 perturbation of the scalar field 118

9.3 The relationship between Quasinormal Modes (QNMs) and the shadow radius. 121

Chapter 10 Conclusion 125

Appendix A Appendix A 127

A.1 $S_P = S_{NG}$ at Classical Level 127

Appendix B Appendix B 129

B.1 Asymptotic Limit of Bessel Functions 129

B.2 Appendix B.2 130

Appendix C Appendix C 131

C.1 Shadow Radius of Kerr Sen Black Hole 132

Bibliography 133

List of Figures

1.1 AdS/CFT duality 6
1.2 Causal structure of $\mathcal{M}_2$ represented in the Rindler form. 14
1.3 Black hole geometry near horizon. 15
1.4 The geometry of a Schwarzschild black hole depicted in Kruskal coordinates. 16
1.5 $\mathcal{M}_2$ Penrose diagram. 18
1.6 Penrose diagram depicting the Schwarzschild black hole in $\mathcal{M}_2$. 18
1.7 Schwarzschild black hole near horizon geometry in Minkowski (left) and Euclidean (right) signature. 19
1.8 Rindler spacetime in Minkowski (left) and Euclidean (right) signature. 20

2.1 Vaccum Diagram 29
2.2 First Order vacuum diagram 29
2.3 Non-planar diagrams on a torus. 30
2.4 sphere (genus-0), torus (genus-1) and double torus(genus-2). 30

3.1 D-brane 58

5.1 The inclusion of AdS_2 within $\mathbb{R}^{2,1}$. Since the temporal axis $\tilde{t}$ displays periodic behavior, we investigate the covering space. 68
5.2 The AdS_2 spacetime represented in conformal coordinates. Poincaré coordinates only encompass a portion of the complete AdS spacetime, illustrated by the dark shaded region (Poincaré patch). 70

8.1 Location of the horizons, ergospheres, and the ring singularity of the Kerr spacetime in Cartesian Kerr–Schild coordinates. 100
8.2 Real part of λ for $\hat{a} = 0.1$ 109
8.3 Imaginary part of λ for $\hat{a} = 0.1$ 109
8.4 Real part of λ for $\hat{a} = 0.3$ 109

8.5 Imaginary part of λ for $\hat{a} = 0.3$ 109

8.6 Real part of λ for $\hat{a} = 0.5$ 109

8.7 Imaginary part of λ for $\hat{a} = 0.5$ 109

8.8 The initial quasinormal frequencies for $l = 2$ and $m = 0$, scaled by $2M$, are depicted in the complex plane. Each panel showcases a distinct angular momentum per unit mass $\hat{a}$, spanning from 0.0 to M, nearing the Kerr limit. 112

8.9 The depicted modes include the first, third, fifth, seventh, and ninth quasinormal modes associated with $l = 2$ and $m = 0$, all scaled by $2M$. These modes vary with the rotation parameter $\hat{a}$, ranging from $\hat{a} = 0$ at the upper left end (represented by squares) to $\hat{a} = 0.49$ at different positions. Intermediate dots correspond to $\hat{a} = 0.1, 0.2, 0.3, 0.4$. Notably, the ninth mode lies on the imaginary axis when $\hat{a} = 0.0$, exhibiting the expected behavior as it progresses. 113

8.10 We plot a detailed view of the curve depicting the fifth mode for $m = \pm 1$. Additionally, we demonstrate the complex conjugate relationship of the Kerr quasinormal frequencies, where squares denote the complex conjugate frequencies for $a = 0.0$. 113

List of Tables

8.1 This table displays the parameters obtained through fitting the Padé approximation for λ, based on numerical data generated by a computer program computing the angular eigenvalues of the Teukolsky equation, specifically for $m = 0$. 110

8.2 This table presents the parameters derived from fitting the Padé approximation for λ to the numerical output generated by a computer program computing the angular eigenvalues of the Teukolsky equation, specifically for $m = -1$. 110

8.3 This table displays the parameters obtained by fitting the Padé approximation for λ to the numerical results obtained from a computer program computing the angular eigenvalues of the Teukolsky equation, specifically for $m = +1$. 110

8.4 Numerical values of the first five Kerr quasinormal frequencies for $l = 2$, $m = 0$, ranging from $\hat{a} = 0.0$ to 0.49. 114

8.5 In this table, I present a comparison between our fundamental mode and Leaver's results for $l = 2$ and $m = 0$, illustrating their close similarity. 114

List of Abbreviations

AdS: Anti-de Sitter

BH: Black Hole

CFT: Conformal Field Theory

EM: Electromagnetic

GR: General Relativity

KS: Kerr Sen

QCD: Quantum Chromodynamics

QFT: Quantum Field Theory

QNF: Quasi Normal frequency

QNM: Quasinormal Mode

SAdS: Schwarzschild Anti-de Sitter

Part I

1

Introduction

In the realm of theoretical physics, there exist profound and captivating ideas that transcend the boundaries of our conventional understanding of the universe. These ideas not only challenge our fundamental notions of space, time, and matter but also reveal unexpected connections between disparate facets of the physical world. Among these remarkable concepts are the AdS/CFT correspondence, holographic duality, and large N symmetries. Each of these notions, in its own right, has revolutionized our comprehension of the cosmos. Yet, when viewed together, they present a panoramic view of the universe that defies our intuitions and beckons us to explore the hidden depths of theoretical physics.

The AdS/CFT correspondence, often referred to as the holographic principle, stands as a pinnacle of 21st-century theoretical physics. It asserts a remarkable relationship between two seemingly unrelated theories: Anti-de Sitter space (AdS), a negatively curved spacetime, and conformal field theory (CFT), a quantum field theory living on its boundary. In this duality, a gravitational theory in AdS is equivalent to a quantum field theory on the boundary of that spacetime. This profound insight, first conjectured by Juan Maldacena in 1997, not only bridges the chasm between quantum mechanics and gravity but also opens new vistas for understanding black holes, quantum entanglement, and the very nature of spacetime itself.

My Thesis embarks on a captivating journey into the interconnected worlds of the AdS/CFT correspondence, holographic duality, and gauge-gravity correspondence and a little bit about string theory. We will delve into the historical developments, mathematical foundations, and multifaceted applications of these ideas, striving to unravel the mysteries they hold and the profound implications they bear for our understanding of the cosmos.

1.1 Hints For Holography

"The career of a young theoretical physicist consists of treating the harmonic oscillator in ever-increasing levels of abstraction." - ***Sidney Coleman***

In this section, we examine the idea of holographic duality. We start by investigating gravitational systems and deriving the principles of black hole thermodynamics, which ultimately give rise to the holography principle. Then, we delve into gauge theory, particularly focusing on the large N (t'Hooft) limit. Finally, we draw comparisons between this theory and string theory, offering valuable perspectives on holographic duality.

Anti-de Sitter space spans across different spatial dimensions, notably serving a pivotal function in the AdS/CFT correspondence. This correspondence hints at the potential to depict a fundamental force in quantum mechanics, like electromagnetism or the strong force, within a defined number of dimensions through string theory. Here, the strings are situated within an anti-de Sitter space, encompassing an extra (non-compact) dimension.

1.1.1 Prelude

Theoretical interactions are well-described by the path integral formalism and Wilsonian Renormalization Group, yet translating calculations into this framework isn't always feasible. Gravity, however, presents distinct challenges due to its unique nature. From the theory of general gravity (GR):

Classical Gravity = Space-time (no concept of spacetime fabric, simply GR)

Understanding quantum gravity poses challenges, requiring a dynamic view of spacetime. The fundamental nature of spacetime — whether it's inherent or emergent, continuous or discrete — poses intriguing questions. The quantum behavior of black holes and the origins of the universe remain captivating subjects, with the potential profound importance of gravity's weakness adding to the mystery.

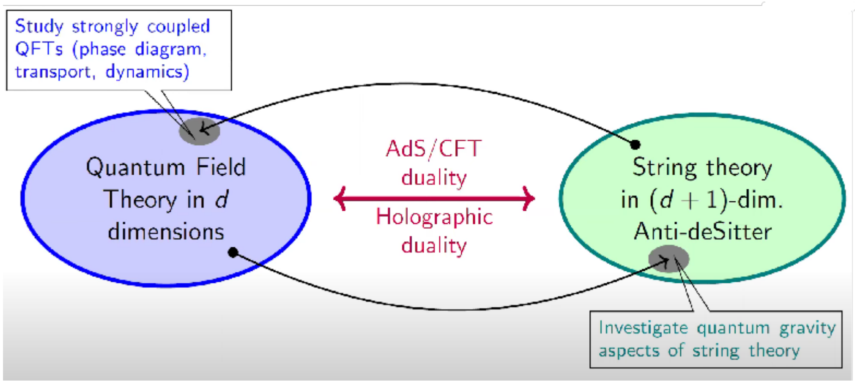
Study strongly coupled QFTs (phase diagram, transport, dynamics)
Quantum Field Theory in d dimensions
AdS/CFT duality
Holographic duality
String theory in $(d+1)$-dim. Anti-deSitter
Investigate quantum gravity aspects of string theory

Figure 1.1: AdS/CFT duality

1.1.2 Emergence of Gravity

Considering field theory, a common question arises: Can massless spin-2 particles (gravitons) emerge from a theory that encompasses massless spin-1 particles (such as photons and gluons) and spin-1/2 particles (such as protons and electrons)? The emergence of gravitons would suggest gravity's emergent nature. While Quantum Chromodynamics (QCD) exhibits massive spin-2 excitations, attempts to manipulate the theory to produce massless spin-2 particles were hampered by Weinberg and Witten's powerful theorem.

Theorem 1.1.1. *A theory that permits the establishment of a Lorentz-invariant conserved 4-vector current* J^{μ} *cannot accommodate massless particles with spins greater than 1/2, provided that the proposed charge* $\int J^0 d^3x$ *possesses a non-zero value.*

Theorem 1.1.2. *A theory that permits the existence of a preserved Lorentz-invariant stress tensor* $T^{\mu\nu}$ *cannot include massless particles with spin > 1.*

Proof. Let's imagine a scenario where we examine a theory allowing Lorentz-covariant conserved currents and stress tensors, which can incorporate massless particles possessing spin-J. In this context, each individual particle state can be denoted as $|k,\sigma\rangle$, where $k^\mu = (k^0, \mathbf{k})$, and $\sigma = \pm j$ signifies the particle's helicity. We then have:

$$\hat{R}(\theta, \hat{k})\,|k,\sigma\rangle = e^{i\sigma\theta}\,|k,\sigma\rangle \tag{1.1}$$

Here, $\hat{R}(\theta, \hat{k})$ denotes the rotation operator by an angle θ around $\hat{k} = \frac{\mathbf{k}}{|k|}$. The Lorentz-covariant current, denoted as J^μ, gives rise to a conserved charge represented as:

$$\hat{Q} = \int J^0 d^3x \tag{1.2}$$

Additionally, the Lorentz-covariant stress tensor, indicated by $T^{\mu\nu}$, encompasses the conserved momentum:

$$\hat{P} = \int T^{0\mu} d^3x \tag{1.3}$$

Consequently, we have:

$$\hat{P}^\mu\,|k,\sigma\rangle = k^\mu\,|k,\sigma\rangle \tag{1.4}$$

When the state $|k,\sigma\rangle$ is subject to the symmetry generated by J^μ with a charge of q:

$$\hat{Q}\,|k,\sigma\rangle = q\,|k,\sigma\rangle \tag{1.5}$$

Our aim is to establish:

1. If $q \neq 0$, then $j \leq \frac{1}{2}$

2. For Lorentz covariant conserved $T^{\mu\nu}$, $j \leq 1$

To begin, we state that Lorentz invariance implies:

$$\langle k,\sigma|\, J^{\mu}\, |k',\sigma\rangle \xrightarrow{k\to k'} \frac{qk^{\mu}}{k^{0}}\frac{1}{(2\pi)^{3}} \tag{1.6}$$

$$\langle k,\sigma|\, T^{\mu\nu}\, |k',\sigma\rangle \xrightarrow{k\to k'} \frac{k^{\mu}k^{\nu}}{k^{0}}\frac{1}{(2\pi)^{3}} \tag{1.7}$$

In the expression $\langle k,\sigma,|,k',\sigma'\rangle = \delta_{\sigma\sigma'}\delta^{(3)}(\mathbf{k}-\mathbf{k}')$, when examining the 0th component of equation (1.6), we find $\langle k,\sigma\,|J^{0}|\,k',\sigma\rangle \xrightarrow{k\to k'} \frac{q}{(2\pi)^{3}}$.

For massless particles, where $k^{2} = k'^{2} = 0$, it implies $k^{\mu}k'_{\mu} < 0$, suggesting $k+k'$ to be timelike. Choosing a frame such that $\mathbf{k}+\mathbf{k}' = 0$ and $k^{\mu} = (E,0,0,E)$ and $k'^{\mu} = (E,0,0,-E)$, rotation by θ around the z-axis yields the following outcome:

$$\hat{R}(\theta)\,|k,j\rangle = e^{ij\theta}\,|k,j\rangle\,,\quad \hat{R}(\theta)\,|k',j\rangle = e^{-ij\theta}\,|k',j\rangle \tag{1.8}$$

$$\langle k',j\left|\hat{R}^{-1}(\theta)J^{\mu}\hat{R}(\theta)\right|k,j\rangle = e^{2ij\theta}\langle k',j\,|J^{\mu}|\,k,j\rangle \tag{1.9}$$

$$\Rightarrow e^{2ij\theta}\langle k',j\,|J^{\mu}|\,k,j\rangle = \Lambda^{\mu}_{\nu}(\theta)\langle k',j\,|J^{\nu}|\,k,j\rangle \tag{1.10}$$

In equation (1.8), the negative sign arises because k' possesses the opposite orientation to k, hence the helicity should also change sign. Λ^{μ}_{ν} represents the transformation induced by a rotation of a 4-vector by an angle θ around the z-axis. Similarly,

$$e^{2ij\theta}\langle k',j\,|T^{\mu\nu}|\,k,j\rangle = \Lambda^{\mu}_{\rho}(\theta)\Lambda^{\nu}_{\lambda}(\theta)\langle k',j\,\left|T^{\rho\lambda}\right|\,k,j\rangle \tag{1.11}$$

$$e^{2ij\theta}\langle k',j\,|T^{\mu\nu}|\,k,j\rangle = \Lambda^{\mu}_{\rho}(\theta)\Lambda^{\nu}_{\lambda}(\theta)\langle k',j\,\left|T^{\rho\lambda}\right|\,k,j\rangle \tag{1.12}$$

Therefore, $\langle k',j\left|\hat{R}^{-1}(\theta)J^{\mu}\hat{R}(\theta)\right|k,j\rangle$ can only possess a non-zero value if $j \leq 1/2$. Otherwise, equation (1.6) would be contradicted because $\Lambda^{\mu}_{\nu}(\theta)$ has eigenvalues $e^{\pm i\theta}, 1$. Similarly, $\langle k',j\,|T^{\mu\nu}|\,k,j\rangle$ can only be non-zero if $j \leq 1$. Otherwise, equation

(1.7) would be contradicted. Therefore, both theorems are proven. □

The Weinberg-Witten Theorem prohibits massless spin-2 particles, crucial for gravity, in QFT's spacetime. However, emergent gravity may arise in different spacetime realms, as demonstrated in holographic duality.

Remarks:

1. The principles of black hole thermodynamics lead to the holographic principle.
2. Gauge theories with a large N lead to gauge/string duality.

1.2 Black Holes

First, we'll compare the strength of gravity with that of the electromagnetic (EM) interaction. In the case of EM, the interaction is described by $V_{EM} = e^2/r$. Here, we consider the reduced Compton wavelength $r_c = \frac{\hbar}{mc}$ as the minimum separation between particles, reflecting a fundamental limit on measuring particle positions due to the principles of quantum mechanics and special relativity. Using the unit of particle static mass, the EM interaction has the effective strength:

$$\lambda_{EM} = \frac{V_{EM}(r_C)}{mc^2} = \frac{e^2}{\hbar c} = \alpha = \frac{1}{137} \tag{1.13}$$

Alternatively, we can determine the effective magnitude of gravity:

$$\lambda_G = \frac{V_G(r_c)}{mc^2} = \frac{G_N m^2}{\hbar/mc}\frac{1}{mc^2} = \frac{m^2}{m_p^2} = \frac{l_p^2}{r_c^2} \tag{1.14}$$

In such cases, $\lambda_G \ll 1$ for $m \ll m_p$, where m_p denotes the Planck mass and l_p represents the Planck length. As an illustration, for an electron with a mass of 5×10^{-4} GeV/c^2, we find:

$$\frac{\lambda_G}{\lambda_{EM}} \approx 10^{-43} \tag{1.15}$$

In this scenario, the gravitational influence is relatively feeble. However, if the mass reaches the Planck scale m_p, then $\lambda_G \sim \mathcal{O}(1)$, indicating that quantum gravity effects become notable (with the corresponding length scale being l_p).

1.2.1 Schwarzschild Radius

To determine at what distance r_s from an object of mass m classical gravity becomes significant, we can examine the influence of a probe mass m'. At the point where classical gravity becomes strong, means that

$$\frac{G_N m m'/r_s}{m'c^2} \sim 1 \quad \Rightarrow r_s = \frac{G_N m}{c^2} \tag{1.16}$$

For an object with mass m, we have two significant scales to consider:

1. $r_c = \frac{\hbar}{mc}$ — Known as the Reduced Compton wavelength.
2. $r_s = \frac{2G_N m}{c^2}$ — Known as the Schwarzschild radius.

The factor of 2 in r_s originates from a General Relativity calculation concerning a Schwarzschild black hole. From the comparison $\frac{r_s}{r_c} \sim \frac{m^2}{m_p^2}$, we can infer:

1. When $m \gg m_p$, $r_s \gg r_c$: Classical gravity dominates (quantum effects are negligible).

2. When $m \ll m_p$, $r_s \ll r_c$: r_s is insignificant, and gravity has a weak impact.

3. When $m \sim m_p$, $r_s \sim r_c$: Quantum gravity effects become significant.

However, the story doesn't end there. Black holes can showcase quantum gravity effects on a macroscopic scale, at lengths approximately equal to $\mathcal{O}(r_s)$.

Remark 1.2.1. l_p serves as the fundamental limit of localization strength. In realms outside of gravity, the probing length scale $l \sim \frac{\hbar}{p}$ can theoretically approach infinitesimal sizes with sufficiently large momentum p. However, in gravitational contexts, when $E \sim p \gg m_p$, $r_s \sim \frac{G_N p}{c^3}$ emerges as the dominant scale. Given $r_s \propto p$, higher energies yield larger length scales, thus defining l_p as the minimal probable scale. Alternatively, considering the uncertainty principle $\delta p \sim \frac{\hbar}{\delta x}$, we derive $\delta x > \frac{G_N \delta p}{c^3} \sim \frac{G_N \hbar}{c^3 \delta x}$, resulting in $\delta x > \sqrt{\frac{\hbar G_N}{c^3}} = l_p$.

1.2.2 Classical Black Hole Geometry

The solution to Einstein's equation with zero cosmological constant yields black hole geometry, originating from an object of mass M. Assuming the object's spherical symmetry, non-rotation, and neutrality, we obtain the Schwarzschild metric solution:

$$ds^2 = -f dt^2 + \frac{1}{f} dr^2 + r^2(d\theta^2 + sin^2\theta d\phi^2), \;\; f = 1 - \frac{2G_N M}{r} = 1 - \frac{r_s}{r} \tag{1.17}$$

The event horizon is defined at $r = r_s = 2G_N M$, where $g_{tt} = 0$ and $g_{rr} = \infty$. As r passes the event horizon, there is a change in sign for f, and the roles of r and t switch.

Remark 1.2.2. 1. While it possesses time-reversal symmetry ($t \to -t$), it does not represent a black hole originating from gravitational collapse, which lacks such symmetry. Rather, it functions as a mathematical abstraction of such an occurrence.

2. One can confirm the absence of spacetime singularity at the horizon by computing curvature invariants (e.g., the Kretschmann scalar $I = R_{\alpha\beta\gamma\delta}R^{\alpha\beta\gamma\delta} = 48\frac{G_N^2 M^2}{r^6}$). The apparent singularity is merely a coordinate singularity, where Schwarzschild time (t) and radial coordinates (r) become singular at the horizon, rather than representing an inherent singularity.

3. The horizon experiences infinite redshift, observed by an observer O_h near $r = r_h \approx r_s$ and another O_∞ at $r = \infty$. At $r = \infty$, the spacetime metric yields $ds^2 \to -dt^2 + dr^2 + r^2 d\Omega^2$, where t denotes proper time for O_∞. Conversely, at $r = r_h$, the metric becomes $ds^2 = -f(r_h)dt^2 + \cdots = -d\tau^2 + \cdots$, with $d\tau^h = f^{1/2}(r_h)dt$ representing proper time for O_h. Then

$$\frac{d\tau_h}{dt} = (1 - \frac{r_s}{r_h})^{\frac{1}{2}} \tag{1.18}$$

As r_h approaches r_s, $\frac{d\tau_h}{dt}$ tends towards zero, implying that time near $r = r_h$ slows infinitely compared to $r = \infty$. Consider an event with energy E_h occurring at $r = r_h$: For observer O_∞, this event appears with energy $E_\infty = E_h f^{\frac{1}{2}}(r_h)$. Hence, for a fixed local energy E_h, E_∞ diminishes to zero as r_h approaches r_s, leading to what we term as infinite redshift.

4. A free-falling traveler requires a finite proper time to reach the horizon, yet an infinite Schwarzschild time.

5. The horizon possesses two intrinsic geometric characteristics:

- Spatial section area: $A = 4\pi r_s^2 = 16\pi G_N^2 M^2$
- Surface gravity: Characterized as the acceleration experienced by a stationary observer positioned at the horizon, as measured by an observer situated at infinity. It is expressed by $K = \frac{1}{2}f'(r_s) = \frac{1}{4G_N M}$.

1.2.3 Rindler Spacetime and Causal Structure

To understand the spacetime arrangement around a black hole, let's focus on the region just outside its horizon. Here, we define the proper distance ρ from the horizon as follows:

$$d\rho = \frac{dr}{\sqrt{f}} \xrightarrow{r \to r_s} \frac{dr}{\sqrt{f'(r_s)(r - r_s) + \cdots}} \tag{1.19}$$

$$\Rightarrow \rho = \frac{2}{\sqrt{f'(r_s)}}\sqrt{r - r_s} \tag{1.20}$$

Expressing it as a function of ρ, we have:

$$f(r) = f'(r_s)(r - r_s) + \cdots = \left(\frac{1}{2}f'(r_s)\right)^2 \rho^2 + \cdots = K^2\rho^2 + \cdots \tag{1.21}$$

where K represents the surface gravity. Near the horizon, the metric becomes:

$$ds^2 = -K^2\rho^2 dt^2 + d\rho^2 + r_s^2 d\Omega_2^2 = -\rho^2 d\eta^2 + d\rho^2 + r_s^2 d\Omega_2^2 \tag{1.22}$$

In this context, we introduce the variable $\eta = Kt = \frac{t}{2r_s}$. The initial two components of the mentioned expression are referred to as the (1+1)-dimensional Minkowski metric represented in a Rindler format.

Consider $\mathcal{M}_2$ (2d Minkowski spacetime):

$$ds^2_{\mathcal{M}_2} = -dT^2 + dX^2 \tag{1.23}$$

Let's consider, $X = \rho\cosh\eta$, $T = \rho\sinh\eta$, we have

$$ds^2_{\mathcal{M}_2} = -\rho^2 d\eta^2 + d\rho^2 \tag{1.24}$$

As $X^2 - T^2 = \rho^2 \geq 0$, the (ρ, η) coordinates cover only part of $\mathcal{M}_2$. The sector where $\rho \geq 0$ corresponds to $X \geq 0$ or region I in figure1.2

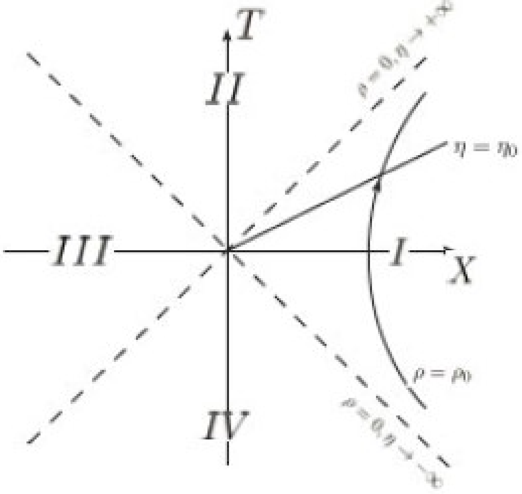

Figure 1.2: Causal structure of $\mathcal{M}_2$ represented in the Rindler form.

Note the following:

1. For $X = T (X > 0)$: As $\eta \to \infty$, $\rho \to 0$ with ρe^{η} remaining finite.
2. For $X = -T (X > 0)$: As $\eta \to -\infty$, $\rho \to 0$ with $\rho e^{-\eta}$ remaining finite.
3. For $X = T = 0$: $\rho = 0$ for any finite η.

Consequently, the black hole's horizon $\rho = 0$ corresponds to a light cone where $X = \pm T$. The geometry near the black hole's horizon can be conceptualized as Rindler space multiplied by a 2-sphere, as depicted in Fig. 1.3

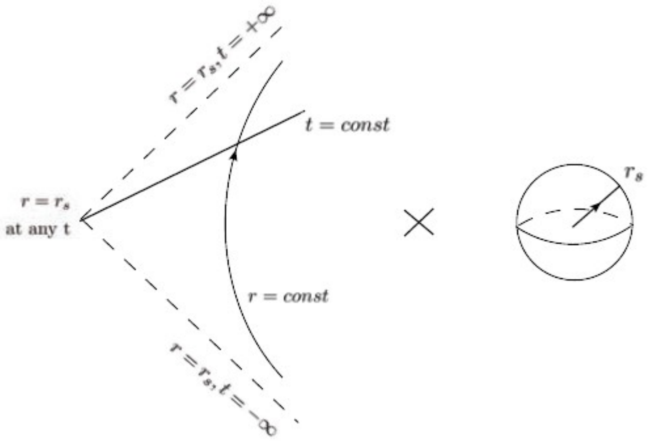

Figure 1.3: Black hole geometry near horizon.

Remark 1.2.3. 1. An observer situated at $r =$ const. for $(r \geq r_s)$ is equivalent to an observer with $\rho =$ const. within a Rindler patch, representing an observer in Minkowski spacetime tracing a hyperbolic trajectory $X^2 - T^2 = \rho^2 =$ const. Such an observer experiences a proper acceleration given by

$$a = \frac{1}{\rho} = \frac{f'(r_s)}{2} \frac{1}{\sqrt{r - r_s}} \tag{1.25}$$

Moreover, the acceleration observed by O_∞ is given by $a_\infty = a(r) f^{1/2}(r) = K$.

2. A free-falling observer in close proximity to a black hole's horizon is equivalent to an inertial observer within $\mathcal{M}_2$.

3. In Rindler coordinates (ρ, η), there is a singularity at $\rho = 0$. However, the use of Minkowski coordinates (X, T) allows for the extension of region I to cover the entire Minkowski spacetime. Similarly, transitioning to appropriate coordinates

(Kruskal coordinates) enables the expansion of Schwarzschild spacetime into four quadrants (refer to Fig. 1.4).

- It's evident that neither information nor any observer within Region II can traverse to Region I, as they are distinguished from a future horizon.
- Regions III and IV are time-reversed counterparts of I and II respectively, but they are not present in real black holes formed from gravitational collapse. Observers in region I cannot affect events in region IV, as they are separated by a past horizon.
- At $r = 0$, a space-like curvature singularity is present, known as the singularity of a black hole.

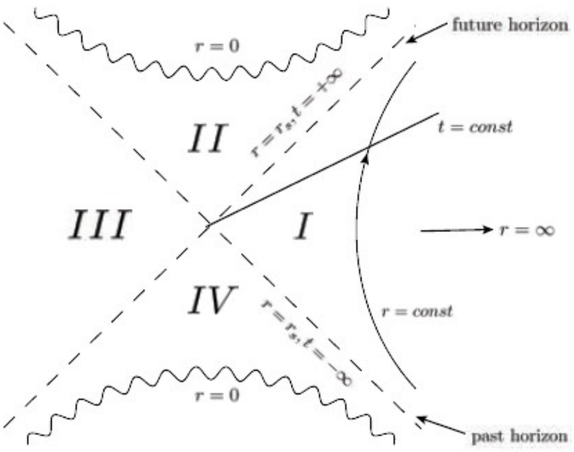

Figure 1.4: The geometry of a Schwarzschild black hole depicted in Kruskal coordinates.

1.2.4 Penrose Diagram

In this section, we explore Penrose diagrams, employed for depicting the overall causal arrangement of a spacetime. Our examination begins with the metric formulation: $ds^2 = g_{ab}(x)dx^a dx^b$.

1. Discover a coordinate transformation $x^a = x^a(y^\alpha)$ such that y^α possesses a finite range, effectively mapping the entire spacetime onto a finite region.
2. Create an alternate metric that is conformally linked to the initial metric:

$$d\tilde{s}^2 = \Omega^2(y)ds^2 = \tilde{g}_{\alpha\beta}(y)dy^\alpha dy^\beta \tag{1.26}$$

   ensuring that $\tilde{g}_{\alpha\beta}$ is straightforward. This transformation preserves the causal structure as null rays remain unaffected by conformal rescalings.

Example : (1+1)d Minkowski space

$$ds^2 = -dT^2 + dX^2 = -dUdV; \quad U = T - X, V = T + X$$

Let $U = \tan u$ and $V = \tan v$, where u and v are within the interval $[-\frac{\pi}{2}, \frac{\pi}{2}]$. We define the following in the context of Example : (1+1)d Minkowski space:

- i_0: Spatial infinity (infinite X, finite T)
- i_+: Timelike future infinity ($T \to \infty$, finite X)
- i_-: Timelike past infinity ($T \to -\infty$, finite X)
- I_+: Null future infinity (termination point for all null rays)
- I_-: Null past infinity (origin point for all null rays)

These points (lines) are to be indicated accordingly on the Penrose diagram for $\mathcal{M}_2$, as depicted in Fig. 1.5.

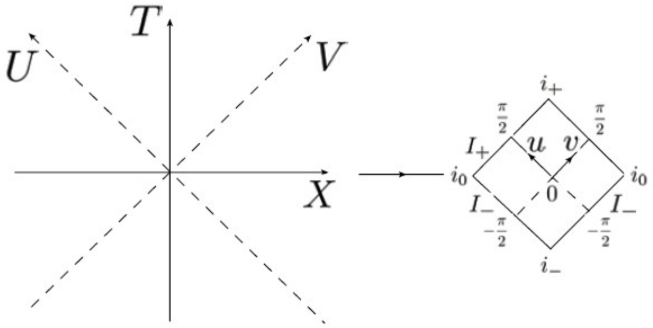

Figure 1.5: $\mathcal{M}_2$ Penrose diagram.

Another intriguing instance involves the Schwarzschild black hole:

- Initially, we examine the (r, t) plane.
- Subsequently, we transition to a coordinate system (Kruskal) encompassing all 4 regions (similar to U, V in Minkowski spacetime).
- Finally, we perform a coordinate transformation to render the new coordinates finite in range, converting (U, V) to (u, v).

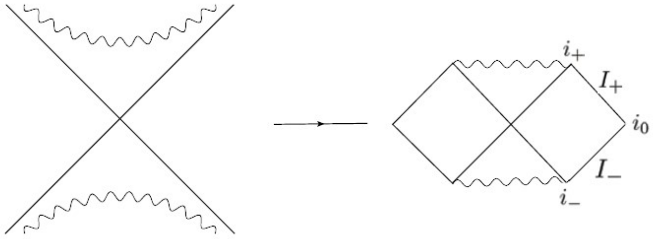

Figure 1.6: Penrose diagram depicting the Schwarzschild black hole in $\mathcal{M}_2$.

1.2.5 Temperature of a black hole

In QFT, when considering a finite temperature (T), we transition to Euclidean signature by substituting t with $-\tau$, where τ is periodic: $\tau \sim \tau + \hbar\beta$, with $\beta = \frac{1}{T}$.

When the Schwarzschild metric is analytically continued to Euclidean signature with $t \to -i\tau$, it yields the following expression near the horizon:

$$dS_E^2 = \rho^2 K^2 d\tau^2 + d\rho^2 + r^2 d\Omega_2^2 = d\rho^2 + r_s^2 d\Omega_2^2; \quad \theta = K\tau = \frac{\tau}{2r_s} \tag{1.27}$$

Take into account that the first two terms represent polar coordinates in Euclidean $\mathcal{R}^2$. This metric displays a conical singularity unless θ has periodicity over 2π, meaning $\theta \sim \theta + 2\pi$. Since the horizon remains nonsingular in Lorentzian signature, it should also lack singularity in Euclidean form. Hence, τ must be periodic.

$$\tau \sim \tau + \frac{2\pi}{K} \tag{1.28}$$

Note that t represents the proper time for an observer situated at $r = \infty$, implying that this observer would perceive a temperature:

$$T = \frac{1}{\beta} = \frac{\hbar K}{2\pi} = \frac{\hbar}{8\pi G_N m} \tag{1.29}$$

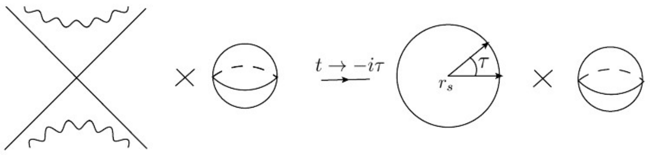

Figure 1.7: Schwarzschild black hole near horizon geometry in Minkowski (left) and Euclidean (right) signature.

For an observer at a certain radial distance r, as $dt_{\text{loc}} = f^{\frac{1}{2}}(r)dt$, the local temperature becomes infinite near the horizon, indicating that the black hole horizon appears extremely hot for a stationary observer !!!!

Similarly for Rindler spacetime

$$ds^2 = -\rho^2 d\eta^2 + d\rho^2 \rightarrow \eta = -i\theta ds_E^2 = \rho^2 d\theta^2 + d\rho^2 \tag{1.30}$$

Given the periodicity of θ over 2π, we establish the local proper time as $d\tau_{loc}^2 = \rho^2 d\theta^2$, thus necessitating periodicity for τ_{loc}.

$$T_{loc}^{Rindler}(\rho) = \frac{\hbar}{2\pi\rho} = \frac{\hbar a}{2\pi} \tag{1.31}$$

In Minkowski spacetime, considering $a = \frac{1}{\rho}$, an accelerating observer will sense a temperature that is proportional to its acceleration.

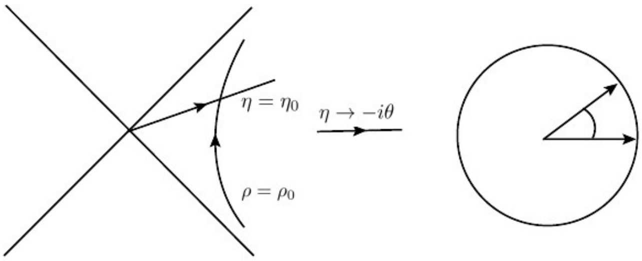

Figure 1.8: Rindler spacetime in Minkowski (left) and Euclidean (right) signature.

Physical interpretation of the temperature

In a black hole spacetime, a QFT's "vacuum" state, derived through analytic continuation from the Euclidean signature, represents a thermal equilibrium state with the associated temperature.

Remark 1.2.4. 1. In a curved spacetime, there isn't a single vacuum choice for a QFT. For a Schwarzschild black hole, it's a "Hartle-Hawking vacuum" whereas, in a Rindler scenario, it's the Minkowski vacuum confined to the Rindler patch (reduced density matrix of the Minkowski vacuum).

2. When considering a black hole, if τ is chosen to be noncompact in Euclidean signature, we arrive at the Schwarzschild vacuum (Boulware vacuum), obtained through canonical quantization in terms of Schwarzschild time t. In the Rindler scenario, if θ is noncompact, we obtain the Rindler vacuum, achieved through canonical quantization in the Rindler patch using η.

3. In the Schwarzschild vacuum, physical observables often become singular at the horizon due to the singularity in the corresponding Euclidean manifold, such as the stress tensor blowing up, unlike in Lorentzian signature.

1.2.6 Black Hole Thermodynamics

As discussed earlier, it's established that a black hole possesses a temperature:

$$T_{BH} = \frac{\hbar}{8\pi G_N m}$$

Therefore, a black hole operates as a thermodynamic entity, adhering to the principles of thermodynamics. Now, consider the thermodynamic relationships:

$$\frac{dS}{dE} = \frac{1}{T(E)} = \frac{8\pi G_N m}{\hbar} \tag{1.32}$$

Since for a black hole E = m, Entropy

$$S(E) = \int \frac{dE}{T(E)} = \frac{4\pi G_N E^2}{\hbar} + const = \frac{4\pi r_s^2}{4\hbar G_N} = \frac{A_{BH}}{e\hbar G_N} \tag{1.33}$$

The integral constant can be established as zero given that $S(E) = 0$ when $E = 0$, where A_{BH} represents the area of the black hole horizon. Hence, it can be concluded for black holes that

$$T_{BH} = \frac{\hbar K}{2\pi}, \quad S_{BH} = \frac{A_{BH}}{4\hbar G_N} \tag{1.34}$$

It's important to observe that as the mass m increases, the black hole temperature T_{BH} decreases, indicating a negative specific heat for the system.

$$C = T\frac{\partial S}{\partial T} = \frac{\partial E}{\partial T} < 0 \tag{1.35}$$

General Black Holes

Theorem 1.2.5. ***No hair theorem****: A stationary black hole, exhibiting asymptotically flat behavior, is defined by its mass M, angular momentum J, and conserved gauged charges (such as electric charges Q).*

Now let's summarize 4 laws of black hole thermodynamics:

- 0th law: K = surface gravity, remains constant across the horizon.
- 1st law:

$$dM = \frac{K}{8\pi G_N} dA + \Omega dJ + \phi dQ \tag{1.36}$$

$$\Rightarrow dE = TdS + \Omega dJ + \phi dQ \tag{1.37}$$

  Here, Ω denotes the angular frequency at the horizon, while ϕ represents electric potential at the horizon (assumption: potential is 0 at infinity).

- 2nd law: In a classical context, the size of the horizon doesn't diminish.
- 3rd law: It's impossible to reduce the surface gravity of a black hole to zero

through a finite number of steps.

Before Hawking's breakthrough regarding black hole radiation, Bekenstein (1972-1974) established the relationship $S_{BH} \sim A_H$, aiming to uphold the $2nd$ law of thermodynamics within systems containing black holes. With a conventional system entering a black hole, its entropy becomes undetectable to an external observer, thus leading to the formulation of the generalized second law (GSL):

$$dS_{tot} \geq 0; \quad S_{tot} = S_{BH} + S_{matter}$$

As a result, several puzzles or paradoxes arise:

1. Can the entropy of a black hole be interpreted statistically?
2. Does a black hole adhere to the principles of quantum mechanics?

The first question has been affirmed for diverse kinds of black holes within the framework of string theory and holographic duality, indicating the presence of organized internal states:

$$N \sim e^{\frac{A_{BH}}{4\hbar G_N}} \tag{1.38}$$

The second inquiry pertains to Hawking's information loss paradox, which can be outlined as follows: Imagine a star is in its pure state collapsing to form a black hole, subsequently emitting thermal radiation. When $m \gg m_p$, the radiation is approximately thermal, resulting in minimal information about the initial state being emitted. However, once a black hole's mass becomes at the order of the Planck mass ($m \sim \mathcal{O}(m_p)$), it becomes too late for all the information to escape.

Consequently, we move from a pure state to a thermal one described by a density matrix, indicating the loss of information!

2

Holographic Duality

2.1 Holographic Principle

If we consider the black hole as a typical quantum mechanical entity, which leads to a significant consequence known as the holographic principle.

Imagine an isolated system characterized by its mass E and entropy S_0 in an asymptotically flat spacetime. Let A denote the area of the smallest sphere that encloses the system, and M_A represent the mass of a black hole with a comparable horizon area. It's crucial that $E < M_A$, as otherwise the system would already constitute a black hole.

Upon adding $M_A - E$ energy to the system while maintaining A constant, we will inevitably yield a black hole with a mass of M_A, since

$$S_{BH} \geq S_0 + S' \tag{2.1}$$

Here S' denotes the entropy of the added energy. Consequently, we deduce

$$S_0 \leq S_{BH} = \frac{A}{4\hbar G_N} \tag{2.2}$$

Put differently, the maximum entropy within a region confined by area A is given by:

$$S_{\max} = \frac{A}{4\hbar G_N} \tag{2.3}$$

Consider the entropy definition: $S = -\mathrm{Tr}\rho \log \rho$, where ρ denotes the density matrix of the system's state. For a system with an N-dimensional Hilbert space:

$$S_{\max} = \log N \tag{2.4}$$

Thus, the effective dimension of the Hilbert space for a system confined within a region of area A is constrained by

$$logN \leq \frac{A}{4\hbar G_N} = \frac{A}{4l_p^2} \tag{2.5}$$

****Holographic Principle****: In the realm of quantum gravity, a region bounded by an area A can be fully characterized by a maximum of $\frac{A}{4\hbar G_N} = \frac{A}{4l_p^2}$ degrees of freedom.

2.2 Expansion at large N in gauge theories

Now, let's examine indications of holographic duality from the field theory perspective. Take, for instance, QCD, which can be depicted as an SU(3) gauge theory featuring fundamental quarks. The Lagrangian can be expressed as

$$\mathcal{L} = \frac{1}{g_{YM}^2}\left[-\frac{1}{4}TrF_{\mu\nu}F^{\mu\nu} - i\overline{\Psi}(\not{D} - m)\Psi\right] \tag{2.6}$$

Here, $D_\mu = \partial_\mu - iA_\mu$, where A_μ represents 3×3 Hermitian matrices and can be expressed as $A_\mu = A_\mu^a T^a$, with $T^a \in SU(3)$. In such a scenario, coupling becomes strong in the infrared (IR) regime ($\Lambda_{QCD} \sim 250$ MeV), where there is no small parameter for expansion. Deriving the IR properties of QCD from first principles remains an open challenge.

In 1974, t' Hooft proposed treating the number of colors $N = 3$ as a parameter, thereby promoting A_μ to $N \times N$ Hermitian matrices and considering the limit $N \to \infty$ with a $\frac{1}{N}$ expansion. This was a clever idea. However, despite efforts, QCD remains unsolved at the leading order in the large N limit. N.b: QCD is still difficult to study in this way because $N = 3$ is not a large number and the quarks in QCD are in fundamental representation. Surprisingly, a correspondence between the large N gauge theory and string theory emerged, with the key insight being the matrix nature of fields. To illustrate, let's consider a scalar theory:

$$\mathcal{L} = -\frac{1}{g^2}Tr\left[\frac{1}{2}\partial_\mu\Phi\partial^\mu\Phi + \frac{1}{4}\Phi^4\right] \tag{2.7}$$

Here, g represents the coupling constant, and $\Phi(x) \equiv \Phi_b^a(x)$ denotes an $N \times N$

Hermitian matrix. In component form, this can be expressed as

$$\mathcal{L} = -\frac{1}{g^2}\left[\frac{1}{2}(\partial_\mu \Phi^a_b)(\partial^\mu \Phi^b_a) + \frac{1}{4}\Phi^a_b\Phi^b_c\Phi^c_d\Phi^d_a\right] \tag{2.8}$$

$\mathcal{L}$ is invariant under $\mathcal{U}(N)$ global symmetry.

Remark 2.2.1.

1. This theory involves N^2 scalar fields.
2. Alternative matrix types, such as $N \times N$ real symmetric matrices, can also be explored, leading to an SO(N) symmetry.
3. Introducing gauge fields enables the localization of the U(N) symmetry.

Below are the Feynman rules for this theory, starting with the propagator:

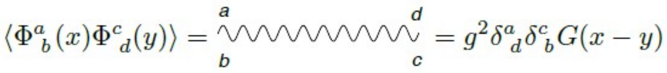

$$\langle \Phi^a{}_b(x)\Phi^c{}_d(y)\rangle = g^2\delta^a{}_d\delta^c{}_b G(x-y)$$

The fermion vertex:

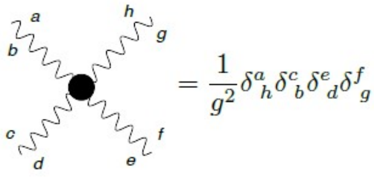

$$= \frac{1}{g^2}\delta^a{}_h\delta^c{}_b\delta^e{}_d\delta^f{}_g$$

Therefore, we can utilize the double-line notation here:

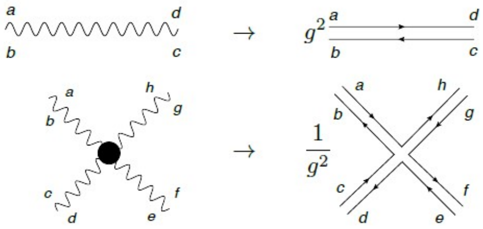

2.2.1 Vaccum Energy

Let's examine vacuum bubbles, which are diagrams without any external legs. The most basic diagrams in the lowest order will be:

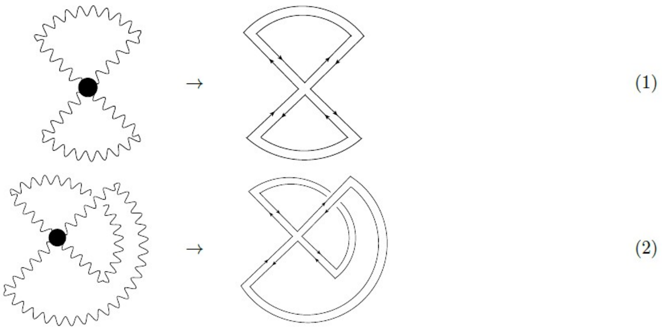

Figure 2.1: Vaccum Diagram

For diagram 1 of Fig. 2.1, each contracted index line contributes N, resulting in a total contribution on the order of $N^3\frac{(g^2)^2}{g^2} = N^3g^2$. For diagram 2 of Fig. 2.1, with only one contracted line, the total contribution is on the order of Ng^2. This disparity arises due to the non-commutativity of the matrices. In the first scenario, the diagram can be depicted on a plane without line crossings, termed as a planar diagram. Conversely, in the second scenario, the diagram cannot be represented on a plane without line crossings, designated as a non-planar diagram.

If we examine the subsequent order in perturbation theory

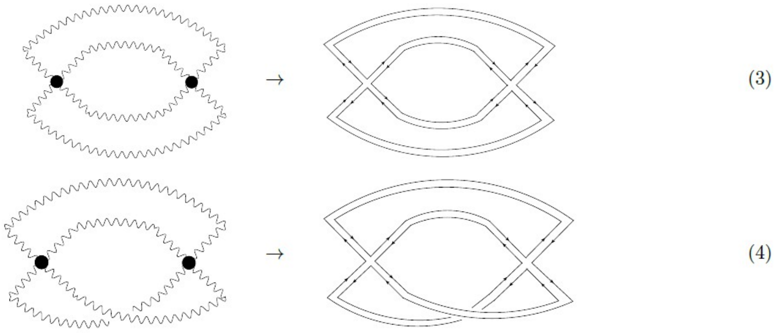

Figure 2.2: First Order vacuum diagram

The first diagram of Fig. 2.2 yields an order of $N^4 g^4$, while the second diagram results in an order of $N^2 g^4$. We may delve into higher-order diagrams, but how do we establish a general N-counting? Furthermore, how do we categorize all non-planar diagrams?

To address these inquiries, we make two observations.

- Diagrams 2 and 4 can be depicted on a torus without line crossings.

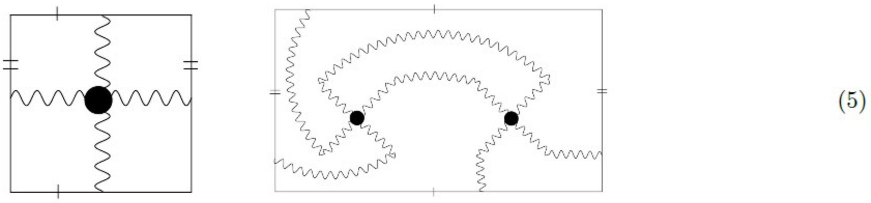

Figure 2.3: Non-planar diagrams on a torus.

- The N-power for each diagram corresponds to the number of faces in the diagram after straightening it out.

Indeed, any orientable two-dimensional surface is topologically categorized by an integer h, denoted as the genus. This genus signifies the number of "holes" present on the surface.

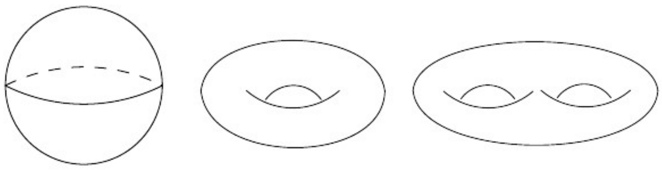

Figure 2.4: sphere (genus-0), torus (genus-1) and double torus(genus-2).

A topological property invariant to the manifold is the Euler characteristic:

$$\chi = 2 - 2h \tag{2.9}$$

where h is an integer representing the genus.

1. Any non-planar diagram can be unfolded (i.e., made non-crossing) on a surface with genus h, an integer characteristic of the surface, but not on a surface with a lesser genus.
2. In the case of any non-planar diagram, the degree of N arising from the contraction of propagators corresponds to the count of faces present on a surface characterized by genus h, representing the number of disjointed areas separated by the diagram.

Typically, a vacuum diagram displays a dependence on g^2 and N as follows:

$$A \sim (g^2)^E (g^2)^{-V} N^F \tag{2.10}$$

Here, E represents the count of propagators, V denotes the number of vertices, and F signifies the number of faces. This setup lacks a meaningful limit as $N \to \infty$ or a $\frac{1}{N}$ expansion due to the absence of an upper bound on F. However, t' Hooft suggests that we can approach the limit $N \to \infty$, $g^2 \to 0$ while maintaining $\lambda = g^2 N$ constant. Then, if L represents the number of loops,

$$A \sim (g^2 N)^{E-V} N^{F+V-E} = \lambda^{L-1} N^{\chi} \tag{2.11}$$

Theorem 2.2.2. *For a surface constituted of polygons with F faces, E edges, and V vertices, the Euler characteristic is defined as*

$$\chi = F + V - E = 2 - 2h \tag{2.12}$$

As every Feynman diagram can be viewed as a division of the surface, thereby segmenting it into polygons, the above theorem is applicable to our N-counting.

Therefore, in this limit, the leading order in N comprises the planar diagrams.

$$N^2(c_0 + c_1\lambda + c_2\lambda^2 + \cdots) = N^2 f_0(\lambda) \tag{2.13}$$

As $\log Z$ encompasses the summation of all vacuum diagrams, including higher-order $\frac{1}{N^2}$ corrections, we can infer that:

$$logZ = \sum_{h=0}^{\infty} N^{2-2h} f_h(\lambda) = N^2 f_0(\lambda) + f_1(\lambda) + \frac{1}{N^2} f_2(\lambda) + \cdots \tag{2.14}$$

The first term arises from the planar diagrams, while the subsequent terms originate from the genus-1 diagrams and beyond.

There exists a heuristic approach to grasp $\log Z = \mathcal{O}(N^2) + \cdots$. Given $Z = \int \mathcal{D}\Phi e^{iS[\Phi]}$, we can reconfigure the Lagrangian as:

$$\mathcal{L} = \frac{N}{\lambda} Tr \left[\frac{1}{2}(\partial\Phi)^2 + \frac{1}{4}\Phi^4 \right] \tag{2.15}$$

The trace operation likewise yields a factor of N, consequently $\mathcal{L} \sim \mathcal{O}(N^2)$, leading to $\log Z \sim \mathcal{O}(N^2)$.

2.2.2 General Observables

Examining permitted operators in both theories reveals that in eq. (2.7), operators such as Φ^a_b are permissible, despite lacking invariance under the global $U(N)$

symmetry. However, in eq. (2.6), where operators must maintain gauge invariance, Φ^a_b is disallowed. Consequently, in gauge theories like $\mathcal{L} = \mathcal{L}(A_\mu, \Phi, \cdots)$, the acceptable operators will be:

1. Single-trace operators include expressions such as $\text{Tr}(F_{\mu\nu}F^{\mu\nu})$ and $\text{Tr}(\Phi^n)$.
2. Multiple-trace operators encompass combinations like $\text{Tr}(F_{\mu\nu}F^{\mu\nu})\text{Tr}(\Phi^2)$, $\text{Tr}(\Phi^2)\text{Tr}(\Phi^n)\text{Tr}(\Phi^n), \cdots$.

We represent single-trace operators as $\mathcal{O}_k$, where $k = 1, \ldots$ denotes different operators. Multiple-trace operators take forms such as $\mathcal{O}_m\mathcal{O}_n(x)$, $\mathcal{O}_{m_1}\mathcal{O}_{m_2}\mathcal{O}_{m_3}(x)$, and so forth. Consequently, general observables consist of correlation functions of gauge-invariant operators, with our focus primarily on local operators:

$$\langle \mathcal{O}_1(x_1)\mathcal{O}_2(x_2)\cdots\mathcal{O}_n(x_n)\rangle_c \tag{2.16}$$

Given our focus on the t'Hooft limit, we aim to understand the scaling behavior of correlations (as per Eq. (2.16)) in the large N limit. To explore this, we employ a strategy:

$$Z\left[J_1, \cdots, J_n\right] = \int \mathcal{D}A_\mu \mathcal{D}\Phi \cdots e^{iS_{eff}} = \int \mathcal{D}A_\mu \mathcal{D}\Phi \cdots e^{\left[iS_0 + iN\sum_i \int J_i(x)\mathcal{O}_i(x)\right]} \tag{2.17}$$

Then the correlation (Eq. (2.16)) can be expressed as

$$\langle \mathcal{O}_1(x_1)\mathcal{O}_2(x_2)\cdots\mathcal{O}_n(x_n)\rangle_c = \frac{\delta^n logZ}{\delta J_1(x_1)\cdots\delta J_n(x_n)}\Big|_{J_1=\cdots=J_n=0}\frac{1}{(iN)^n} \tag{2.18}$$

Applying eq. (2.16) on eq. (2.14) we get,

$$\langle \mathbb{I} \rangle \sim \mathcal{O}(N^2) + \mathcal{O}(N^0) + \cdots \tag{2.19}$$

$$\langle \mathcal{O} \rangle \sim \mathcal{O}(N) + \mathcal{O}(N^{-1}) + \cdots \tag{2.20}$$

$$\langle \mathcal{O}_1 \mathcal{O}_2 \rangle_c \sim \mathcal{O}(N^0) + \mathcal{O}(N^{-2}) + \cdots \tag{2.21}$$

$$\langle \mathcal{O}_1 \mathcal{O}_2 \mathcal{O}_3 \rangle_c \sim \mathcal{O}(N^{-1}) + \mathcal{O}(N^{-3}) + \cdots \tag{2.22}$$

All leading order contributions arise from planar diagrams.

Physical Implications :

1. In the large N limit, $\mathcal{O}(x)|0\rangle$ can be understood as generating a single-particle state (referred to as a "glue ball"). Similarly, $:\mathcal{O}_1 \cdots \mathcal{O}_n(x):|0\rangle$ denotes an n-particle state.
2. The fluctuations of “glue balls” are diminished.
3. If we regard it as the "scattering amplitude" of n "glueballs", then at the leading order in $N \to \infty$, the scattering involves only tree-level interactions (essentially classical) among the glueball states.

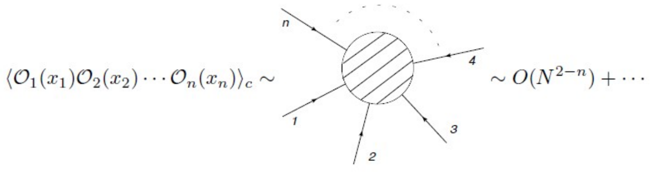
$\langle \mathcal{O}_1(x_1)\mathcal{O}_2(x_2)\cdots\mathcal{O}_n(x_n)\rangle_c \sim$
n
4
3
2
1
$\sim O(N^{2-n}) + \cdots$

   (a) Consider

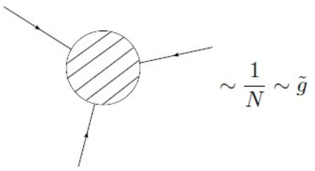
$\sim \frac{1}{N} \sim \tilde{g}$

If we consider it as a fundamental vertex with coupling $\tilde{g}$, then the tree-level amplitude for n-particle scattering scales as $\tilde{g}^{n-2} \sim N^{2-n}$.

(b) We can also incorporate higher-order vertices, but they must adhere to:

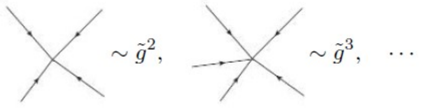

(c) There can be at most one-particle intermediate states. When we insert a complete set of states at all possible locations, the large N counting implies that all states other than single-particle ones are suppressed:

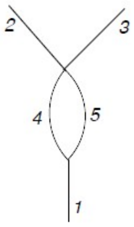

$$= \langle \mathcal{O}_1 : \mathcal{O}_4 \mathcal{O}_5 :\rangle \langle : \mathcal{O}_4 \mathcal{O}_5 : \mathcal{O}_2 \mathcal{O}_3 \rangle \sim O(N^{-3})$$

Compared to

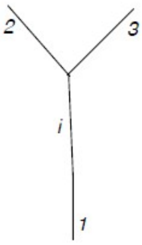

$$= \langle \mathcal{O}_1 \mathcal{O}_i \rangle \langle \mathcal{O}_i \mathcal{O}_2 \mathcal{O}_3 \rangle \sim O(N^{-1})$$

i.e. all “loops” of glue balls are suppressed.

More explicitly,

Gauge theory with finite $\hbar$ in the $N \to \infty$ limit $=$ Glue ball theory

Perturbative expansion in 1/N $=$ Loops of glue balls perturbative in $\hbar$

2.3 Large N Expansion As a String Theory

Quantum field theory (QFT) can be viewed as a framework describing "particles." While the conventional method of quantization is second quantization, first quantization directly involves quantizing the motion of a particle in spacetime. This involves

$$Z = \int DX^{\mu}(\tau) e^{iS_{particle}} \tag{2.23}$$

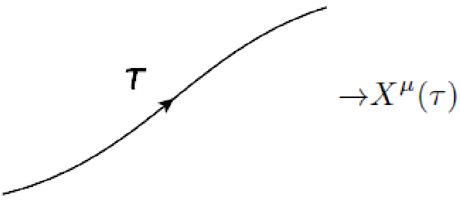

Where,

$$S_{particle} = m \int dl = m \int d\tau \frac{dl}{d\tau} = m \int d\tau \sqrt{g_{\mu\nu} \frac{dX^{\mu}}{d\tau} \frac{dX^{\nu}}{d\tau}} \tag{2.24}$$

To incorporate interactions such as $\lambda\phi^3$, we have to introduce them manually.

2.3.1 String Theory

Similarly, in string theory, we must quantize the motions of strings in space-time

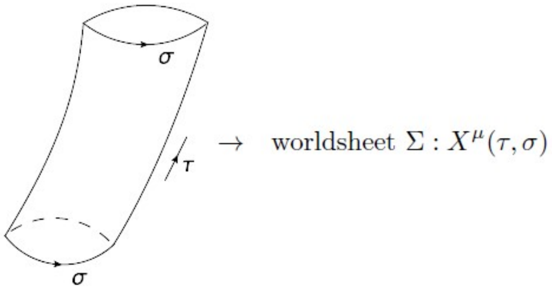

The most basic expression for S_{string} is the Nambu-Goto action.

$$S_{NG} = T \int_{\Sigma} dA \tag{2.25}$$

In this context, $T = \frac{1}{2\pi\alpha'}$ represents the string tension, which is the mass per unit length. The differential area $dA = \sqrt{-\det(h_{ab})}d\sigma d\tau$ corresponds to the infinitesimal area of the world sheet, calculated using the induced matrix $h_{ab} = g_{\mu\nu}\partial_a X^{\mu}\partial_b X^{\nu}$. To establish and compute eq. (2.23), the most practical approach is to transition to Euclidean signature. For vacuum processes:

$$Z_{string} = \sum_{\text{all closed surfaces}} e^{-S_{NG}} = \sum_{h=0}^{\infty} e^{-\lambda\chi} \sum_{\text{surfaces with given topology}} e^{-S_{NG}} \tag{2.26}$$

In this context, $\chi = 2 - 2h$ represents the weight associated with various topologies, where λ serves as an analog to a "chemical potential" for topology. If we express g_s as e^{λ}, the vacuum encompasses diagrams such as

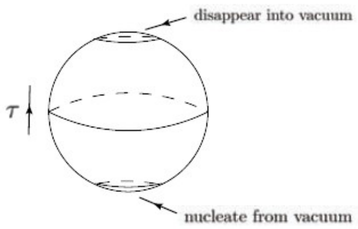

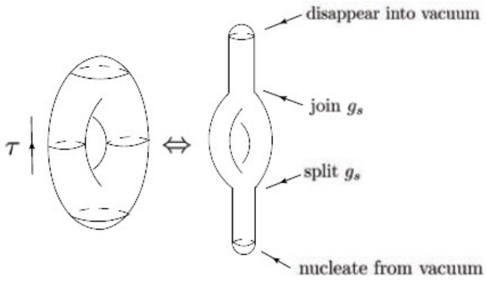

The surface acts as a vacuum bubble, where the string initiates from the vacuum at the south pole and merges back into it at the north pole. Torus, representing a one-loop diagram, the string splits into two before rejoining, with each vertex interaction strength g_s. Hence, the primary interaction points involve string splitting and recombination, with the coupling strength denoted as $g_s = e^{\lambda}$.

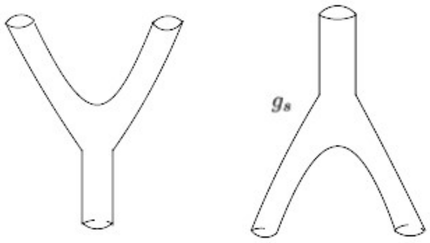

We now introduce external strings, such as:

$$\text{string} + \text{string} \to \text{string} + \text{string} \tag{2.27}$$

In the graphical representation:

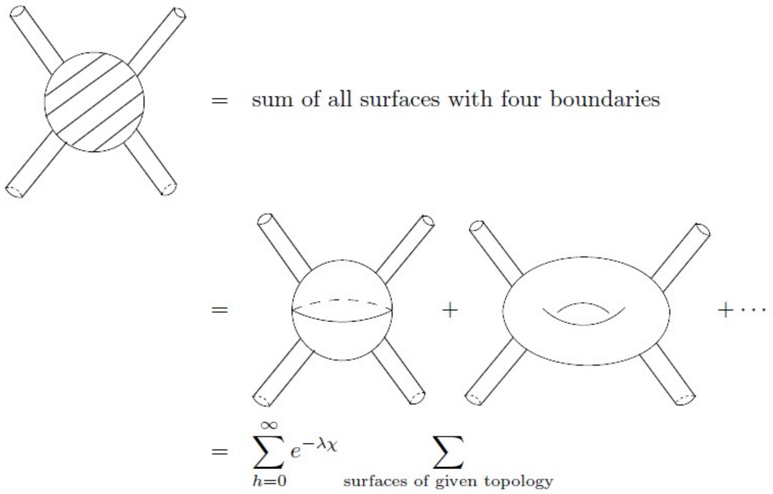
= sum of all surfaces with four boundaries
=
+
+ ⋯
$= \sum_{h=0}^{\infty} e^{-\lambda\chi} \sum_{\text{surfaces of given topology}}$

Here, $\chi = 2 - 2h - n$, where n represents the count of boundaries (the number of external strings).

Therefore, for a scattering process involving n strings (which includes vacuum processes, i.e., when $n = 0$)

$$\mathcal{A}_n = \sum_{h=0}^{\infty} g_s^{n-2+2h} F_n^{(h)} = \underbrace{g_s^{n-2} F_n^{(0)}}_{\substack{\text{tree-level diagrams}\\ \text{(sphere topology)}}} + \underbrace{g_s^{n} F_n^{(1)}}_{\substack{\text{1-loop diagrams}\\ \text{(torus topology)}}} + \underbrace{g_s^{n+2} F_n^{(2)}}_{\substack{\text{2-loop diagrams}\\ \text{(double torus topology)}}} \tag{2.28}$$

Now, in relation to our earlier discussion on the large N expansion of a gauge theory (including $n = 0$)

$$\begin{aligned}\langle \mathcal{O}_1(x_1)\mathcal{O}_2(x_2)\cdots\mathcal{O}_n(x_n)\rangle_c &= \sum_{h=0}^{\infty} N^{2-n-2h} f_n^{(h)} \\ &= \underbrace{N^{2-n} f_n^{(0)}}_{\substack{\text{planar diagrams} \\ \text{(sphere topology)}}} + \underbrace{N^{-n} f_n^{(1)}}_{\text{torus diagrams}} + \underbrace{N^{-n-2} f_n^{(2)}}_{\substack{\text{double-torus} \\ \text{diagrams}}}\end{aligned} \tag{2.29}$$

Upon comparing eq. [(2.28)] and [(2.29)], we observe a consistent mathematical framework in both theories, with the correspondence:

$$e^{\lambda} = g_s \leftrightarrow \frac{1}{N}$$

external strings ↔ “glue balls” (single trace operator) $\mathcal{O}_i(x)\,|0\rangle$

sum over string world sheet of given topology ↔ sum over Feynman diagrams of given topology

topology of the world sheet ↔ topology of Feynman diagrams

Remember that each Feynman diagram can be viewed as a partition of a surface with genus-h. The scattering amplitude of n particles on a surface with genus-h can be expressed as:

$$f_n^{(h} = \sum_{\text{all Feynman diagrams of genus-h}} G = \sum_{\text{all possible triangulations of genus-h surface}} G \tag{2.30}$$

In this context, G denotes the representation for each diagram. Likewise, in string theory, we encounter n-string scattering phenomena.

$$F_n^{(h} = \int_{\substack{\text{genus h surfaces}\\ \text{with n boundaries}}} DX e^{-S_{string}} = \sum_{\substack{\text{all possible triangulations of}\\ \text{genus-h surfaces with n boundaries}}} e^{-S_{string}} \tag{2.31}$$

If we manage to associate G with a certain $e^{-S_{string}}$, we would consequently obtain:

a large N gauge theory = a string theory

$\frac{1}{N}$ expansion = perturbative expansion in g_s

large N limit (classical theory of glue-balls) = classical string theory

single-trace operators (glueballs) = string states

Indeed, achieving this identification poses challenges:

- String theory operates within a continuous framework, whereas Feynman diagrams, at best, offer a discrete rendition (such as the triangulation of the manifold).
- The action S_{string} establishes a mapping from the world sheet Σ to the target space $\mathcal{M}$ (the spacetime manifold) $(\sigma, \tau) \rightarrow X^\mu(\sigma, \tau)$. Within such a mapping, we encounter options regarding the spacetime manifold $\mathcal{M}$, the specific formulations of the action S_{string}, and the possibility of "internal" degrees of freedom residing on the world sheet without direct spacetime correspondence. For instance, these could entail superstrings, involving fermions on the world sheet.

Generalizations:

1. Up to this point, our focus has primarily been on matrix-valued fields, specifically fields within the adjoint representation of the U(N) gauge group. However, one could incorporate fields in the fundamental representation (quarks).

$$q = \begin{bmatrix} q_1 \\ q_2 \\ \vdots \\ q_N \end{bmatrix}$$

   e.g. within vacuum diagrams, loops of quarks are now considered, which can be categorized topologically by 2D surfaces with boundaries. This scenario corresponds to a string theory encompassing both open and closed strings.

2. Up to this point, we focused on the U(N) gauge group.

$$\langle \Phi^{a}{}_{b}(x)\Phi^{c}{}_{d}(y)\rangle =$$

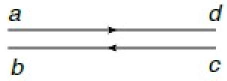

   If we were to examine SO(N) or SP(N) instead, there would be no divergence between the two indices of the fields.

$$\langle \Phi_{ab}\Phi_{cd}\rangle =$$

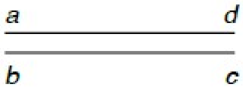

Consider, for example, the large N extension of QCD in 3+1 dimensional Minkowski spacetime. If the $\frac{1}{N}$ expansion could be characterized by a string theory, what implications would this hold?

A straightforward assumption would be a string theory situated in 3+1 dimensional Minkowski space.

$$ds^2 = -dt^2 + d\vec{x}^2 \tag{2.32}$$

We could explore either the Nambu-Goto action or the Polyakov action, which are classically equivalent to S_{NG}. However, this approach proves ineffective:

1. This type of string theory exhibits inconsistencies unless D (the dimension of spacetime) equals either 10 or 26.
2. Consider a string theory in 10 dimensions with $\mathcal{M}_4 \times \mathcal{N}$, where $\mathcal{N}$ represents a compact manifold. This theory includes a massless spin-2 particle (graviton) in $\mathcal{M}_4$, a feature absent in Yang-Mills theory.

To address this issue, we can explore either more unconventional string actions or alternative target spaces. Indeed, there are indications suggesting the consideration of a 5-dimensional string theory:

1. **Holographic principle:** String theory inherently includes gravity. In accordance with the holographic principle, the gravitational aspect of this theory is ideally represented in five dimensions for consistency.
2. **The consistency of string theory itself:** It needs the inclusion of a Liouville mode, which acts as an additional dimension.

In the context of a 5-dimensional spacetime, a string Y should exhibit all the symmetries found in 4-dimensional Yang-Mills theories, such as translations and Lorentz symmetries.

$$ds^2 = a^2(z)\left[dz^2 + \eta_{\mu\nu} dX^\mu dX^\nu\right] \tag{2.33}$$

This is the most general metric compatible with 4-dimensional Poincaré symmetries. However, if a theory exhibits conformal or scale invariance. Eq. (2.33) should represent the AdS metric. It is invariant under scaling transformations:

$$X^\mu = \lambda X^\mu \tag{2.34}$$

This implies that z transforms as $z \to \lambda z$, and $a(\lambda z) = \frac{1}{\lambda} a(z)$, indicating $a(z) = \frac{R}{z}$ with a constant R. Finally, as a concluding note, let's outline the historical journey leading to the discovery of holographic duality.

1974 (continued)

Lattice QCD (Wilson), confining strings

1993-1994

Holographic principle

(t' Hooft, Susskind)

1997 June

Need 5D string theory to describe QCD (Polyakov)

1995

D-branes (Polchinski)

1997 Nov

AdS/CFT (Maldacena)

1998 Feb

Connection between holographic principle and large N gauge theory/string theory duality (Witten)

3

AdS/CFT Conjecture

3.1 String Theory in the Perturbative (Bosonic) Regime

3.1.1 Overall Framework

Think about a string moving in a spacetime denoted as $\mathcal{M}$, characterized by a metric $(\mu, \nu = 0, 1, ..., d-1)$:

$$ds^2 = G_{\mu\nu} dX^\mu dX^\nu \tag{3.1}$$

With the world-sheet Σ parametrizations (a = 0, 1):

$$X^\mu(\sigma, \tau) = X^\mu(\sigma^a) \tag{3.2}$$

The induced metric on Σ is written as:

$$h_{ab} = G_{\mu\nu}\partial_a X^\mu \partial_b X^\nu, \quad ds^2 = h_{ab}(\sigma,\tau)d\sigma^a d\sigma^b \tag{3.3}$$

The action of the string is determined to be directly related to the area enclosed by Σ, expressed in the Nambu-Goto format as follows:

$$S_{NG}[X^\mu] = \frac{1}{2\pi\alpha'}\int_\Sigma dA \quad = \frac{1}{2\pi\alpha'}\int_\Sigma d^2\sigma\sqrt{-h}; \quad [\alpha'] = L^2 \rightarrow \alpha' = l_s^2, \quad T = \frac{1}{2\pi\alpha'} \tag{3.4}$$

where l_s represents the length scale of the string (derived from dimensional analysis), and T stands for the string tension. Here, $d^2\sigma = d\sigma d\tau$.

Because the non-polynomial structure of S_{NG} poses difficulties in calculations, it is more convenient to utilize Polyakov's action, which, at the classical level, is equivalent to the Nambu-Goto action. For calculation see A.1 :

$$S_P[\gamma^{ab}, X] = \frac{1}{4\pi\alpha'}\int d^2\sigma\sqrt{-\gamma}\gamma^{ab}\partial_a X^\mu \partial_b X^\nu G_{\mu\nu}; \quad \gamma^{ab} \equiv \gamma^{ab}(\sigma,\tau) \tag{3.5}$$

Equation of Motion for γ^{ab}:

$$\gamma_{ab} = \frac{\lambda}{2}h_{ab} \tag{3.6}$$

In this context, λ represents an arbitrary function. Thus, we have $\gamma^{ab}h_{ab} = \frac{2}{\lambda}\times 2$ and $\sqrt{-\gamma} = \frac{\lambda}{2}\sqrt{-h}$. Eq. (3.5) takes on the structure resembling that of a 2-dimensional scalar field theory within the curved spacetime Σ characterized by the metric γ_{ab}.

The quantization of the string path integral will adhere to this framework.

$$\int D\gamma^{ab} DX^{\mu} e^{iS_P[\gamma^{ab},X^{\mu}]} \dots \tag{3.7}$$

To gain a better understanding of the physical spectrum of strings, canonical quantization proves to be a more suitable approach. The Polyakov Lagrangian:

$$S_P = \int_{\Sigma} d^2\sigma \mathcal{L}_P \tag{3.8}$$

Symmetries of eq. (3.5) :

1. Global Poincare transformation (translation and Lorentz rotation):

$$X^{\mu}(\sigma,\tau) \rightarrow X^{\mu} + a^{\mu}; \quad X^{\mu} \rightarrow \Lambda^{\mu}_{\nu} X^{\nu} \tag{3.9}$$

2. Local diffeomorphism transformation ($\sigma^a \rightarrow \sigma'^a$) :

$$X^{\mu}(\sigma,\tau) \rightarrow X'^{\mu}(\sigma',\tau') = X^{\mu}(\sigma,\tau); \quad \gamma^{ab} \rightarrow \gamma'^{ab} = \frac{\partial\sigma'^a}{\partial\sigma^c}\frac{\partial\sigma'^b}{\partial\sigma^d}\gamma^{cd}(\sigma,\tau) \tag{3.10}$$

3. Local Weyl transformation:

$$\gamma^{ab} \rightarrow e^{-2\omega(\sigma,\tau)}\gamma^{ab}(\sigma,\tau) \tag{3.11}$$

These symmetries (Poincaré and Diff × Weyl) can serve as the guiding principles that (almost) uniquely determine the string action in eq. (3.5). For instance, when considering a topological invariant of 2D oriented closed surfaces, the 2D

Einstein-Hilbert action also aligns with this criterion.

$$S_\chi[\gamma^{ab}] = \lambda \left(\frac{1}{4\pi} \int_\Sigma d^2\sigma \sqrt{-\gamma} R \right) = \lambda_\chi \left(\Sigma\right); \quad \chi\left(\Sigma\right) = 2 - 2g \tag{3.12}$$

Here, R = Ricci scalar.

3.2 Light-Cone Quantization

Every distinct oscillation mode exhibited by a string correlates with a particle existing within space-time. In the case of massless modes, a closed string represents a spin 2 particle (such as the graviton), while an open string represents a spin 1 particle (like a gauge particle, such as the photon or gluon).

The process of canonical quantization involves the following steps:

1. Formulate the classical equation of motion.
2. Address the gauge symmetries.
3. Determine the entire set of classical solutions.
4. Elevate classical fields (on the world-sheet) to quantum operators, adhering to canonical quantization criteria. The classical solutions then transform into solutions to operator equations, and the parameters within classical solutions transition into creation and annihilation operators.
5. Extract the spectrum by applying creation operators to the vacuum of the (2D world-sheet) theory.

The classical equation of motion from eq. (3.5)

1. For γ^{ab} :

$$0 = T_{ab} = \partial_a X^\mu \partial_b X_\mu - \frac{1}{2}\gamma_{ab}\gamma^{cd}\partial_c X^\mu \partial_d X_\mu \tag{3.13}$$

2. For X^μ :

$$\partial_a\left(\sqrt{-\gamma}\gamma^{ab}\partial_b X^\mu\right) = 0 \tag{3.14}$$

Through diffeomorphism, the metric can be transformed into the conformally flat form $\gamma_{ab} = e^{2\omega(\sigma,\tau)}\eta_{ab}$, and Weyl rescaling enables the attainment of $\gamma_{ab} = \eta_{ab}$. Now, referring to equation (3.14)

$$\partial_\tau^2 X^\mu - \partial_\sigma^2 X^\mu = 0 \tag{3.15}$$

From eq. (3.13), we get,

$$T_{00} = T_{11} = \frac{1}{2}\left(\partial_\tau X^\mu \partial_\tau X_\mu + \partial_\sigma X^\mu \partial_\sigma X_\mu\right) = 0 \tag{3.16}$$

$$T_{\tau\sigma} = T_{\sigma\tau} = \partial_\tau X^\mu \partial_\sigma X_\mu = 0 \tag{3.17}$$

Equations (3.16) and (3.17) represent the Virasoro constraints. In the case of an open string with Neumann boundary conditions $\partial_\sigma X^\mu(\sigma = 0, \pi; \tau) = 0$, equation (3.15) can be readily resolved (x^μ, v^μ can be arbitrary constants):

$$X^\mu(\sigma,\tau) = x^\mu + v^\mu\tau + X_R^\mu(\tau-\sigma) + X_L^\mu(\tau+\sigma) \tag{3.18}$$

In the scenario of closed strings, X_R and X_L represent independent periodic functions over the interval of 2π. When implementing Neumann boundary conditions for open strings, we obtain

$$X'_L(\tau) = X'_R(\tau) \;\text{ at } \sigma = 0 \tag{3.19}$$

$$X'_L(\tau - \pi) = X'_R(\tau + \pi) \;\text{ at } \sigma = \pi \tag{3.20}$$

We get $X_L = X_R$ and is periodic in 2π.

3.2.1 Light Cone Gauge

Even after determining the worldsheet metric, there remains additional gauge freedom known as conformal symmetry. Let's introduce:

$$\sigma^{\pm} = \frac{\tau \pm \sigma}{\sqrt{2}}; \quad ds^2 = -d\tau^2 + d\sigma^2 = -2d\sigma^+ d\sigma^- \tag{3.21}$$

Therefore, this symmetry can be interpreted as the preservation of $\gamma^{ab} = \eta^{ab}$ (subject to a Weyl rescaling) as:

$$\sigma^+ \to \tilde{\sigma}^+ = f(\sigma^+); \quad \sigma^- \to \tilde{\sigma}^- = g(\sigma^-); \quad ds^2 \to -2\partial_+ f \partial_- g d\sigma^+ \sigma^- \tag{3.22}$$

$$\tilde{\tau} = \frac{f(\tau + \sigma) + g(\tau - \sigma)}{\sqrt{2}} \Rightarrow \tau \tag{3.23}$$

If this matches the classical solution of X^{μ}, one can fully specify the gauge by selecting suitable functions f and g such that:

$$\tau = \frac{X^+}{v^+}; \quad X^{\pm} = \frac{X^0 \pm X^1}{\sqrt{2}} \tag{3.24}$$

This gauge is termed the light-cone gauge, as it sets the worldsheet time according to the spacetime light-cone coordinate. With $X^\mu = (X^+, X^-, X^i)$ (the transverse directions $i = 2, 3, \cdots, d-1$): $dX^\mu dX_\mu = -2dX^+dX^- + dX^idX^i$. In this gauge, the Virasoro constraints (3.16) and (3.17) simplify,

$$2v^+\partial_\tau X^- = \left(\partial_\tau X^i\right)^2 + \left(\partial_\sigma X^i\right)^2 \tag{3.25}$$

$$v^+\partial_\sigma X^- = \partial_\sigma X^i \partial_\sigma X^i \tag{3.26}$$

The degrees of freedom that are independent are denoted by X^i. Due to the “wrong” sign in its kinetic terms, X^0 among these degrees of freedom doesn’t effectively address a unitarity issue at the quantum level.

Expanding equation (3.18) in a Fourier series, in the case of closed strings, we obtain

$$X^\mu(\sigma,\tau) = X^\mu + v^\mu\tau + i\sqrt{\frac{\alpha'}{2}}\sum_{n\neq 0}\frac{1}{n}\left(\alpha_n^\mu e^{-in(\tau+\sigma)} + \tilde{\alpha}_n^\mu e^{-in(\tau-\sigma)}\right) \tag{3.27}$$

It’s similar for open string, but from $X_R^\mu = X_L^\mu$ one arrives at $\alpha_n^\mu = \tilde{\alpha}_n^\mu$:

$$X^\mu(\sigma,\tau) = X^\mu + v^\mu\tau + i\sqrt{2\alpha'}\sum_{n\neq 0}\frac{1}{n}\alpha_n^\mu e^{-in\tau}\cos n\sigma \tag{3.28}$$

The center of mass motion can be determined by computing the average position of the strings across a particular time slice ($l = 2\pi$ for closed strings and $l = \pi$ for open strings):

$$\frac{1}{l}\int_0^l d\sigma X^\mu(\sigma,\tau) = x^\mu + v^\mu\tau \tag{3.29}$$

The parameter v^μ is associated with the velocity of the strings’ center of mass.

The classical coefficients α_n^μ and $\tilde{\alpha}_n^\mu$ monitor the oscillation patterns of the strings. While closed strings exhibit distinct left-moving and right-moving components, open strings can be likened to standing waves, implying that left-moving and right-moving contributions are equivalent.

In the light-cone gauge, $X^+ = v^+\tau$, and X^- is obtained by expanding X^- in a Fourier series. By substituting equations (3.27) and (3.28) into equations (3.25) and (3.26), and then equating the coefficients of different Fourier modes, X^- is determined. The zeroth (non-oscillating) mode establishes the relationship between the velocity of the strings' center of mass and the strings' oscillation modes.

$$2v^+v^- = v_i^2 + 2\alpha' \sum_{m\neq 0} \alpha_{-m}^i \alpha_m^i \quad \text{(open)} \tag{3.30}$$

$$2v^+v^- = v_i^2 + \alpha' \sum_{m\neq 0} \left(\alpha_{-m}^i \alpha_m^i + \tilde{\alpha}_{-m}^i \tilde{\alpha}_m^i\right) \quad \text{(closed)} \tag{3.31}$$

The Poincaré global symmetries present in the action correspond to conserved currents on the worldsheet. For now, let's focus on translation and employ the conventional Noether method:

$$\Pi_a^\mu = \frac{1}{2\pi\alpha'}\partial_a X^\mu \tag{3.32}$$

It's worth mentioning that $\partial^a \Pi_a^\mu = 0$, a consequence of the equation of motion for X^μ. Π_τ^μ represents the momentum density along the string, and the associated conserved current signifies the string momentum in space-time:

$$p^\mu = \int_0^l d\sigma \Pi_\tau^\mu = \frac{l}{2\pi}\frac{v^\mu}{\alpha'} \tag{3.33}$$

The mass squared is linked to the spacetime momentum of the strings, characterized by the mass shell condition: $M^2 = -p^\mu p_\mu = 2p^+p^- + p_i^2$

$$M^2 = \frac{1}{2\alpha'} \sum_{m\neq 0} \alpha_{-m}^i \alpha_m^i \ \text{(open)} \tag{3.34}$$

$$M^2 = \frac{1}{\alpha'} \sum_{m\neq 0} \left[\alpha_{-m}^i \alpha_m^i + \tilde{\alpha}_{-m}^i \tilde{\alpha}_m^i\right] \ \text{(closed)} \tag{3.35}$$

3.2.2 Quantization :

Once the classical behavior of the strings has been comprehended, the subsequent stage involves quantization - namely, quantizing the independent degrees of freedom $X^i(\sigma, \tau)$ (alongside their canonical momentum density Π^i) within the action:

$$S = -\frac{1}{4\pi\alpha'} \int d^2\sigma \partial^a X^i \partial_a X^i; \quad \Pi^i = \frac{1}{2\pi\alpha'} \partial_\tau X^i \tag{3.36}$$

Designate X^i as a quantum operator, with the canonical commutation relation on a specific time slice:

$$\begin{aligned} \left[X^i(\sigma,\tau), X^j(\sigma',\tau)\right] = \left[\Pi^i(\sigma,\tau), \Pi^j(\sigma',\tau)\right] = 0; \\ \left[X^i(\sigma,\tau), \Pi^j(\sigma',\tau)\right] = i\delta^{ij}\delta(\sigma - \sigma') \end{aligned} \tag{3.37}$$

The outcomes indicate that the zeroth mode x^i, p^i, and the oscillation modes α^i and $\tilde{\alpha}^i$ are all transformed into operators:

$$\left[x^i, p^j\right] = i\delta^{ij}; \quad \left[\alpha_n^i, \alpha_m^j\right] = \left[\tilde{\alpha}_n^i, \tilde{\alpha}_m^j\right] = n\delta^{ij}\delta_{n+m,0} \tag{3.38}$$

It's important to recognize that α^i and $\tilde{\alpha}^i$ can be associated with creation and annihilation operators:

$$\frac{1}{\sqrt{n}}\alpha_n^i = a_n^i; \quad \frac{1}{\sqrt{n}}\alpha_{-n}^i = \left(a_{-n}^i\right)^\dagger; \quad \frac{1}{\sqrt{n}}\tilde{\alpha}_{-n}^i = \left(\tilde{a}_{-n}^i\right)^\dagger; \quad \frac{1}{\sqrt{n}}\tilde{\alpha}_n^i = \tilde{a}_n^i \tag{3.39}$$

Hence, the vacuum state of the oscillator (indexed by string spacetime momentum p^μ) meets:

$$\alpha_n^i \left|0, p^\mu\right\rangle = \tilde{\alpha}_n^i \left|0, p^\mu\right\rangle = 0, \quad n > 0 \tag{3.40}$$

Excited states can be constructed using creation operators ($\alpha_{-n}^i, \tilde{\alpha}_{-n}^i$ with $n > 0$) :

$$\alpha_{-n_1}^{i_1}\alpha_{-n_2}^{i_2}\cdots\tilde{\alpha}_{-m_1}^{j_1}\tilde{\alpha}_{-m_2}^{j_2}\cdots\left|0, p^\mu\right\rangle \tag{3.41}$$

Define the operator for the number of oscillations for closed strings (no summation in the index i, and the order of operators is crucial).

$$N_n^i = \frac{1}{n}\alpha_{-n}^i\alpha_n^i; \quad \tilde{N}_n^i = \frac{1}{n}\tilde{\alpha}_{-n}^i\tilde{\alpha}_n^i \tag{3.42}$$

The quantum expression for the mass shell condition of closed strings is given by:

$$M^2 = \frac{2}{\alpha'}\sum_{i=2}^{D-1}\sum_{n\neq 0} n\left(N_n^i + \tilde{N}_n^i\right) + a_0 \tag{3.43}$$

The constant a_0 represents the zero-point energy for closed strings, derived from rearranging the operator to normal order.

$$a_0 = \frac{2(D-2)}{\alpha'}\sum_{n=1}^{\infty} n = -\frac{(D-2)}{24}\frac{4}{\alpha'} \tag{3.44}$$

Similarly for open string,

$$M^2 = \frac{1}{\alpha'} \sum_{i=2}^{D-1} \sum_{m=1}^{\infty} m N_m^i + a_0 \tag{3.45}$$

The constant a_0 is determined as:

$$a_0 = \frac{(D-2)}{2\alpha'} \sum_{n=1}^{\infty} n = -\frac{(D-2)}{24} \frac{1}{\alpha'} \tag{3.46}$$

The spectrum of the string can be determined by observing that each state of the string corresponds to a particle state in spacetime.

Let's begin by examining the particle composition of open strings:

1. The oscillation vacuum state is:

   $$|0, p^\mu\rangle\, ; \;\; N_m^i = 0; \;\; \forall m, i \tag{3.47}$$

   The spacetime transformation of this state implies it should be a scalar with mass: $M^2 = -\frac{D-2}{24\alpha'}$. When $D > 2$, this particle is a tachyon since $M^2 < 0$.

2. The first excited state of oscillation transforms into a $SO(D-2)$ vector under spacetime rotations: $\alpha_{-1}^i |0, p^\mu\rangle$, with $M^2 = -\frac{D-2}{24\alpha'}$. Given that the first excited state is a vector with only $D-2$ independent components, for consistency with Lorentz symmetries or the quantization process, it should be massless: $M^2 = 0 \Rightarrow D = 26$. This outcome for the spacetime dimension is referred to as the critical dimension of (bosonic) string theory. The coherent state formed by many of these particles in spacetime yields the field configuration of a massless vector field A_μ, which later assumes the roles of a gauge boson (such as the photon and gluon).

3. Higher energy states are all massive and form multiplets with mass-squared intervals of $\frac{1}{\alpha'}$. The particle representation of the second excited state of the string (massive) includes $\alpha_{-1}^{i}\alpha_{-1}^{j}\left|0,p^{\mu}\right\rangle$, $\alpha_{-2}^{i}\left|0,p^{\mu}\right\rangle$, where $M^2=\frac{1}{\alpha'}$.

Similarly, the particle composition of closed strings can also be deduced.

1. The oscillation vacuum state is:

$$\left|0,p^{\mu}\right\rangle;\ \ N_m^i=\tilde{N}_m^i=0;\ \ \forall m,i \tag{3.48}$$

   The transformation of this state in spacetime suggests that it should be a spacetime scalar with mass: $M^2=-\frac{D-2}{6\alpha'}$. As with the open string, when $D>2$, this particle is a tachyon due to $M^2<0$.

2. The first excited state of oscillation is: (utilizing the level matching condition) $\alpha_{-1}^{i}\tilde{\alpha}_{-1}^{j}\left|0,p^{\mu}\right\rangle$, with $M^2=\frac{26-D}{6\alpha'}$. Only for $D=26$, this state aligns with the irreducible representations of $SO(D-2)$ of the Lorentz group consistently (as massless $M^2=0$ spin 2 particles), with further decomposition into scalar (trace), symmetric traceless, and antisymmetric components: $\sum_i^{24}\alpha_{-1}^{i}\tilde{\alpha}_{-1}^{i}\left|0,p^{\mu}\right\rangle$, $\alpha_{-1}^{i}\tilde{\alpha}_{-1}^{j}e_{ij}\left|0,p^{\mu}\right\rangle$, $\alpha_{-1}^{i}\tilde{\alpha}_{-1}^{j}b_{ij}\left|0,p^{\mu}\right\rangle$. The coherent state formed by many of these particles in spacetime represents the field configuration of a massless scalar field Φ (dilaton), a traceless symmetric tensor field $G_{\mu\nu}$ (graviton), and an antisymmetric tensor field $B_{\mu\nu}$ (Kalb-Ramon, or B-field), associated with gauge symmetries.

3. The higher-energy states are all massive, organized into multiplets with mass-squared intervals of $\frac{4}{\alpha'}$. For instance, the particle representation of the second

excited state of the string (which is massive) includes $\alpha^i_{-1}\alpha^j_{-1}\tilde{\alpha}^k_{-1}\tilde{\alpha}^l_{-1}\left|0,p^\mu\right\rangle$, $\alpha^i_{-2}\tilde{\alpha}^k_{-1}\tilde{\alpha}^l_{-1}\left|0,p^\mu\right\rangle$, $\alpha^i_{-1}\alpha^j_{-1}\tilde{\alpha}^k_{-2}\left|0,p^\mu\right\rangle$, where $M^2 = \frac{4}{\alpha'}$. This aligns with the description of massive spin 4 particles in $D = 26$ Lorentz irreducible groups, forming complete multiplets of $SO(25)$. The same consistency holds for particles with higher spins (masses).

At energies significantly lower than $\frac{1}{\alpha'}$, the behavior of A_μ and $G_{\mu\nu}$ should be dictated by Maxwell and Einstein's theories. This assertion is supported by explicit calculations of scattering amplitudes involving these particles in string theory ($g_s \ll 1$). Additionally, we find that $G_N \propto g_s^2$ and $g_s = e^{\langle\Phi\rangle}$.

Various quantization approaches exist without the presence of tachyons, and IIA and IIB refer to prospective perturbative superstring theories. Both of them mandate that the critical dimension be $D = 10$.

The massless fields of the closed superstring (bosonic) in spacetime are:

1. For IIA superstring:

$$\Phi,\ G_{\mu\nu},\ B_{\mu\nu},\ A_\mu,\ C^{(3)}_{\mu\nu\lambda} \tag{3.49}$$

   A_μ and $C^{(3)}_{\mu\nu\lambda}$ are the RR fields.

2. For IIB superstring:

$$\Phi,\ G_{\mu\nu},\ B_{\mu\nu},\ \chi,\ C^{(2)}_{\mu\nu},\ C^{(4)}_{\mu\nu\lambda\sigma} \tag{3.50}$$

   $\chi, C^{(2)}_{\mu\nu}$ and $C^{(4)}_{\mu\nu\lambda\sigma}$ are the RR fields.

The effective field theories at low energies emerging from these superstring theories are known as IIA and IIB supergravity.

3.3 D-Branes

We encounter two significant boundary conditions:

1. The Dirichlet condition (D-condition) applied to the endpoints of open strings ($\sigma_{end} = 0, \pi$) in spatial direction, where $\delta X^i = 0 \to X^i(\sigma_{end}, \tau) =$ const.
2. The Neumann condition (N-condition) for the endpoints of open strings ($\sigma_{end} = 0, \pi$), where $\partial_\sigma \delta X^\mu = 0$.

We'll begin with the D-condition.

The implication is that the endpoint is confined to a hypersurface or a p-dimensional surface, termed a "spacetime defect", where open strings terminate. This appears to be a degree of freedom distinct from the perturbative string perspective. Such an entity is referred to as a D-brane, with a D_p-brane representing a D-brane with p spatial directions.

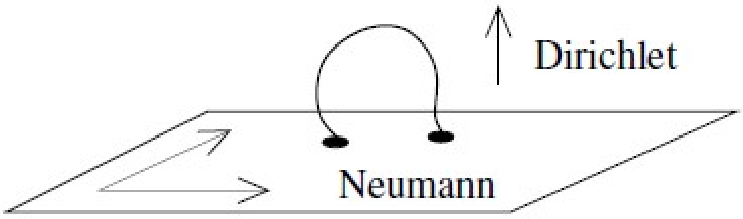

Figure 3.1: D-brane

1. Suppose in all directions we have

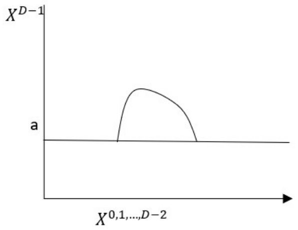

$$X^{0,1,\cdots,D-2} = N \text{ for } \sigma = 0, \pi \tag{3.51}$$

$$X^{D-1} = a \text{ for } \sigma = 0, \pi \tag{3.52}$$

2.

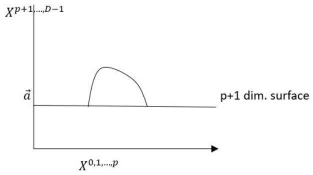

$$X^{0,1,\cdots,p} = N \text{ for } \sigma = 0, \pi \tag{3.53}$$

$$X^{p+1,p+2,\cdots,D-1} = \vec{a} \text{ for } \sigma = 0, \pi \tag{3.54}$$

3. If the N-condition holds for the end of an open string in all directions, it suggests an open string can end anywhere, termed as a space-filling brane (like a D25-brane, as the number of spatial dimensions is 25 in bosonic string theory) with complex dynamics. This implies that strings, initially closed, can only open up at specific spacetime locations where D-branes reside.

4. In Lorentzian spacetime, the existence of a D(-1)-brane is untenable as it's not a stable entity; it only manifests momentarily in time. This is because time in the target space cannot remain constant, rendering the condition X^0 = const. impossible.

5. A D0-brane corresponds to a particle, while a D1-brane represents a string; likewise, a D2-brane signifies a membrane, and so on.

6. When considering multiple D-branes, we encounter 4 distinct types of open strings.

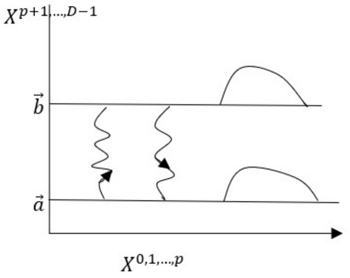

$$X^{0,1,\cdots,p} = N \text{ for } \sigma = 0, \pi \tag{3.55}$$

$$X^{p+1,p+2,\cdots,D-1} = \vec{a} \text{ for } (\sigma = 0, \tau) \tag{3.56}$$

$$= \vec{b} \text{ for } (\sigma = \pi, \tau) \tag{3.57}$$

7. D-branes of different dimensions

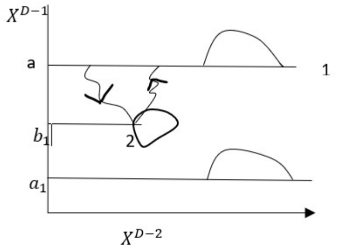

$$X^{D-2} = N \text{ for } (\sigma = 0, \tau) \tag{3.58}$$

$$X^{D-2} = a_1 \text{ for } (\sigma = \pi, \tau) \tag{3.59}$$

A D_p-brane disrupts the translational and Lorentz symmetries of the original $Mink_D$ to Poincaré$(1, p) \times SO(D-1-p)$.

What D-brane tells us ?

The presence of the D-brane leads to two significant insights. Firstly, it refines the GKP-Witten relation:

$$Z_{\mathcal{N}_4} = Z_{AdS_5 \times S^5} \tag{3.60}$$

Here, the left-hand side represents the partition function of $\mathcal{N} = 4$ SYM, while the right-hand side corresponds to the partition function of string theory on $AdS_5 \times S^5$.

Secondly, through the D-brane, we derive the AdS/CFT dictionary. Often, the S^5 is compactified, leading to a five-dimensional gravitational theory known as gauged supergravity.

The actual process of compactifying S^5 is intricate, as is the complete gauged supergravity action.

Part II

4

Introduction

In Part 2, we shift our focus to the specific properties of anti-de Sitter (AdS) spacetime and black holes within this framework. AdS spacetime, characterized by its negative cosmological constant, serves as a crucial arena for studying the AdS/CFT correspondence due to its rich geometric structure and well-understood boundary behavior. Within this backdrop, we investigate the thermodynamic properties of AdS black holes, their perturbations, and their quasi-normal modes.

By exploring various perturbations of AdS black holes, including scalar, vector, electromagnetic, and gravitational perturbations, we aim to elucidate the stability and dynamical behavior of these gravitational objects.

Furthermore, we employ novel techniques to calculate the quasi-normal modes of Kerr black holes, departing from traditional methods such as Leaver's method. By leveraging insights from AdS/CFT correspondence, we extend our analysis to Kerr-Sen black holes, shedding light on Kerr BH's quasi-normal modes and Love numbers.

5

The AdS spacetime

So, what exactly is Anti-deSitter (AdS) spacetime?

AdS_{d+1} denotes a maximally symmetric spacetime characterized by negative curvature. It emerges as a solution to Einstein's equations featuring a negative cosmological constant.

5.1 Spacetimes with constant curvature

Now, let's contemplate spacetimes characterized by constant curvature. The AdS_2 spacetime is capable of being embedded within a flat spacetime featuring two timelike directions, as illustrated in Fig. 5.1.

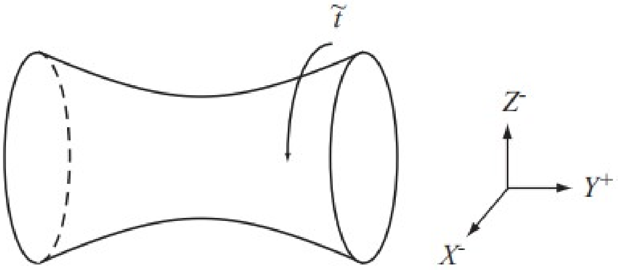

Figure 5.1: The inclusion of AdS_2 within $\mathbb{R}^{2,1}$. Since the temporal axis $\tilde{t}$ displays periodic behavior, we investigate the covering space.

$$ds^2 = -dZ^2 - dX^2 + dY^2 \tag{5.1}$$

$$-Z^2 - X^2 + Y^2 = L^2 \tag{5.2}$$

The parameter L is denoted as the AdS radius. AdS_2 spacetime exhibits $SO(2,1)$ symmetry. Similar to S^2 and H^2, we establish a coordinate system

$$Z = L\cosh\rho\cos\tilde{t}, \quad X = L\cosh\rho\sin\tilde{t}, \quad Y = L\sinh\rho \tag{5.3}$$

Then, the metric becomes

$$ds^2 = L^2(-\cosh^2\rho d\tilde{t}^2 + d\rho^2) \tag{5.4}$$

This coordinate system $(\tilde{t}, \rho)$ is referred to as the global coordinates. Despite embedding the AdS spacetime into a flat spacetime with two timelike directions X and Y, the AdS spacetime itself possesses only one timelike direction.

From Eq. (5.3), it's apparent that the coordinate $\tilde{t}$ exhibits periodicity 2π, rendering the timelike direction periodic. This presents causal difficulties, leading to the customary unwrapping of the timelike direction and consideration of the covering space of the AdS_2 spacetime, where $-\infty < \tilde{t} < \infty$. In the context of AdS/CFT, this covering space represents the AdS spacetime. AdS_2 spacetime demonstrates a constant negative curvature $R = -2/L^2$.

While AdS_5 spacetime is often considered for applications involving AdS/CFT, but the dS_4 spacetime is typically preferred for cosmological applications.

5.2 Various coordinate systems of AdS spacetime

Up to this point, we've examined the AdS spacetime utilizing the global coordinates. However, numerous other coordinate systems are found in the literature.

Static coordinates: $(\tilde{t}, \tilde{r})$. The coordinate $\tilde{r}$ is given by $\tilde{r} = \sinh\rho$. Consequently, the metric transforms to:

$$\frac{dS^2}{L^2} = -\left(\tilde{r}^2 + 1\right) d\tilde{t}^2 + \frac{d\tilde{r}^2}{\tilde{r}^2 + 1} \tag{5.5}$$

This coordinate system proves beneficial for comparison with the AdS black hole.

Conformal coordinates: $(\tilde{t}, \theta)$. The coordinate θ is determined by $\tan\theta = \sinh\rho$ with θ ranging from $-\pi/2$ to $\pi/2$. Consequently, the metric becomes flat with an overall factor (conformally flat):

$$\frac{dS^2}{L^2} = \frac{1}{\cos^2\theta}\left(-d\tilde{t}^2 + d\theta^2\right) \tag{5.6}$$

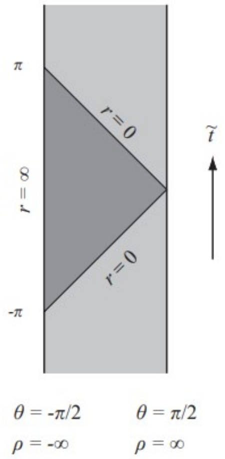

Figure 5.2: The AdS_2 spacetime represented in conformal coordinates. Poincaré coordinates only encompass a portion of the complete AdS spacetime, illustrated by the dark shaded region (Poincaré patch).

The AdS spacetime is depicted in Fig. 5.2 within this coordinate framework. Notably, the presence of a spatial "boundary" at $\theta = \pm\pi/2$ is crucial. This boundary is referred to as the AdS boundary.

Poincare coordinates : (t, r) this coordinate system is defined by

$$Z = \frac{Lr}{2}\left(-t^2 + \frac{1}{r^2} + 1\right) \tag{5.7}$$

$$X = Lrt \tag{5.8}$$

$$Y = \frac{Lr}{2}\left(-t^2 + \frac{1}{r^2} - 1\right) \tag{5.9}$$

$(r > 0, t : -\infty \to \infty)$. The metric becomes

$$\frac{dS^2}{L^2} = -r^2 dt^2 + \frac{dr^2}{r^2} \tag{5.10}$$

This coordinate system is widely used in AdS/CFT applications. It also proves beneficial for comparing with the AdS black hole.

5.3 Maximally symmetric spacetimes

We observed that these spacetimes possess a multitude of symmetries akin to S^2. They are termed maximally symmetric spacetimes, accommodating the highest count of symmetry generators. For instance, Minkowski spacetime, with constant curvature (specifically $R = 0$), qualifies as a maximally symmetric space. The (p + 2)-dimensional Minkowski spacetime exhibits $ISO(1, p{+}1)$ Poincaré invariance. The total number of symmetry generators amounts to $(p + 1)(p + 2)/2$ for $SO(1, p + 1)$ and (p + 2) for translations, thus totaling $(p + 2)(p + 3)/2$, representing the maximum number of generators.

6

The AdS black hole

Black holes have the potential to manifest within AdS spacetime. One of the most basic examples of an AdS black hole is referred to as the Schwarzschild-AdS black hole (hereafter abbreviated as SAdS black hole). Similar to the Schwarzschild black hole, AdS black holes can be conceptualized with a spherical horizon, but our focus here is on AdS black holes with a planar horizon or AdS black branes.

The SAdS_5 black hole emerges as a solution to the Einstein equation within a context of negative cosmological constant, akin to the AdS_5 spacetime. The specific metric is expressed as follows:

$$ds_5^2 = -\left(\frac{r}{L}\right)^2 h(r)dt^2 + \frac{dr^2}{\left(\frac{r}{L}\right)^2 h(r)} + \left(\frac{r}{L}\right)^2 \left(dx^2 + dy^2 + dz^2\right) \tag{6.1}$$

$$\text{Here, } h(r) = 1 - \left(\frac{r_0}{r}\right)^4 \tag{6.2}$$

The horizon exists at $r = r_0$. When $r_0 = 0$, the metric simplifies to AdS_5 spacetime. The g_{00} component includes $r_0^4/(L^2 r^2)$. The behavior of $\mathcal{O}(r^{-2})$ originates from the Newtonian potential, following a r^{-2} pattern in five-dimensional spacetime. Coordinates (x, y, z) represent $\mathbb{R}^3$. Unlike the Schwarzschild black hole, where $r^2 d\Omega^2$ indicates a spherical horizon, here the $r = r_0$ horizon extends indefinitely in (x, y, z) directions. Despite AdS spacetime's constant curvature, $SAdS_5$ black hole deviates, marked by a curvature singularity at $r = 0$.

6.1 Thermodynamic quantities of AdS black hole

Here, we analyze the thermodynamic properties of the $SAdS_5$ black hole, which, in AdS/CFT correspondence, correspond to the thermodynamic characteristics of the dual $\mathcal{N} = 4$ SYM theory at strong coupling. To bridge black hole outcomes with gauge theory results, establishing parameter relations between the two theories is essential.

$$N_c^2 = \frac{\pi}{2}\frac{L^3}{G_5}, \quad \lambda = \left(\frac{L}{l_s}\right)^4 \tag{6.3}$$

These connections are referred to as the AdS/CFT correspondence. On the left side, gauge theory parameters are expressed in relation to gravity parameters on the right side.

First, the temperature is given by

$$\begin{aligned} T &= \frac{f'(r_0)}{4\pi} && (6.4)\\ &= \frac{1}{4\pi}\frac{1}{L^2}\left(2r + \frac{2r_0^4}{r^3}\right)\Big|_{r=r_0} && (6.5)\\ &= \frac{1}{\pi}\frac{r_0}{L^2} && (6.6) \end{aligned}$$

For this black hole, the horizon extends infinitely, resulting in divergent entropy. Hence, using entropy density s is more appropriate. Spatially, the black hole is confined within $0 \leq x, y, z \leq L_x, L_y, L_z$, acting as an infrared cutoff. The gauge theory volume, $V_3 := L_x L_y L_z$, is distinguished from the horizon "area" due to the line element $(r/L)^2(dx^2 + dy^2 + dz^2)$. From area law

$$\begin{aligned} S &= \frac{A}{4G_5} = \frac{1}{4G_5}\left(\frac{r_0}{L}\right)^3 V_3 && (6.7)\\ \Rightarrow s &= \frac{S}{V_3} = \frac{1}{4G_5}\left(\frac{r_0}{L}\right)^3 && (6.8)\\ &= \frac{a}{4G_5} && (6.9) \end{aligned}$$

Here, $a = A/V_3$ represents the “horizon area density”. Employing the temperature (6.6) and the AdS/CFT dictionary, we obtain:

$$s = \frac{\pi^2}{2} N_c^2 T^3 \qquad (6.10)$$

Other thermodynamic properties can be established through related principles. For example, utilizing the first law, $d\varepsilon = T ds$, we can derive the energy density as shown below:

$$\varepsilon = \frac{3}{8}\pi^2 N_c^4 T^3 \qquad (6.11)$$

By employing the Euler relation, $\varepsilon = Ts - P$, the pressure can be deduced as $P = \frac{1}{3}\varepsilon$.

6.2 AdS Black Holes and Thermality

Let's initiate a conceptual experiment. Imagine a CFT residing on the Lorentzian cylinder $R \times S^{d-1}$, gradually raising its temperature. As the dilatation operator acts as the Hamiltonian, with increasing temperature, the CFT transitions into a state characterized by larger operator/state dimensions.

Given the identical Hilbert space of AdS to that of the CFT, we interpret our heated CFT as a thermal state in AdS. However, what constitutes this state? At lower temperatures, it comprises a thermal gas of light particles in AdS, predominantly confined to the central region. Yet, as temperature rises, more energy is confined to a relatively fixed-sized region. In the realm of dynamic gravity, this process is finite – at a critical temperature T_c, the hot gas collapses to form a black hole in AdS. This thought experiment illustrates that black holes in AdS correspond to a heated CFT.

7

Properties of AdS Black Holes

7.1 How anti-de Sitter black holes reach thermal equilibrium

In recent years, extensive research has focused on black holes within anti-de Sitter (AdS) spacetimes, driven by their significance in holography (gauge/gravity duality). These black holes exhibit distinct characteristics compared to their asymptotically flat counterparts. Notably, their event horizon isn't confined to a spherical shape; hyperbolic or toroidal horizons are also valid solutions to the Einstein field equations. Despite variations in horizon topology, AdS black holes display markedly different thermodynamic behaviors from asymptotically flat ones. The Hawking temperature in d-dimensions is given by the formula [1] (with units $G = c = \hbar = k_B = 1$)

$$T = \frac{k(d-3)L^2 + (d-1)r_h^2}{4\pi L^2 r_h}, \tag{7.1}$$

Here, $k = +1, 0, -1$ corresponds to horizons that are positively curved, flat, and negatively curved, respectively, while r_h represents the radial position of the event horizon. For sufficiently large black holes, where the horizon size exceeds the AdS curvature length scale ($r_h > L$), the temperature scales directly with r_h. In other words, large AdS black holes are "hot" [1]. This is in stark contrast to the asymptotically flat Schwarzschild black hole, whose temperature scales inversely with its mass (and therefore size).

Furthermore, asymptotically locally AdS spacetimes possess a timelike boundary at spatial infinity. Interestingly, null geodesics originating from within the bulk can intersect the boundary and return within a finite affine parameter interval (and also within a finite coordinate time t, if canonical Schwarzschild-like coordinates are utilized). To illustrate this phenomenon, let's consider the $k = 0$ scenario, commonly employed in holography. Henceforth, we will denote such black holes as "flat black holes".

Assuming the absence of a black hole, consider the metric tensor

$$ds^2 = -\frac{r^2}{L^2}dt^2 + \frac{L^2}{r^2}dr^2 + r^2\left(\sum_{i=1}^{d-2}(dx^i)^2\right), \tag{7.2}$$

The metric tensor straightforwardly depicts a flat representation of the maximally symmetric AdS spacetime. However, this coordinate system becomes inadequate at the center $r = 0$, hence we focus on $r = \varepsilon > 0$, where ε is small. The elapsed proper time between two events situated at $r = \varepsilon$ is $(\varepsilon/L)\Delta t$, where Δt denotes the time taken by a photon traveling from $r = \varepsilon$ to ∞ and back is

---

[1] Although the temperature of AdS black holes may appear exceedingly high in terms of global geometry, local observers do not perceive thermal radiation at such Hawking temperature. With this nuance in consideration, we will refrain from using quotation marks around the terms "hot" or "cold" henceforth.

$$\Delta t = 2\int_{\varepsilon}^{\infty} \frac{L^2}{r^2} dr = \frac{2L^2}{\varepsilon}. \tag{7.3}$$

This duration is finite, although large. The proper time experienced by the static observer amounts to $2L$. It's noteworthy that ε becomes irrelevant in the proper time calculation, consistent with the arbitrary nature of the AdS "center". Consequently, with a reflective boundary condition, Hawking photons are reflected back into the black hole, enabling a sufficiently large black hole to reach thermal equilibrium. (Another implication is the nonlinear instability of AdS: remarkably, a wide range of perturbations, regardless of their smallness, can be reflected and focused back in the bulk, potentially leading to black hole formation.) [2]

In the case of $k = 1$, even small black holes exhibit high temperatures ($T \sim 1/r_h$ according to Eq.(7.1)), akin to small asymptotically flat Schwarzschild black holes. Due to the time required for Hawking radiation to reach the boundary and reflect back, these small black holes can evaporate entirely before achieving thermal equilibrium. Put differently, while large black holes (with positive specific heat) are stable, small black holes (with negative specific heat) are inherently unstable. This stability criterion could theoretically define "large" and "small" black holes. While this criterion aligns with using either mass or horizon size greater than L to define black hole "size" in the $k = 1$ scenario, it's not applicable for the $k = 0$ case focused on in this study. For $k = 0$ black holes, regardless of size, the Hawking temperature is proportional to r_h, implying that small flat black holes are cold, i.e., they evaporate slowly. Consequently, small black holes have the potential to attain thermal equilibrium with their Hawking radiation. Thus, if we were to use stability/specific heat to define its "size", *all* $k = 0$ black holes would be considered "large". Hence, we use $r_h > L$ as the criterion to define a large black hole.

Moreover, since the boundary condition can be altered to a completely absorptive one, negating thermal equilibrium, we opt for a definition independent of boundary conditions. That is, a large black hole would retain its "largeness" regardless of boundary condition alterations. Given a fixed black hole in the bulk, there is a delay for radiation to reach the boundary and return. Until the radiation reaches the boundary (and potentially reflects back or is absorbed depending on the boundary condition), the black hole remains unaware of its potential to reach equilibrium. Therefore, a local criterion that defines black hole size at any given time, even *prior* to the emission of the first Hawking radiation (allowing us to discuss whether an *initially* "large" black hole can transition into a "small" one or remains "large", even in the $k = 1$ scenario), proves more practical. Defined in this manner, large flat black holes can dissipate into a small black hole in thermal equilibrium with their Hawking quanta[2].

7.2 Perturbations of anti-de Sitter black holes

Quasi-normal modes (QNMs) dictate the disturbances of a black hole, often determined by solving a wave equation for minor fluctuations in the background of the black hole, ensuring inward flux at the horizon and outward flux at infinity.

---

[2] Gibbons and Perry proposed that black holes can maintain thermal equilibrium with a heat bath despite particle interactions, although their study is limited to the asymptotically flat scenario, suggesting the conclusion's generality.

7.2.1 Perturbations

In this section, I examine scalar, gravitational, and electromagnetic perturbations of a d-dimensional AdS Schwarzschild black hole, analytically deriving the QNM spectrum in the high-frequency range. A discussion of low overtones will follow in the subsequent section. The metric describing an AdS Schwarzschild black hole is

$$ds^2 = -\left(\frac{r^2}{l^2} + K - \frac{2\mu}{r^{d-3}}\right) dt^2 + \frac{dr^2}{\frac{r^2}{l^2} + K - \frac{2\mu}{r^{d-3}}} + r^2 d\Sigma^2_{K,d-2} \tag{7.4}$$

I will select units such that the AdS radius $l = 1$. The radius of the horizon r_+ and the Hawking temperature T_H are then, respectively,

$$2\mu = r_+^{d-1}\left(1 + \frac{K}{r_+^2}\right), \quad T_H = \frac{(d-1)r_+^2 + K(d-3)}{4\pi r+} \tag{7.5}$$

The mass and entropy of the hole are, respectively,

$$M = (d-2)(K + r_+^2)\frac{r_+^{d-3}}{16\pi G} Vol(\Sigma_{K,d-2}), \quad S = \frac{r_+^{d-2}}{4G} Vol(\Sigma_{K,d-2}) \tag{7.6}$$

The parameter K dictates the curvature of the horizon and the boundary of AdS space. For $K = 0, +1, -1$, we encounter, respectively, a flat $(\mathbb{R}^{d-2})$, spherical $(\mathbb{S}^{d-2})$, and hyperbolic ($\mathbb{H}^{d-2}/\Gamma$, refers to a topological black hole with a hyperbolic horizon, where Γ denotes a discrete group of isometries.) horizon (boundary).

The harmonics on $\Sigma_{K,d-2}$ adhere to the equation,

$$(\nabla^2 + k^2)\mathbb{T} = 0 \tag{7.7}$$

When $K = 0$, k represents the momentum; whereas for $K = +1$, the eigenvalues are quantized.

$$k^2 = l(l + d - 3) - \delta \tag{7.8}$$

Conversely, for $K = -1$,

$$k^2 = \xi^2 + \left(\frac{d-3}{2}\right)^2 + \delta \tag{7.9}$$

where ξ is discretized for non-trivial Γ. $\delta = 0, 1, 2$ corresponds to scalar, vector, or tensor perturbations, respectively.

Scalar perturbations:

To determine the asymptotic behavior of QNMs, we must derive an approximation to the wave equation that holds in the high-frequency range. In three dimensions, this derived wave equation is exact (a hypergeometric equation). In five dimensions, I will transform the Heun equation into a hypergeometric equation, enabling the derivation of an analytical expression for the asymptotic form of QNM frequencies consistent with numerical findings.

***AdS_5*:** Focusing solely on the scenario of a large black hole, the massless scalar wave equation appears as follows:

$$\frac{1}{r^3}\partial_r(r^5 f(r)\partial_r\Phi) - \frac{1}{r^2 f(r)}\partial_t^2\Phi - \frac{1}{r^2}\vec{\nabla}^2\Phi = 0,\ \ f(r) = 1 - \frac{r_+^4}{r^4} \tag{7.10}$$

Expressing the solution as:

$$\Phi = e^{i(\omega t - \vec{p}\cdot\vec{x})}\Psi(y),\ \ y = \frac{r^2}{r_+^2} \tag{7.11}$$

The radial wave equation transforms into:

$$(y^2-1)(y(y^2-1)\Psi')' + \left(\frac{\omega^2}{4}y^2 - \frac{p^2}{4}(y^2-1)\right)\Psi = 0 \tag{7.12}$$

In seeking QNMs, we focus on the analytical solution that diminishes at the boundary and exhibits ingoing wave characteristics at the horizon. The wave equation introduces an extra (unphysical) singularity at $y = -1$, where the wavefunction follows $\Psi \sim (y+1)^{\pm\omega/4}$. Isolating the wavefunction's behavior near the singularities $y = \pm 1$,

$$\Psi(y) = (y-1)^{-i\omega/4}(y+1)^{\pm\omega/4}F_\pm(y) \tag{7.13}$$

$F_\pm(y)$ obeys the Heun equation

$$\begin{aligned} &y(y^2-1)F_\pm'' + \left[\left(3 - \frac{i\pm 1}{2}\omega\right)y^2 - \frac{i\pm 1}{2}\omega y - 1\right]F_\pm' \\ &+ \left[\frac{\omega}{2}\left(\pm\frac{i\omega}{4} \mp 1 - i\right)y - (i \mp 1)\frac{\omega}{4} - \frac{p^2}{4}\right]F_\pm = 0 \end{aligned} \tag{7.14}$$

The equation must be solved in a complex y-plane region where $|y| \geq 1$, covering the physical domain $r > r_+$. With large ω, the constant terms in the polynomial coefficients of F' and F become negligible, allowing an approximation of the wave equation by a hypergeometric equation.

$$(y^2-1)F''_\pm + \left[\left(3-\frac{i\pm1}{2}\omega\right)y - \frac{i\pm1}{2}\omega\right]F'_\pm + \frac{\omega}{2}\left(\pm\frac{i\omega}{4}\mp1-i\right)F_\pm = 0 \quad (7.15)$$

In the limit of large frequencies ω, the viable solution is

$$F_0(x) = F_1(a_+;a_-;c;(y+1)/2), \;\; a_\pm = 1-\frac{i\pm1}{4}\omega\pm1, \;\; c=\frac{3}{2}\pm\frac{\omega}{2} \quad (7.16)$$

To ensure proper behavior at the boundary ($y\to\infty$), we require F to be a polynomial, leading to the condition $a_+ = -n, \; n=1,2,\ldots$. This condition implies that F is a polynomial of order n, so as $y\to\infty$, $F\sim y^n\sim y^{-a_+}$ and $\Psi\sim y^{-i\omega/4}y^{\pm\omega/4}y^{-a_+}\sim y^{-2}$, as anticipated. Thus, we derive the quasi-normal frequencies as [3]

$$\hat{\omega} = \frac{\omega}{4\pi T_H} = 2n(\pm1-i) \quad (7.17)$$

Gravitational perturbations

I examine gravitational perturbations, focusing specifically on the scenario of spherical black holes ($K=+1$). I aim to obtain analytical expressions for QNMs [4], incorporating first-order corrections [5]. These findings closely align with numerical analysis results [6]. The generalization of alternative horizon geometries is straightforward. The radial wave equation governing gravitational perturbations within the black-hole background can be reformulated into a Schrödinger-like expression

$$-\frac{d^2\Psi}{dr_*^2} + V[r(r_*)]\Psi = \omega^2\Psi \quad (7.18)$$

Expressed in the tortoise coordinate, defined as $\frac{dr_*}{dr} = \frac{1}{f(r)}$, the potential V for different perturbation types has been determined by Ishibashi and Kodama [7]. For tensor, vector, and scalar perturbations, one derives, respectively:

$$V_T(r) = f(r)\left[\frac{l(l+d-3)}{r^2} + \frac{(d-2)(d-4)f(r)}{4r^2} + \frac{(d-2)f'(r)}{2r}\right] \tag{7.19}$$

$$V_v(r) = f(r)\left[\frac{l(l+d-3)}{r^2} + \frac{(d-2)(d-4)f(r)}{4r^2} + \frac{rf'''(r)}{2(d-3)}\right] \tag{7.20}$$

$$\begin{aligned}
V_s(r) = {} & \frac{f(r)}{4r^2}\left[l(l+d-3) - (d-2) + \frac{(d-1)(d-2)\mu}{r^{d-3}}\right]^{-2} \\
& \times \left\{ \frac{d(d-1)^2(d-2)^3\mu^2}{R^2 r^{2d-8}} - \frac{6(d-1)(d-2)^2(d-4)[l(l+d-3)-(d-2)]\mu}{R^2 r^{d-5}} \right. \\
& + \frac{(d-4)(d-6)[l(l+d-3)-(d-2)]^2 r^2}{R^2} + \frac{2(d-1)^2(d-2)^4\mu^3}{r^{3d-9}} \\
& + \frac{4(d-1)(d-2)(2d^2-11d+18)[l(l+d-3)-(d-2)]\mu^2}{r^{2d-6}} \\
& + \frac{(d-1)^2(d-2)^2(d-4)(d-6)\mu^2}{r^{2d-6}} \qquad (7.21) \\
& - \frac{6(d-2)(d-6)[l(l+d-3)-(d-2)^2]\mu}{r^{d-3}} \\
& - \frac{6(d-1)(d-2)^2(d-4)[l(l+d-3)-(d-2)]\mu}{r^{d-3}} \\
& \left. + 4[l(l+d-3)-(d-2)]^3 + d(d-2)[l(l+d-3)-(d-2)]^2 \right\} \qquad (7.22)
\end{aligned}$$

Near to the singularity of the black hole (when $r \sim 0$),

$$V_{\mathsf{T}} = -\frac{1}{4r_*^2} + \frac{\mathcal{A}_{\mathsf{T}}}{[-2(d-2)\mu]^{\frac{1}{d-2}}} r_*^{-\frac{d-1}{d-2}} + \dots , \quad \mathcal{A}_{\mathsf{T}} = \frac{(d-3)^2}{2(2d-5)} + \frac{\ell(\ell+d-3)}{d-2}, \tag{7.23}$$

$$V_{\mathsf{V}} = \frac{3}{4r_*^2} + \frac{\mathcal{A}_{\mathsf{V}}}{[-2(d-2)\mu]^{\frac{1}{d-2}}} r_*^{-\frac{d-1}{d-2}} + \dots \quad , \quad \mathcal{A}_{\mathsf{V}} = \frac{d^2-8d+13}{2(2d-15)} + \frac{\ell(\ell+d-3)}{d-2} \tag{7.24}$$

and

$$V_{\mathsf{S}} = -\frac{1}{4r_*^2} + \frac{\mathcal{A}_{\mathsf{S}}}{[-2(d-2)\mu]^{\frac{1}{d-2}}} r_*^{-\frac{d-1}{d-2}} + \dots , \tag{7.25}$$

where

$$\mathcal{A}_\mathsf{S} = \frac{(2d^3 - 24d^2 + 94d - 116)}{4(2d-5)(d-2)} + \frac{(d^2 - 7d + 14)[\ell(\ell + d - 3) - (d-2)]}{(d-1)(d-2)^2} \tag{7.26}$$

I have incorporated only the relevant terms for the desired order. The characteristics of the potential in the vicinity of the origin can be summarized as follows:

$$V = \frac{j^2 - 1}{4r_*^2} + \mathcal{A}\, r_*^{-\frac{d-1}{d-2}} + \dots \tag{7.27}$$

where $j = 0$ for scalar and tensor perturbations and for vector perturbations, $j = 2$. Conversely, in the vicinity of the boundary (for large r),

$$V = \frac{j_\infty^2 - 1}{4(r_* - \bar{r}_*)^2} + \dots \quad , \qquad \bar{r}_* = \int_0^\infty \frac{dr}{f(r)} \tag{7.28}$$

where $j_\infty = d-1$, $d-3$, and $d-5$ for tensor, vector, and scalar perturbations, respectively.

Upon rescaling the tortoise coordinate ($z = \omega r_*$), the Schrödinger-like wave equation to first order takes the form

$$\left(\mathcal{H}_0 + \omega^{-\frac{d-3}{d-2}}\, \mathcal{H}_1\right) \Psi = 0, \tag{7.29}$$

where

$$\mathcal{H}_0 = \frac{d^2}{dz^2} - \left[\frac{j^2 - 1}{4z^2} - 1\right] \quad , \quad \mathcal{H}_1 = -\mathcal{A}\, z^{-\frac{d-1}{d-2}}. \tag{7.30}$$

One can expand the wave function by considering $\mathcal{H}_1$ as a perturbation,

$$\Psi(z) = \Psi_0(z) + \omega^{-\frac{d-3}{d-2}}\, \Psi_1(z) + \dots \tag{7.31}$$

and solve the wave equation through perturbation.

The wave equation at zeroth order,

$$\mathcal{H}_0\Psi_0(z) = 0, \tag{7.32}$$

can be resolved using Bessel functions,

$$\Psi_0(z) = A_1\sqrt{z}\,J_{\frac{j}{2}}(z) + A_2\sqrt{z}\,N_{\frac{j}{2}}(z). \tag{7.33}$$

For large values B.1 of z, its behavior is similar to

$$\begin{aligned}\Psi_0(z) \quad &\sim \quad \sqrt{\frac{2}{\pi}}\left[A_1\cos(z-\alpha_+) + A_2\sin(z-\alpha_+)\right] && (7.34)\\ &= \quad \frac{1}{\sqrt{2\pi}}(A_1 - iA_2)e^{-i\alpha_+}e^{iz} + \frac{1}{\sqrt{2\pi}}(A_1 + iA_2)e^{+i\alpha_+}e^{-iz} && (7.35)\end{aligned}$$

where $\alpha_\pm = \frac{\pi}{4}(1 \pm j)$.

At the boundary ($r \to \infty$), the wavefunction must vanish, thus the permissible solution is

$$\Psi_0(r_*) = B\sqrt{\omega(r_* - \bar{r}_*)}\;J_{\frac{j_\infty}{2}}(\omega(r_* - \bar{r}_*)) \tag{7.36}$$

Certainly, $\Psi \to 0$ as $r_* \to \bar{r}_*$, as expected. As z becomes large, it behaves as

$$\Psi(r_*) \sim \sqrt{\frac{2}{\pi}}\,B\cos\left[\omega(r_* - \bar{r}_*) + \beta\right]\;, \qquad \beta = \frac{\pi}{4}(1 + j_\infty) \tag{7.37}$$

This needs to align with the asymptotic expression of the wavefunction near the black hole singularity along the Stokes line $\Im z = \Im(\omega r_*) = 0$. Consequently, it imposes a restriction on the coefficients A_1 and A_2,

$$A_1 \tan(\omega \bar{r}_* - \beta - \alpha_+) - A_2 = 0. \tag{7.38}$$

By applying the boundary condition at the horizon

$$\Psi(z) \sim e^{iz} \quad , \qquad z \to -\infty \ , \tag{7.39}$$

Applying the boundary condition at the horizon yields an additional constraint. To determine it, one must analytically extend the wavefunction near the black hole singularity ($z = 0$) to negative values of z. A rotation of z by $-\pi$ corresponds to a rotation by $-\frac{\pi}{d-2}$ near the origin in the complex r-plane. Using the known form of Bessel functions

$$J_\nu(e^{-i\pi} z) = e^{-i\pi\nu} J_\nu(z) \ , \qquad N_\nu(e^{-i\pi} z) = e^{i\pi\nu} N_\nu(z) - 2i \cos \pi\nu \, J_\nu(z) \tag{7.40}$$

For $z < 0$, the wavefunction transforms into

$$\Psi_0(z) = e^{-i\pi(j+1)/2} \sqrt{-z} \left\{ \left[A_1 - i(1 + e^{i\pi j}) A_2 \right] \, J_{\frac{j}{2}}(-z) + A_2 e^{i\pi j} \, N_{\frac{j}{2}}(-z) \right\} \tag{7.41}$$

whose large z behavior is expressed as

$$\Psi \sim \frac{e^{-i\pi(j+1)/2}}{\sqrt{2\pi}} \left[A_1 - i(1 + 2e^{j\pi i}) A_2 \right] \, e^{-iz} + \frac{e^{-i\pi(j+1)/2}}{\sqrt{2\pi}} \left[A_1 - i A_2 \right] e^{iz} \tag{7.42}$$

As a result, another constraint emerges

$$A_1 - i(1 + 2e^{j\pi i}) A_2 = 0 \tag{7.43}$$

The two limitations are in agreement as long as

$$\begin{vmatrix} 1 & -i(1+2e^{j\pi i}) \\ \tan(\omega\bar{r}_* - \beta - \alpha_+) & -1 \end{vmatrix} = 0 \tag{7.44}$$

which gives quasi-normal modes [4]

$$\omega\bar{r}_* = \frac{\pi}{4}(2+j+j_\infty) - \tan^{-1}\frac{i}{1+2e^{j\pi i}} + n\pi \tag{7.45}$$

The first-order perturbation to the aforementioned asymptotic expression can be determined using conventional perturbation theory [5]. To first order, the wave equation becomes

$$\mathcal{H}_0\Psi_1 + \mathcal{H}_1\Psi_0 = 0 \tag{7.46}$$

The solution is

$$\begin{aligned}\Psi_1(z) = \sqrt{z}\,N_{\frac{j}{2}}(z)\int_0^z dz'\frac{\sqrt{z'}\,J_{\frac{j}{2}}(z')\mathcal{H}_1\Psi_0(z')}{\mathcal{W}} \\ -\sqrt{z}\,J_{\frac{j}{2}}(z)\int_0^z dz'\frac{\sqrt{z'}\,N_{\frac{j}{2}}(z')\mathcal{H}_1\Psi_0(z')}{\mathcal{W}}\end{aligned} \tag{7.47}$$

where $\mathcal{W} = 2/\pi$ is the Wronskian.

The wave function at the first order is described as

$$\Psi(z) = \{A_1[1-b(z)] - A_2a_2(z)\}\sqrt{z}J_{\frac{j}{2}}(z) + \{A_2[1+b(z)] + A_1a_1(z)\}\sqrt{z}N_{\frac{j}{2}}(z) \tag{7.48}$$

where

$$\begin{aligned} a_1(z) &= \frac{\pi\mathcal{A}}{2}\,\omega^{-\frac{d-3}{d-2}} \int_0^z dz'\; z'^{-\frac{1}{d-2}} J_{\frac{j}{2}}(z') J_{\frac{j}{2}}(z') \\ a_2(z) &= \frac{\pi\mathcal{A}}{2}\,\omega^{-\frac{d-3}{d-2}} \int_0^z dz'\; z'^{-\frac{1}{d-2}} N_{\frac{j}{2}}(z') N_{\frac{j}{2}}(z') \\ b(z) &= \frac{\pi\mathcal{A}}{2}\,\omega^{-\frac{d-3}{d-2}} \int_0^z dz'\; z'^{-\frac{1}{d-2}} J_{\frac{j}{2}}(z') N_{\frac{j}{2}}(z') \end{aligned}$$

and $\mathcal{A}$ varies based on the nature of the perturbation. In the asymptotic limit, it demonstrates behavior similar to

$$\Psi(z) \sim \sqrt{\frac{2}{\pi}}\left[A_1' \cos(z-\alpha_+) + A_2' \sin(z-\alpha_+)\right] , \tag{7.49}$$

where

$$A_1' = [1-\bar{b}]A_1 - \bar{a}_2 A_2 \quad , \qquad A_2' = [1+\bar{b}]A_2 + \bar{a}_1 A_1 \tag{7.50}$$

and I established the notation

$$\bar{a}_1 = a_1(\infty) \quad , \qquad \bar{a}_2 = a_2(\infty) \quad , \qquad \bar{b} = b(\infty) \tag{7.51}$$

The first constraint is adjusted to

$$A_1' \tan(\omega\bar{r}_* - \beta - \alpha_+) - A_2' = 0 \tag{7.52}$$

Explicitly,

$$[(1-\bar{b})\tan(\omega\bar{r}_* - \beta - \alpha_+) - \bar{a}_1]A_1 - [1+\bar{b}+\bar{a}_2\tan(\omega\bar{r}_* - \beta - \alpha_+)]A_2 = 0 \tag{7.53}$$

To determine the second constraint at the first order, one must approach the horizon, involving a rotation of $-\pi$ in the z plane. Using

$$\begin{aligned}
a_1(e^{-i\pi}z) &= e^{-i\pi\frac{d-3}{d-2}}e^{-i\pi j}a_1(z)\ ,\\
a_2(e^{-i\pi}z) &= e^{-i\pi\frac{d-3}{d-2}}\left[e^{i\pi j}a_2(z)-4\cos^2\frac{\pi j}{2}a_1(z)-2i(1+e^{i\pi j})b(z)\right]\ ,\\
b(e^{-i\pi}z) &= e^{-i\pi\frac{d-3}{d-2}}\left[b(z)-i(1+e^{-i\pi j})a_1(z)\right]
\end{aligned}$$

in the limit $z\to-\infty$ we get,

$$\Psi(z)\sim -ie^{-ij\pi/2}B_1\cos(-z-\alpha_+)-ie^{ij\pi/2}B_2\sin(-z-\alpha_+) \qquad (7.54)$$

where

$$\begin{aligned}
B_1 &= A_1-A_1e^{-i\pi\frac{d-3}{d-2}}[\bar{b}-i(1+e^{-i\pi j})\bar{a}_1]\\
&\quad -A_2e^{-i\pi\frac{d-3}{d-2}}\left[e^{+i\pi j}\bar{a}_2-4\cos^2\frac{\pi j}{2}\bar{a}_1-2i(1+e^{+i\pi j})\bar{b}\right]\\
&\quad -i(1+e^{i\pi j})\left[A_2+A_2e^{-i\pi\frac{d-3}{d-2}}[\bar{b}-i(1+e^{-i\pi j})\bar{a}_1]+A_1e^{-i\pi\frac{d-3}{d-2}}e^{-i\pi j}\bar{a}_1\right]\\
B_2 &= A_2+A_2e^{-i\pi\frac{d-3}{d-2}}[\bar{b}-i(1+e^{-i\pi j})\bar{a}_1]+A_1e^{-i\pi\frac{d-3}{d-2}}e^{-i\pi j}\bar{a}_1
\end{aligned}$$

Hence, the second constraint in the first order is formulated as

$$[1-e^{-i\pi\frac{d-3}{d-2}}(i\bar{a}_1+\bar{b})]A_1-[i(1+2e^{i\pi j})+e^{-i\pi\frac{d-3}{d-2}}((1+e^{i\pi j})\bar{a}_1+e^{i\pi j}\bar{a}_2-i\bar{b})]A_2=0 \qquad (7.55)$$

Agreement between the two primary level constraints results in

$$\begin{vmatrix} 1+\bar{b}+\bar{a}_2\tan(\omega\bar{r}_*-\beta-\alpha_+) & \begin{array}{c} i(1+2e^{i\pi j}) \\ +e^{-i\pi\frac{d-3}{d-2}}((1+e^{i\pi j})\bar{a}_1+e^{i\pi j}\bar{a}_2-i\bar{b}) \end{array} \\ (1-\bar{b})\tan(\omega\bar{r}_*-\beta-\alpha_+)-\bar{a}_1 & 1-e^{-i\pi\frac{d-3}{d-2}}(i\bar{a}_1+\bar{b}) \end{vmatrix} = 0 \tag{7.56}$$

resulting in the quasi-normal frequencies' first-order expression,

$$\begin{aligned} \omega\bar{r}_* &= \frac{\pi}{4}(2+j+j_\infty)+\frac{1}{2i}\ln 2+n\pi \\ &\quad -\frac{1}{8}\left\{6i\bar{b}-2ie^{-i\pi\frac{d-3}{d-2}}\bar{b}-9\bar{a}_1+e^{-i\pi\frac{d-3}{d-2}}\bar{a}_1+\bar{a}_2-e^{-i\pi\frac{d-3}{d-2}}\bar{a}_2\right\} \end{aligned}$$

where (see appendix B.2)

$$\begin{aligned} \bar{a}_1 &= \frac{\pi\mathcal{A}}{4}\left(\frac{n\pi}{2\bar{r}_*}\right)^{-\frac{d-3}{d-2}}\frac{\Gamma(\frac{1}{d-2})\Gamma(\frac{j}{2}+\frac{d-3}{2(d-2)})}{\Gamma^2(\frac{d-1}{2(d-2)})\Gamma(\frac{j}{2}+\frac{d-1}{2(d-2)})} \\ \bar{a}_2 &= \left[1+2\cot\frac{\pi(d-3)}{2(d-2)}\cot\frac{\pi}{2}\left(-j+\frac{d-3}{d-2}\right)\right]\bar{a}_1 \\ \bar{b} &= -\cot\frac{\pi(d-3)}{2(d-2)}\,\bar{a}_1 \end{aligned}$$

Therefore, the correction to the first order is approximate of order $\mathcal{O}(n^{-\frac{d-3}{d-2}})$.

These analytical findings align well with numerical outcomes [6] for a thorough comparison [5].

Electromagnetic perturbations:

The electromagnetic potential within a four-dimensional context is

$$V_{\mathsf{EM}} = \frac{\ell(\ell+1)}{r^2} f(r). \tag{7.57}$$

In proximity to the origin,

$$V_{\mathsf{EM}} = \frac{j^2-1}{4r_*^2} + \frac{\ell(\ell+1) r_*^{-3/2}}{2\sqrt{-4\mu}} + \dots\ , \tag{7.58}$$

where $j = 1$, this results in a potential that diminishes to zeroth order. To derive the QNM spectrum, it is necessary to incorporate first-order adjustments from the beginning. By following a similar approach to gravitational perturbations, the QNMs are derived

$$\omega \bar{r}_* = n\pi - \frac{i}{4} \ln n + \frac{1}{2i} \ln\left(2(1+i)\mathcal{A}\sqrt{\bar{r}_*}\right)\ , \qquad \mathcal{A} = \frac{\ell(\ell+1)}{2\sqrt{-4\mu}} \tag{7.59}$$

It's notable that the first-order adjustment exhibits a logarithmic behavior with respect to n, a characteristic that could be linked to gauge invariance.

Similar to the case of gravitational perturbations, the aforementioned analytical findings align well with numerical results for a thorough comparison [6]. (see ref. [5] for detailed comparison)

8

A detailed study of quasinormal frequencies of Kerr black hole

8.1 Introduction

The gravitational waves released by perturbed black holes are widely recognized to be chiefly governed, in the late stages, by quasi-normal modes. These modes are distinguished by complex frequencies featuring positive imaginary components, signifying damped oscillations. The quasi-normal frequencies of black holes within asymptotically flat spacetime hold significant astrophysical relevance. They furnish insights into key parameters of a black hole, including its mass and angular momentum. This is why they have been thoroughly investigated for over four decades.

Regge and Wheeler [8] pioneered the investigation into this subject by initially exploring linear perturbations of stationary black holes. They formulated a second-order ordinary differential equation that characterizes perturbations of scalar, electromagnetic, and gravitational fields around Schwarzschild black holes. Teukolsky [9] later addressed the challenge of separating the wave equation for rotating Kerr black holes, successfully deriving two distinct partial differential equations governing the radial and angular components of the perturbation. For an in-depth exploration of black hole perturbation, readers can refer to [10].

The discovery of quasinormal modes originated from numerical simulations of gravitational wave evolution around black holes, initially identified by Vishveshwara [11] and Press [12]. Chandrasekhar and Detweiler [13] introduced the first numerical method for computing these modes, relying on direct integration of the Regge-Wheeler equation. Various analytical approaches have also been attempted to derive these frequencies, with applications extending to Kerr and Reissner-Nordstrom black holes. However, these methods often yield less precise frequency values and struggle to handle rapidly damped modes.

Leaver [14] demonstrated that the quasinormal frequencies of both stationary and rotating black holes can be obtained using a continued fraction technique. While several methods exist for computing quasinormal frequencies for stationary black holes, the continued fraction method remains the only one adaptable to the Kerr scenario. In the Kerr case, besides determining the quasinormal frequencies, one must also evaluate the separation constants, which are the angular eigenvalues linked to the Teukolsky equations. An enhanced version of Leaver's findings is presented in [15].

In perturbing rotating black holes, the computation of angular eigenvalues concurrently poses significant challenges in achieving accurate frequency outcomes. As an alternative to Leaver's method, Sasaki [16] proposed employing ordinary perturbation theory to tackle the angular equation. However, this approach is limited to scenarios where the expansion parameter $a\omega$ remains small. In essence, for non-zero values of a, this technique fails to handle high frequencies.

In this section, I adopt Leaver's continued fraction technique. Following the acquisition of analytical solutions for the radial and angular equations, I simultaneously solve the corresponding pair of continued fraction equations, akin to Leaver's approach. My subsequent strategy involves initially computing the angular eigenvalues using a Pade approximation of the actual values, and subsequently integrating this approximation into the radial solution. I then contrast these two outcomes and discuss which approach proves more efficient.

8.1.1 Rotating Black Holes

Spacetime Symmetries:

Definition 8.1.1. A spacetime is considered asymptotically flat if and only if it is stationary, characterized by the existence of a Killing vector field, k, which is timelike near infinity (where it can be normalized such that $k^2 \to -1$). Outside a potential horizon, $k = \partial/\partial t$, where t represents a time coordinate. Consequently, the general metric for a stationary spacetime in these coordinates is expressed as:

$$ds^2 = g_{00}(\vec{x})dt^2 + 2g_{0i}(\vec{x})dtdx^i + g_{ij}(\vec{x})dx^i dx^j \tag{8.1}$$

A stationary spacetime can be deemed static, at least in the vicinity of infinity, if it also exhibits invariance under time-reversal. This condition necessitates $g_{0i} = 0$, leading to the general static metric formulation:

$$ds^2 = g_{00}(\vec{x})dt^2 + g_{ij}(\vec{x})dx^i dx^j \tag{8.2}$$

Definition 8.1.2. An asymptotically flat spacetime demonstrates axisymmetry when a spacelike Killing vector field m (termed as an 'axial' Killing vector field) exists near infinity, and all its orbits are closed. By selecting appropriate coordinates, we can express m as:

$$m = \frac{\partial}{\partial \phi} \tag{8.3}$$

8.1.2 Kerr metric

The Kerr metric, also known as Kerr geometry, characterizes the geometry of vacuum spacetime surrounding a rotating, uncharged, axially symmetric black hole with a nearly spherical event horizon. It serves as an exact solution to the Einstein field equations of general relativity, which are notably non-linear, posing challenges in finding precise solutions.

Describing the spacetime geometry near a mass M with angular momentum J, the Kerr metric delineates the relationships. The metric, expressed in

Boyer–Lindquist coordinates, takes the form of the line element for proper time,

$$\begin{aligned} ds^2 &= -c^2 d\tau^2 \qquad (8.4) \\ &= -\left(1 - \frac{2Mr}{\Sigma}\right) dt^2 + \frac{4Mra\sin^2\theta}{\Sigma} dt d\phi - \frac{\Sigma}{\Delta} dr^2 - \Sigma d\theta^2 \\ &\quad - \left(r^2 + a^2 + \frac{2Mra^2\sin^2\theta}{\Sigma}\right)\sin^2\theta d\phi^2 \qquad (8.5) \end{aligned}$$

Here, $\Delta = r^2 - 2Mr - a^2$ with $a = J/M$, and $\Sigma = r^2 + a^2\cos^2\theta$. A noteworthy aspect of the provided metric is the presence of the cross-term $dt\, d\phi$. This indicates a coupling between time and motion in the rotational plane, a coupling that diminishes when the black hole's angular momentum approaches zero.

Important surfaces

Within the Kerr metric (8.5), numerous significant surfaces emerge. The inner surface corresponds to an event horizon akin to that found in the Schwarzschild metric, manifesting where the purely radial component g_{rr} of the metric diverges. Resolving the quadratic equation $1/g_{rr} = 0$ produces the solution:

$$r_{\pm}^{H} = M \pm \sqrt{M^2 - a^2} \qquad (8.6)$$

In contrast to the Schwarzschild metric, where the event horizon coincides with the location where the purely temporal component g_{tt} of the metric transitions from positive to negative, in the Kerr metric, this occurrence transpires at a distinct distance. Once more, resolving a quadratic equation $g_{tt} = 0$ furnishes the solution:

$$r_{\pm}^{E} = M \pm \sqrt{M^2 - a^2\cos^2\theta} \qquad (8.7)$$

Because of the presence of the $\cos^2\theta$ term in the square root, this external surface takes on the appearance of a flattened sphere that intersects with the inner surface at the poles of the rotational axis, where the colatitude θ is either 0 or π. The region between these two surfaces is referred to as the ergosphere. Within this region, the purely temporal component g_{tt} becomes negative, essentially behaving like a purely spatial metric component. Therefore, particles within this ergosphere must rotate along with the central mass in order to maintain their time-like properties.

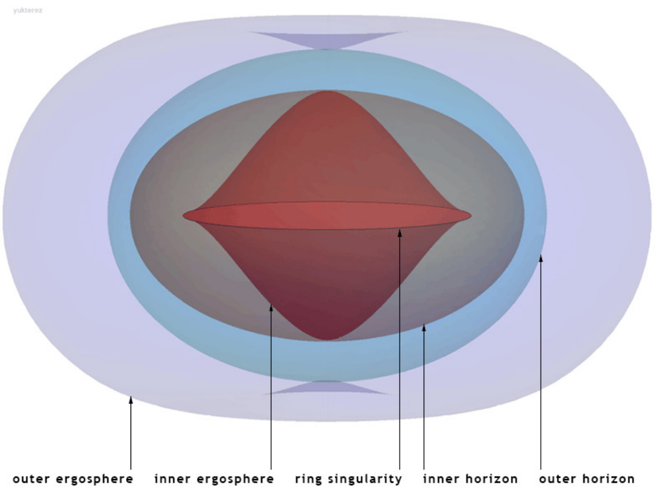

Figure 8.1: Location of the horizons, ergospheres, and the ring singularity of the Kerr spacetime in Cartesian Kerr–Schild coordinates.

Credit: By Yukterez (Simon Tyran, Vienna) - Own work, CC BY-SA 4.0, *https://commons.wikimedia.org/w/index.php?curid=60362250*

Ring singularity

In classical physics, under general relativity, when a spherical non-rotating object reaches a critical radius and collapses due to its own gravitational force, theory predicts that it will condense into a 0-dimensional point. However, this scenario differs when considering a rotating black hole, specifically a Kerr black hole. In the case of a rotating body such as a fluid, its mass distribution deviates from spherical symmetry, exhibiting an equatorial bulge, and possesses angular momentum. Classical physics dictates that a point cannot sustain rotation or angular momentum. Therefore, in general relativity, which is a classical theory, the smallest form of singularity capable of supporting these properties is a 2-dimensional ring with negligible thickness but a non-zero radius. This peculiar structure is commonly known as a ringularity or Kerr singularity.

8.2 Angular and radial continued fractions equations

Teukolsky [9] introduced a master perturbation equation encompassing scalar, electromagnetic, and gravitational perturbations of this metric. Assuming a temporal and azimuthal dependence represented by $e^{-i\omega t+im\phi}$, Teukolsky separated the field quantities denoted by ψ and decomposed the wave equation as follows:

$$\psi(t,r,\theta,\phi)=\frac{1}{2\pi}\int e^{-\mathrm{i}\omega t}\sum_{l=|s|}^{\infty}\sum_{m=-l}^{+l}e^{\mathrm{i}m\phi}S_s(\theta)R_s(r)d\omega \tag{8.8}$$

The decomposed differential equation governing the angular component of the perturbation is

$$(1-u^2)\frac{d^2S_s}{du^2}-2u\frac{dS_s}{du}+W(u)S_s=0, \tag{8.9}$$

where

$$W=a^2\omega^2u^2-2a\omega su+\lambda+s-\frac{(m+su)^2}{1-u^2}, \tag{8.10}$$

and the corresponding equation for the radial component is

$$\Delta\frac{d^2R_s}{dr^2}+2(s+1)(r-M)\frac{dR_s}{dr}+V(r)R_s=0, \tag{8.11}$$

where

$$V = \frac{K^2 - 2isK(r-M)}{\Delta} + 4is\omega r - \lambda + 2a\omega m - a^2\omega^2, \tag{8.12}$$

with

$$\begin{aligned} u &= \cos\theta, && (8.13) \\ K &= (r^2 + a^2)\omega - am. && (8.14) \end{aligned}$$

The spin-weight parameter s corresponds to the values 0, -1, and -2 for outgoing scalar, electromagnetic, and gravitational fields, respectively. In equation (8.10), λ represents the angular separation constant, which simplifies to $l(l+1) - s(s+1)$ in the Schwarzschild limit.

For rotating black holes, numerical solutions for eq. (8.9) are necessary, following the approach outlined by Leaver [14]. Boundary conditions stipulate that S_s remains regular at the regular singular points $u = \pm 1$. The corresponding indices are determined by $\pm(m+s)/2$ at $u = 1$ and $\pm(m-s)/2$ at $u = -1$. A solution to equation (8.9) can be expressed as

$$S_s(u) = e^{a\omega u}(1+u)^{|m-s|/2}(1-u)^{|m+s|/2}\sum_{n=0}^{\infty}\hat{a}_n(1+u)^n. \tag{8.15}$$

The coefficients of the series are interconnected through a three-term recurrence relationship, and the boundary condition at $u = 1$ is solely met by its minimal solution sequence. This recurrence relation is characterized by,

$$\hat{\alpha}_0\hat{a}_1 + \hat{\beta}_0\hat{a}_0 = 0, \tag{8.16}$$

$$\hat{\alpha}_n \hat{a}_{n+1} + \hat{\beta}_n \hat{a}_n + \hat{\gamma}_n \hat{a}_{n-1} = 0 \ \ (n \geq 1), \tag{8.17}$$

where $k_1 = |m - s|/2$, $k_2 = |m + s|/2$, and the coefficients governing the recurrence relation are

$$\begin{aligned}
\hat{\alpha}_n &= -2(n+1)(n+2k_1+1), && (8.18)\\
\hat{\beta}_n &= n(n-1) + 2n(k_1+k_2+1-2a\omega) - 2a\omega(2k_1+s+1) && \\
&\quad +(k_1+k_2)(k_1+k_2+1) - (a^2\omega^2 + s(s+1) + \lambda), && (8.19)\\
\hat{\gamma}_n &= 2a\omega(n+k_1+k_2+s). && (8.20)
\end{aligned}$$

The infinite continued fraction expresses the ratio between successive $\hat{a}_n$ as follows:

$$\frac{\hat{a}_{n+1}}{\hat{a}_n} = \frac{-\hat{\gamma}_{n+1}}{\hat{\beta}_{n+1} - \frac{\hat{\alpha}_{n+1}\hat{\gamma}_{n+2}}{\hat{\beta}_{n+2} - \frac{\hat{\alpha}_{n+2}\hat{\gamma}_{n+3}}{\hat{\beta}_{n+3} - \cdots}}} \tag{8.21}$$

In usual notation, we can write,

$$\frac{\hat{a}_{n+1}}{\hat{a}_n} = \frac{-\hat{\gamma}_{n+1}}{\hat{\beta}_{n+1}-} \frac{\hat{\alpha}_{n+1}\hat{\gamma}_{n+2}}{\hat{\beta}_{n+2}-} \frac{\hat{\alpha}_{n+2}\hat{\gamma}_{n+3}}{\hat{\beta}_{n+3}-} \cdots \tag{8.22}$$

Eq. (8.22) serves as a boundary condition at $n = \infty$ for the sequence $\hat{a}_n$. By evaluating (8.22) at $n = 0$ and utilizing equation (8.16) as a boundary condition at $n = 0$ for the ratio $\hat{a}_1/\hat{a}_0$, we derive a characteristic equation for the quasi-normal frequencies. In essence, two expressions must be simultaneously fulfilled:

From eq.(8.16) we get,

$$\frac{\hat{a}_1}{\hat{a}_0} = -\frac{\hat{\beta}_0}{\hat{\alpha}_0} \tag{8.23}$$

From eq. (8.17) we get,

$$\frac{\hat{a}_1}{\hat{a}_0} = -\frac{-\hat{\gamma}_1}{\hat{\beta}_1 -}\frac{\hat{\alpha}_1\hat{\gamma}_2}{\hat{\beta}_2 -}\frac{\hat{\alpha}_2\hat{\gamma}_3}{\hat{\beta}_3 -}\cdots \tag{8.24}$$

It's worth noting that in the Schwarzschild limit ($\hat{a} = 0$), the coefficients $\hat{\gamma}_n$ are zero for all n, and the recursion process halts whenever λ reaches a value such that $\hat{\beta}_n$ becomes zero for some n. This scenario occurs when $\lambda = n(n+1) - s(s+1)$, meaning $n = l$.

The solution will be deemed minimal if the angular separation constant λ corresponds to a root of the continued fraction equation.

$$0 = \hat{\beta}_0 - \frac{\hat{\alpha}_0\hat{\gamma}_1}{\hat{\beta}_1 -}\frac{\hat{\alpha}_1\hat{\gamma}_2}{\hat{\beta}_2 -}\frac{\hat{\alpha}_2\hat{\gamma}_3}{\hat{\beta}_3 -}\frac{\hat{\alpha}_3\hat{\gamma}_4}{\hat{\beta}_4 -}\cdots . \tag{8.25}$$

Similarly to the approach taken for eq. (8.9), a solution to the radial eq. (8.11) is obtained. This equation exhibits two regular singular points, r_+ and r_-, corresponding to the roots of Δ. Introducing a new rotational parameter $b = (1 - a^2/M^2)^{\frac{1}{2}}$, where b ranges from 1 to 0 as a varies from 0 to M (the Kerr limit), we redefine $\hat{a} = a/2M$ and $\hat{\omega} = 2M\omega$. The event horizon is situated at $r = r_+$. The indices at $r = r_+$ are $i\sigma_+$ and $-s - i\sigma_+$, where $\sigma_+ = (\omega r_+ - \hat{a}m)/b$. Given that the second index corresponds to in-going radiation, we can impose the quasinormal boundary conditions on R_s

$$R_s \sim (r - r_+)^{-s-i\sigma_+}, \; as \; r \to r_+ \tag{8.26}$$

$$R_s \sim r^{-1-2s+i\omega}e^{i\omega r}, \; as \; r \to \infty \tag{8.27}$$

Thus, our solution can be written as

$$R_s = e^{i\omega r}(r-r_-)^{-1-s+i\hat{\omega}+i\sigma_+}(r-r_+)^{-s-i\sigma_+}\sum_{n=0}^{\infty} a_n \left(\frac{r-r_+}{r-r_-}\right)^n , \tag{8.28}$$

The expansion coefficients are once more determined by a three-term recurrence relation,

$$\alpha_0 a_1 + \beta_0 a_0 = 0 \tag{8.29}$$

$$\alpha_n a_{n+1} + \beta_n a_n + \gamma_n a_{n-1} = 0 \ \ (n \geq 1) \tag{8.30}$$

The recursion coefficients are

$$\begin{aligned}
\alpha_n &= n^2 + (c_0+1)n + c_0, \\
\beta_n &= -2n^2 + (c_1+2)n + c_3, \\
\gamma_n &= n^2 + (c_2-3)n + c_4 - c_2 + 2,
\end{aligned} \tag{8.31}$$

and the intermediary constants are determined by

$$\begin{aligned}
c_0 &= 1 - s - i\hat{\omega} - \frac{2i}{b}\left(\frac{\hat{\omega}}{2} - \hat{a}m\right), \\
c_1 &= -4 + 2i\hat{\omega}(2+b) + \frac{4i}{b}\left(\frac{\hat{\omega}}{2} - \hat{a}m\right), \\
c_2 &= s + 3 - 3i\hat{\omega} - \frac{2i}{b}\left(\frac{\hat{\omega}}{2} - \hat{a}m\right), \\
c_3 &= \hat{\omega}^2(4 + 2b - \hat{a}^2) - 2\hat{a}m\hat{\omega} - s - 1 + (2+b)i\hat{\omega} - \lambda + \frac{4\hat{\omega}+2i}{b}\left(\frac{\hat{\omega}}{2} - \hat{a}m\right), \\
c_4 &= s + 1 - 2\hat{\omega}^2 - (2s+3)i\hat{\omega} - \frac{4\hat{\omega}+2i}{b}\left(\frac{\hat{\omega}}{2} - \hat{a}m\right),
\end{aligned} \tag{8.32}$$

The radial series solution converges, and the boundary condition at $r = \infty$ is fulfilled if, for a specified set of a, m, λ, and s, the frequency ω corresponds to a root of the continued fraction equation.

$$0 = \beta_0 - \frac{\alpha_0\gamma_1}{\beta_1 -}\frac{\alpha_1\gamma_2}{\beta_2 -}\frac{\alpha_2\gamma_3}{\beta_3 -}\cdots, \tag{8.33}$$

8.2.1 New technique for the angular equation

For small $a\omega$, the angular separation constant can be estimated using perturbation theory. This approach, as demonstrated by Sasaki in [16], involves expanding the angular eigenvalues in terms of powers of $a\omega$.

$$\lambda = \lambda_0 + a\omega\lambda_1 + a^2\omega^2\lambda_2 + O((a\omega)^3). \tag{8.34}$$

and the values of the coefficients are

$$\begin{aligned}
\lambda_0 &= l(l+1) - 2 = (l-1)(l+2), \\
\lambda_1 &= -2m\frac{l(l+1)+4}{l(l+1)}, \\
\lambda_2 &= -2(l+1)(c_{lm}^{l+1})^2 + 2l(c_{lm}^{l-1})^2 + \frac{2}{3} - \frac{2}{3}\frac{(l+4)(l-3)(l^2+l-3m^2)}{l(l+1)(2l+3)(2l-1)},
\end{aligned}$$

with

$$\begin{aligned}
c_{lm}^{l+1} &= \frac{2}{(l+1)^2}\left[\frac{(l+3)(l-1)(l+m+1)(l-m+1)}{(2l+1)(2l+3)}\right]^{1/2}, \\
c_{lm}^{l-1} &= -\frac{2}{l^2}\left[\frac{(l+2)(l-2)(l+m)(l-m)}{(2l+1)(2l-1)}\right]^{1/2}.
\end{aligned}$$

This approach is effective when the expansion parameter $a\omega$ remains sufficiently small, thus avoiding limitations associated with handling high frequencies. Since our interest extends to both slowly and rapidly damped modes, we aim to circumvent such restrictions.

As outlined in the introduction, I adhere to Leaver's continued fraction method and propose a novel strategy for numerically solving the two continued fraction equations (8.25) and (8.33). Instead of employing a two-dimensional root-finding routine, which simultaneously determines frequencies and separation constants in the complex plane, I opt to compute the angular eigenvalues first. Subsequently, I utilize these values in the continued fraction arising from the radial solution.

Initially, I developed a computer program capable of efficiently approximating the continued fraction (8.25) and computing the corresponding roots, which represent the angular eigenvalues. For this purpose, we employ the highly effective "modified Lent's algorithm" [17], which essentially transforms the continued fraction into a quotient of two series

$$f_n = \frac{A_n}{B_n}, \tag{8.35}$$

The coefficients A_n and B_n are obtained through recurrence relations associated with the coefficients of the continued fraction. The series are computed from left to right, and the algorithm terminates once the absolute difference between two consecutive fractions falls below a predetermined threshold. Subsequently, within the same program, the roots are determined using a complex one-dimensional Newton-Rapson method routine.

Following this, I fit the numerical data for λ to a Padé approximation for real

$a\omega$, which is expressed as,

$$\lambda = \frac{a_0 + a_1 a\omega + a_2(a\omega)^2 + a_3(a\omega)^3 + a_4(a\omega)^4}{1 + b_1 a\omega + b_2(a\omega)^2 + b_3(a\omega)^3}. \tag{8.36}$$

Finally, the Padé approximation and numerical data are contrasted for imaginary $a\omega$.

In the Padé formula (8.36), the numerator is one degree higher than the denominator. This selection is made because Teukolsky's angular equation falls within the category of differential equations for angular prolate spheroidal wave functions. The behavior of the angular eigenvalues for large $a\omega$, as associated with this type of equation, is well-documented [18].

Fitting simulations have been conducted for various values of the angular parameter a and for several combinations of the spherical harmonic parameters l and m, consistently yielding accurate results when compared with those obtained by Leaver. I demonstrate the accuracy of our Padé approximation for $m = 0$ and $l = 2$, examining both the real and imaginary components of λ. My fitting procedure utilized the software package "gnufit". Details of the fit parameters for $m = 0$ are presented in Table 8.1, while Tables 8.2 and 8.3 display the corresponding results for $m = \pm 1$.

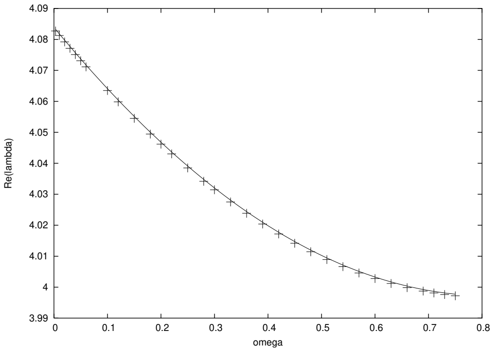

Figure 8.2: Real part of λ for $\hat{a} = 0.1$

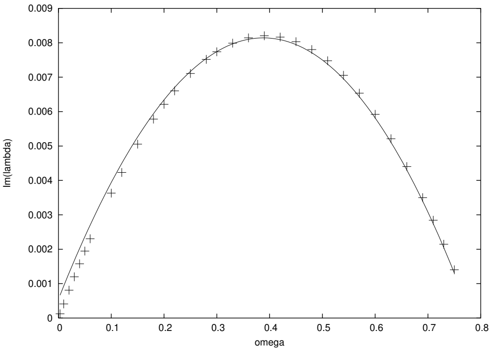

Figure 8.3: Imaginary part of λ for $\hat{a} = 0.1$

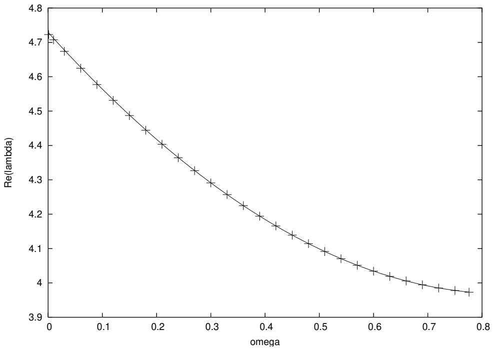

Figure 8.4: Real part of λ for $\hat{a} = 0.3$

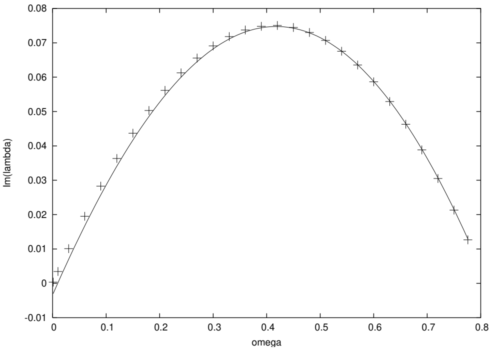

Figure 8.5: Imaginary part of λ for $\hat{a} = 0.3$

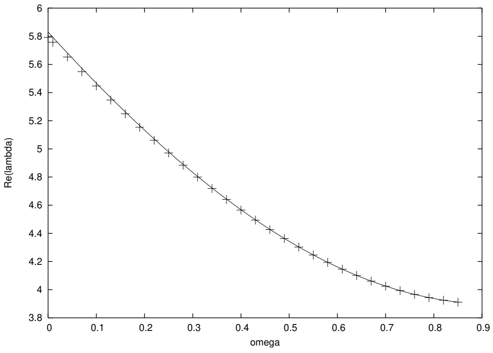

Figure 8.6: Real part of λ for $\hat{a} = 0.5$

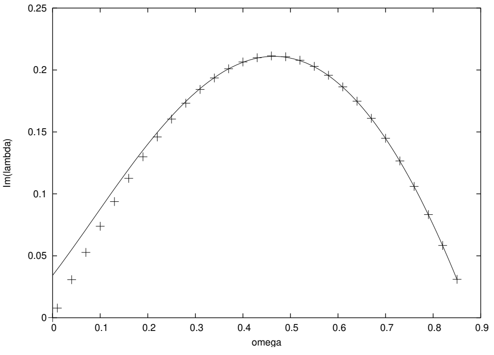

Figure 8.7: Imaginary part of λ for $\hat{a} = 0.5$

$\hat{a}$	a_0	a_1	a_2	a_3	a_4	b_1	b_2	b_3
0.0	4.0	0.0	0.0	0.0	0.0	0.0	0.0	0.0
0.1	4.0	-0.2979	-0.3994	0.0420	-0.0294	-0.0744	0.0310	0.0009
0.2	4.0	-0.3127	-0.3939	0.0434	-0.03	-0.0781	0.0323	0.0008
0.3	4.0	-0.5886	-0.2857	0.0679	-0.0396	-0.1470	0.0588	-0.0009
0.4	4.0	-0.5284	-0.2889	0.0619	-0.04038	-0.1320	0.0582	-0.0008
0.49	4.0	-0.5378	-0.2872	0.0627	-0.0404	-0.1343	0.0586	-0.00086

Table 8.1: This table displays the parameters obtained through fitting the Padé approximation for λ, based on numerical data generated by a computer program computing the angular eigenvalues of the Teukolsky equation, specifically for $m = 0$.

$\hat{a}$	a_0	a_1	a_2	a_3	b_1	b_2
0.0	4.0	0.0	0.0	0.0	0.0	0.0
0.1	4.0	0.8550	-0.8523	0.0792	-0.1195	-0.0289
0.2	4.0	2.2571	-0.4582	-0.0919	0.2284	-0.0380
0.3	4.0	2.8878	-0.3198	-0.1651	0.3838	-0.0483
0.4	4.0	3.2568	-0.2402	-0.2078	0.4747	-0.0546
0.49	4.0	3.2944	-0.2335	-0.2118	0.4838	-0.0553

Table 8.2: This table presents the parameters derived from fitting the Padé approximation for λ to the numerical output generated by a computer program computing the angular eigenvalues of the Teukolsky equation, specifically for $m = -1$.

$\hat{a}$	a_0	a_1	a_2	a_3	b_1	b_2
0.0	4.0	0.0	0.0	0.0	0.0	0.0
0.1	4.0	-4.1751	0.5889	0.2868	-0.7104	0.0543
0.2	4.0	-2.1949	-0.2201	0.0469	-0.2151	0.0163
0.3	4.0	-2.7029	-0.0173	0.1112	-0.3423	0.0252
0.4	4.0	-2.5610	-0.0748	0.0937	-0.3068	0.0226
0.49	4.0	-2.7425	-0.0014	0.1161	-0.3522	0.0258

Table 8.3: This table displays the parameters obtained by fitting the Padé approximation for λ to the numerical results obtained from a computer program computing the angular eigenvalues of the Teukolsky equation, specifically for $m = +1$.

8.2.2 Radial equation and numerical results

Due to the adoption of the new method, the concern regarding the angular equation and its eigenvalues has been alleviated. Consequently, we can now focus our numerical efforts on the radial equation. Similar to our approach with the angular equation, our priority lies in efficiently representing the radial continued fraction (8.33). It is advantageous in this scenario to consider the nth inversion of the radial continued fraction, expressed as:

$$0 = \left[\hat{\beta}_n - \frac{\hat{\alpha}_{n-1}\hat{\gamma}_n}{\hat{\beta}_{n-1}-}\frac{\hat{\alpha}_{n-2}\hat{\gamma}_{n-1}}{\hat{\beta}_{n-2}-}\cdots\frac{\hat{\alpha}_0\hat{\gamma}_1}{\hat{\beta}_0}\right] - \left[\frac{\hat{\alpha}_n\hat{\gamma}_{n+1}}{\hat{\beta}_{n+1}-}\frac{\hat{\alpha}_{n+1}\hat{\gamma}_{n+2}}{\hat{\beta}_{n+2}-}\cdots\right], \tag{8.37}$$

Because the nth quasinormal frequency is typically the most stable root of the nth inversion [14], I focus on this approach. I employ Lentz's method for both the finite and infinite fractions in equation (8.37). Subsequently, I developed another straightforward computer program, akin to the one utilized for the angular equation, capable of approximating the sum in (8.37) and simultaneously computing its roots. This program incorporates the Padé rational function to represent the angular eigenvalues present in (8.33). Consequently, the roots obtained from this method correspond to the Kerr quasinormal frequencies under investigation.

This innovative approach enables us to match or exceed previous results up to the ninth mode [14, 15].

Fig. 8.8 presents several plots illustrating the distribution of quasinormal frequencies across different angular parameters $\hat{a}$, spanning from $\hat{a} = 0.1$ to $\hat{a} = 0.49$, closely approaching the Kerr limit. The top left panel depicts the frequencies for $\hat{a} = 0.0$, $l = 2$, and $m = 0$, representing the classical outcome for Schwarzschild black holes, as documented in references such as [19] and [20].

Fig. 8.9 illustrates the modes in closer detail, each parameterized by the rotation parameter a. Notably, it's evident that the ninth mode begins on the imaginary axis, consistent with expectations.

In Fig. 8.10, I present a detailed view of the curve depicting the fifth mode for $m = \pm 1$, demonstrating the complex conjugate symmetry of the Kerr quasinormal frequencies. This figure reaffirms the accuracy of our technique in reproducing

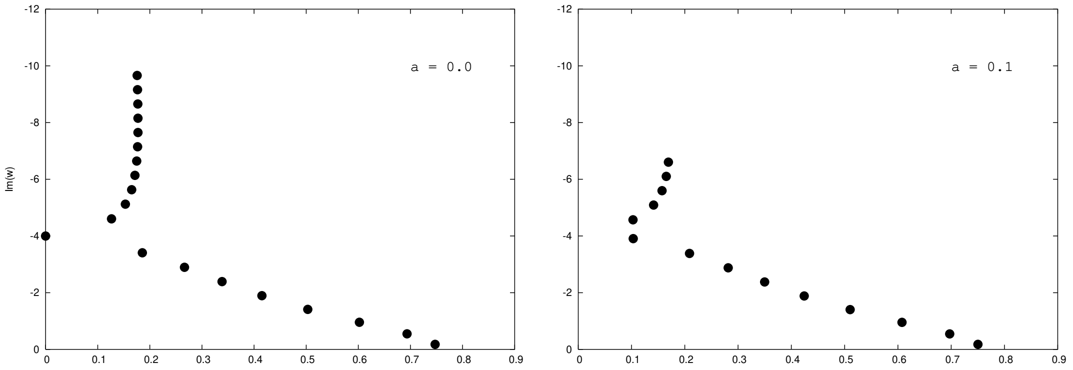

(a) $\hat{a} = 0.0$ (b) $\hat{a} = 0.1$

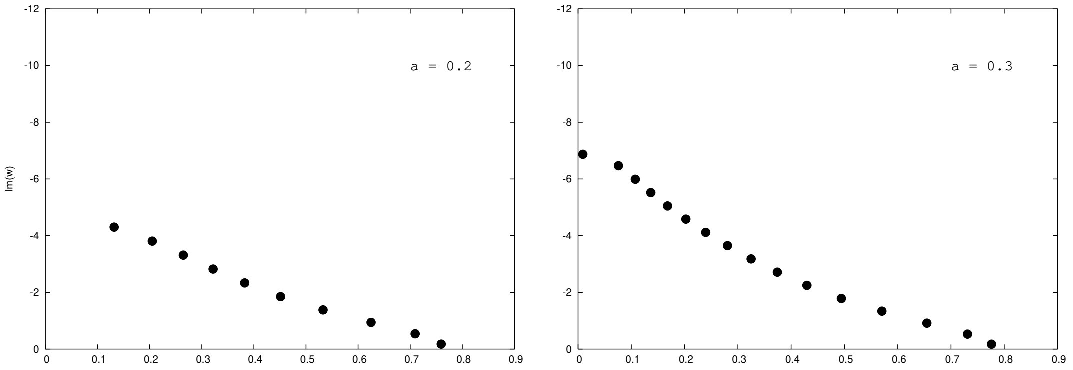

(c) $\hat{a} = 0.2$ (d) $\hat{a} = 0.3$

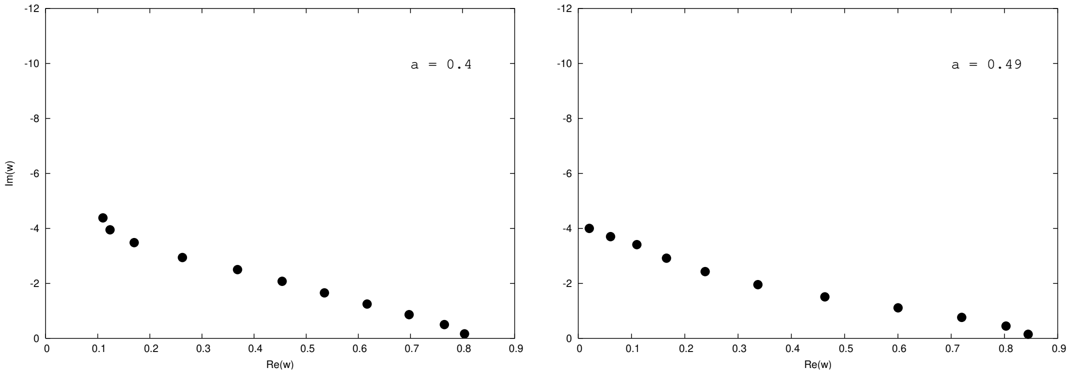

(e) $\hat{a} = 0.4$ (f) $\hat{a} = 0.49$

Figure 8.8: The initial quasinormal frequencies for $l = 2$ and $m = 0$, scaled by $2M$, are depicted in the complex plane. Each panel showcases a distinct angular momentum per unit mass $\hat{a}$, spanning from 0.0 to M, nearing the Kerr limit.

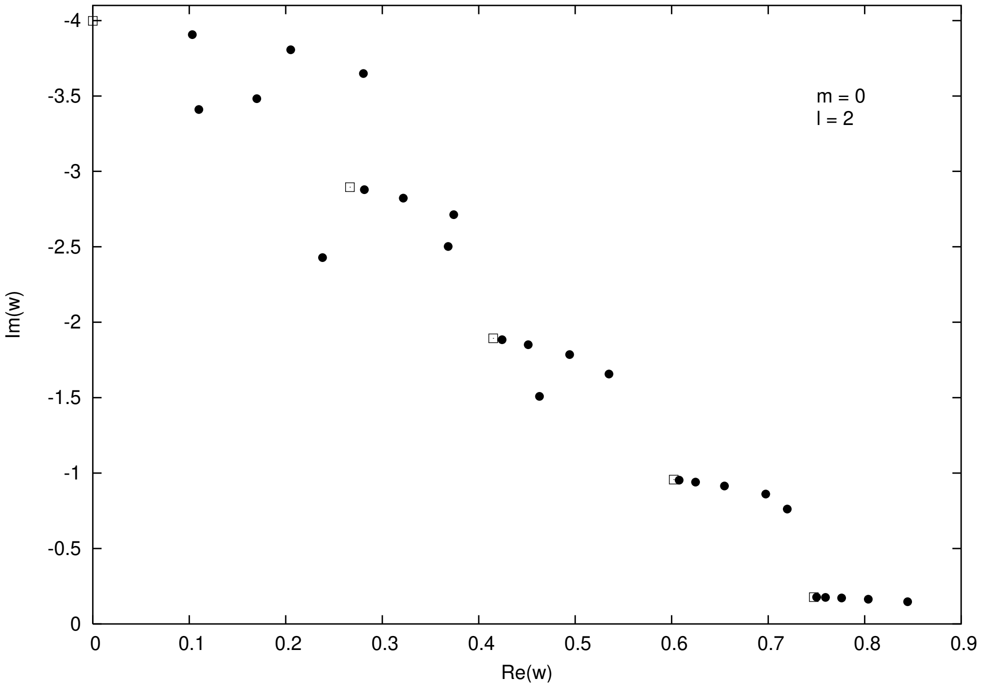

Figure 8.9: The depicted modes include the first, third, fifth, seventh, and ninth quasinormal modes associated with $l = 2$ and $m = 0$, all scaled by $2M$. These modes vary with the rotation parameter $\hat{a}$, ranging from $\hat{a} = 0$ at the upper left end (represented by squares) to $\hat{a} = 0.49$ at different positions. Intermediate dots correspond to $\hat{a} = 0.1, 0.2, 0.3, 0.4$. Notably, the ninth mode lies on the imaginary axis when $\hat{a} = 0.0$, exhibiting the expected behavior as it progresses.

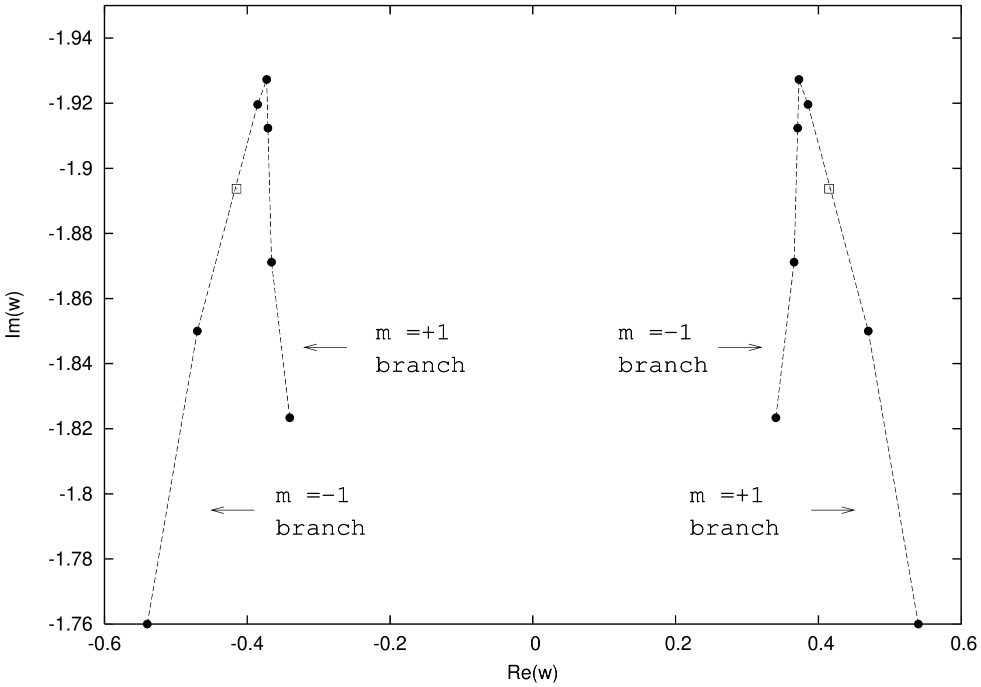

Figure 8.10: We plot a detailed view of the curve depicting the fifth mode for $m = \pm 1$. Additionally, we demonstrate the complex conjugate relationship of the Kerr quasinormal frequencies, where squares denote the complex conjugate frequencies for $a = 0.0$.

Leaver's results. The peak observed for $m = -1$ and angular parameter $\hat{a}$ ranging from zero to the Kerr limit confirms a similar behavior found by Leaver.

$\hat{a}$	$\hat{\omega}_1$	$\hat{\omega}_2$	$\hat{\omega}_3$	$\hat{\omega}_4$	$\hat{\omega}_5$
0.0	(0.747343, -0.177925)	(0.693422, -0.547829)	(0.602107, -0.956555)	(0.503011, -1.4103)	(0.415028, -1.89369)
0.1	(0.750252, -0.177401)	(0.697296, -0.546029)	(0.607671, -0.952749)	(0.510396, -1.40365)	(0.424195, -1.88378)
0.2	(0.75936, -0.175653)	(0.709343, -0.540027)	(0.624762, -0.940155)	(0.532732, -1.38181)	(0.451287, -1.85134)
0.3	(0.776104, -0.17199)	(0.731061, -0.527509)	(0.654649, -0.914241)	(0.57023, -1.33741)	(0.494169, -1.78589)
0.4	(0.803834, -0.164314)	(0.765136, -0.501476)	(0.6975, -0.86143)	(0.616905, -1.24857)	(0.535028, -1.65631)
0.49	(0.844509, -0.147065)	(0.802873, -0.446104)	(0.7198, -0.7616)	(0.60027, -1.11018)	(0.462988, -1.50839)

Table 8.4: Numerical values of the first five Kerr quasinormal frequencies for $l = 2$, $m = 0$, ranging from $\hat{a} = 0.0$ to 0.49.

In Table 8.4, I present the numerical results of Kerr quasinormal frequencies for $l = 2$ and $m = 0$, calculated using our updated method. It's worth noting that the values of the primary modes closely align with those from Leaver's analysis, as evidenced by the comparison in Table 8.5

$\hat{a}$	Leaver's fund. mode	Our fund. mode
0.0	(0.747343, -0.177925)	(0.747343, -0.177925)
0.1	(0.750248, -0.177401)	(0.750252, -0.177401)
0.2	(0.759363, -0.175653)	(0.75936, -0.175653)
0.3	(0.766108, -0.171989)	(0.776104, -0.17199)
0.4	(0.803835, -0.164313)	(0.803834, -0.164314)
0.49	(0.844509, -0.147065)	(0.844509, -0.147065)

Table 8.5: In this table, I present a comparison between our fundamental mode and Leaver's results for $l = 2$ and $m = 0$, illustrating their close similarity.

9

A detailed study of quasi-normal frequencies of Kerr Sen black hole

9.1 Kerr Sen Spacetime

In 1992, Sen derived a solution for a four-dimensional black hole with charge and rotation within the low-energy approximation of heterotic string theory. The effective action governing this scenario in four dimensions is detailed in the literature [21].

$$S = \int d^4x \sqrt{|\tilde{g}|} e^{-\Phi} \left(R - \frac{1}{8} F_{\mu\nu} F^{\mu\nu} + \tilde{g}^{\mu\nu} \partial_\mu \Phi \partial_\nu \Phi - \frac{1}{12} H_{\kappa\lambda\mu} H^{\kappa\lambda\mu} \right) \tag{9.1}$$

Here, $\tilde{g}$ represents the determinant of the tensor metric $\tilde{g}_{\mu\nu}$, where the spacetime metric in the Einstein frame $g_{\mu\nu}$ and the string metric $\tilde{g}_{\mu\nu}$ are connected through the relation $g_{\mu\nu} = e^{-\Phi}\tilde{g}_{\mu\nu}$. In this context, R stands for the scalar curvature, Φ denotes the dilaton field, and $F_{\mu\nu}$ represents the field-strength tensor $F_{\mu\nu} = \partial_\mu A_\nu - \partial_\nu A_\mu$. Here, A_ν denotes the electromagnetic 4-vector potential of the charged black hole, while $H_{\kappa\lambda\mu}$ represents the third-rank tensor field,

$$H_{\kappa\mu\nu} = \partial_\kappa B_{\mu\nu} + \partial_\nu B_{\kappa\mu} + \partial_\mu B_{\nu\kappa} - \frac{1}{4}\left(A_\kappa F_{\mu\nu} + A_\nu F_{\kappa\mu} + A_\mu F_{\nu\kappa}\right) \tag{9.2}$$

$B_{\nu\sigma}$ represents a second-rank antisymmetric tensor gauge field. Sen utilized a transformation on the Kerr solution, originally a vacuum Einstein equation solution, yielding the charged rotating black hole solution dubbed the Kerr-Sen solution within the theory (9.1). In Boyer-Lindquist coordinates (t, r, θ, ϕ), the Kerr-Sen metric in the Einstein frame can be expressed as:

$$\begin{aligned} ds^2 &= -\left(1 - \frac{2\mathcal{M}r}{\Sigma}\right)dt^2 + \Sigma\left(\frac{dr^2}{\Delta_{KS}} + d\theta^2\right) - \frac{4\mathcal{M}ra}{\Sigma}\sin^2\theta dt d\phi \\ &\quad + \left(\Sigma + a^2\sin^2\theta + \frac{2\mathcal{M}ra^2\sin^2\theta}{\Sigma}\right)\sin^2\theta d\phi^2, \end{aligned} \tag{9.3}$$

where

$$b = \frac{Q^2}{2\mathcal{M}} \tag{9.4}$$

$$\Delta_{KS} = r(r + 2b) - 2\mathcal{M}r + a^2 \tag{9.5}$$

$$\Sigma = r(r + 2b) + a^2\cos^2\theta. \tag{9.6}$$

Indeed, r_+ and r_- denote the outer and inner horizons of the black hole, respectively, defined as:

$$r_\pm = \mathcal{M} - b \pm \sqrt{(\mathcal{M} - b)^2 - a^2}. \tag{9.7}$$

The existing elements of the Kerr-Sen contravariant tensor metric in the Einstein frame are:

$$\begin{aligned}
g^{tt} &= \frac{\Delta_{KS} a^2 \sin^2\theta - (r^2 + 2br + a^2)^2}{\Delta_{KS}\Sigma}, \; g^{rr} = \frac{\Delta_{KS}}{\Sigma} && (9.8)\\
g^{\theta\theta} &= \frac{1}{\Sigma}, \; g^{\phi\phi} = \frac{\Delta_{KS} - a^2 \sin^2\theta}{\Delta_{KS}\Sigma \sin^2\theta} && (9.9)\\
g^{t\phi} &= g^{\phi t} = -\frac{2\mathcal{M}ar}{\Delta_{KS}\Sigma}, && (9.10)
\end{aligned}$$

where $\sqrt{-g} = \Sigma \sin\theta$. The Kerr-Sen metric (9.3) characterizes a black hole possessing mass $\mathcal{M}$, electric charge Q, and angular momentum $J = \mathcal{M}a$. The solutions pertaining to non-gravitational fundamental fields within the theory specified by the action (9.1) are

$$\begin{aligned}
e^{-2\Phi} &= \frac{\Sigma}{r^2 + a^2 \cos^2\theta} && (9.11)\\
A_t &= -\frac{Qr}{\Sigma} && (9.12)\\
A_\phi &= \frac{Qra \sin^2\theta}{\Sigma} && (9.13)\\
B_{t\phi} &= \frac{bra \sin^2\theta}{\Sigma} && (9.14)
\end{aligned}$$

and the corresponding Hawking temperature, angular velocity, and electrostatic potential at the horizon are determined as:

$$
\begin{aligned}
T_H &= \frac{r_+ - r_-}{8\pi \mathcal{M} r_+} = \frac{\sqrt{(2\mathcal{M}^2 - Q^2)^2 - 4J^2}}{4\pi\mathcal{M}\left(2\mathcal{M}^2 - Q^2 + \sqrt{(2\mathcal{M}^2 - Q^2)^2 - 4J^2}\right)} && (9.15)\\
\Omega_H &= \frac{a}{2\mathcal{M} r_+} = \frac{J}{\mathcal{M}\left(2\mathcal{M}^2 - Q^2 + \sqrt{(2\mathcal{M}^2 - Q^2)^2 - 4J^2}\right)} && (9.16)\\
\Phi_H &= \frac{Q}{2\mathcal{M}} && (9.17)
\end{aligned}
$$

9.2 Quasi-Normal Modes (QNMs) of the Kerr-Sen Black Hole

9.2.1 perturbation of the scalar field

Examining a massless scalar field denoted as Φ within the Kerr-Sen spacetime, it obeys the Klein-Gordon equation

$$\frac{1}{\sqrt{-g}}\partial_\alpha(g^{\alpha\beta}\sqrt{-g}\partial_\beta\Phi) = 0. \tag{9.18}$$

In Teukolsky's research [9], it is demonstrated that all scalar fields satisfying $\nabla^2\Phi = 0$ can be separated in Boyer-Lindquist coordinates. Consequently, for the scalar field $\Phi(t, r, \theta, \varphi)$ within the Kerr-Sen spacetime, we can express it as:

$$\Phi = e^{-i\omega t} e^{im\varphi} R(r) S(\theta), \tag{9.19}$$

In the eikonal limit, the functions $R(r)$ and $S(\theta)$ adhere to the subsequent equations.

$$\frac{1}{\sin\theta}\frac{d}{d\theta}\left(\sin\theta\frac{dS(\theta)}{d\theta}\right)+\left(a^2\omega^2 cos^2\theta-\frac{m^2}{\sin^2\theta}+A_{\ell m}\right)S(\theta) = 0 \quad (9.20)$$

$$\frac{d}{dr}\left(\Delta_{KS}\frac{dR(r)}{dr}\right)+\left(\frac{(r(r+2b)+a^2)^2}{\Delta_{KS}}+2am\omega-A_{\ell m}\right)R(r) = 0 \quad (9.21)$$

Here, m represents the azimuthal quantum number, while $A_{\ell m}$ signifies the angular eigenvalue, which is dependent on ω. As the parameters a and b approach zero (the Schwarzschild limit), the angle eigenvalue simplifies to $A_{\ell m} = \ell(\ell+1)$ (Discussed earlier in Section 8.2). Typically, the expression for $A_{\ell m}$ is intricate, allowing for separation into real and imaginary parts [22]

$$A_{\ell m} = A^R_{\ell m} - iA^I_{\ell m} \quad (9.22)$$

Eq. (9.20) must adhere to the Bohr-Sommerfeld quantization criterion [22]

$$\int_{\theta_-}^{\theta_+}\sqrt{a^2\omega_R^2 cos^2\theta-\frac{m^2}{sin^2\theta}+A^R_{\ell m}}d\theta = (L-\mid m\mid)\pi. \quad (9.23)$$

In this instance, we set L as $\ell + 1/2$ following [22]. Symbols $\theta_\pm$ denote the turning point and the zero point of the potential, respectively. Referring to the angular equation Eq.(9.20), and we redefine variables as $dx = d\theta/\sin\theta$ and $x = \log(\tan(\theta/2))$ to express Eq.(9.20) differently

$$\frac{d^2S(\theta)}{dx^2}+(a^2\omega_R^2 cos^2\theta sin^2\theta - m^2 + A^R_{\ell m} sin^2\theta)S(\theta) = 0. \quad (9.24)$$

Eq.(9.20) possesses two regular singular points, $cos\theta = +1$ and $cos\theta = -1$. The stipulated boundary condition for Eq.(9.20) is that S_θ remains finite at these singular points. In line with E. W. Leaver's approach [14], a solution to Eq.(9.20) can be formulated as:

$$S_\theta = e^{a\omega cos\theta}(1+cos\theta)^{\frac{|m|}{2}}(1-cos\theta)^{\frac{|m|}{2}}\sum_{n=0}^{\infty} a_n(1+cos\theta)^n. \tag{9.25}$$

Through the substitution of Eq. (9.25) into Eq. (9.20), a three-term recurrence relation can be derived:

$$\alpha_0 a_1 + \beta_0 a_0 = 0 \tag{9.26}$$

$$\alpha_n a_{n+1} + \beta_n a_n + \gamma_n a_{n-1} = 0, \quad n = 1, 2\cdots \tag{9.27}$$

For a given a and m, solving the continued fraction equation yields ω_R and $A_{\ell m}$. Remarkably, this equation shares the same form and recurrence coefficients as those in the Kerr black hole scalar field case [14], owing to similar equation forms and boundary conditions. Consequently, the angular separation constant $A_{\ell m}$ for the KS black hole scalar field equation can be determined using the methodologies outlined in [22, 23]. Particularly, in the eikonal limit where $\ell \gg 1$, treating $a\omega_R$ as small allows the expansion of $A^R_{\ell m}$ as a Taylor series [14],

$$A^R_{\ell m} = \sum_{p=0}^{\infty} f_p(a\omega_R)^p \approx f_0 + f_2(a\omega_R)^2 + O(a\omega_R)^4 \approx L^2 + \frac{1}{2}(\frac{m^2}{L^2} - 1)a^2\omega_R^2 \tag{9.28}$$

9.3 The relationship between Quasinormal Modes (QNMs) and the shadow radius.

By equating the massless scalar field Φ with the dominant component of the principal function (C.2), we can express it as:

$$\Phi = e^{iS} = e^{-iEt} e^{iL_z \phi} e^{iS_\theta} e^{iS_r} \tag{9.29}$$

Upon comparing Eq.(9.19) and Eq.(9.29), it becomes apparent that

$$E = \omega_R, \quad L_z = m \tag{9.30}$$

Furthermore, upon examining equations (C.3), (9.20), and (9.24), and applying as employed in Ref. [22], we can additionally identify that

$$\mathcal{D} = A^R_{\ell m} - m^2 \tag{9.31}$$

For conventional Quasinormal Modes (QNMs), it can be formulated as per [22]

$$\omega = (\ell + \frac{1}{2})\Omega_R(\mu) - i(n + \frac{1}{2})\Omega_I(\mu) \tag{9.32}$$

with $\mu \equiv m/(\ell + 1/2)$ and $\Omega_R \equiv \omega_R/L$ In the context of a rotating black hole, a new angle $\Delta\varphi_{prec}$ is introduced, as discussed in [22], symbolizing the Lense-Thirring precession frequency due to the black hole's rotation [22]. If we designate T_θ as the period of motion in the θ direction, then the associated precession frequency Ω_{prec} can be expressed as:

$$\Omega_{prec} = \frac{\Delta\varphi_{prec}}{T_\theta} \tag{9.33}$$

In the context of a rotating black hole, the real component of the frequency can be represented as per [24]

$$\Omega_R = \Omega_\theta(\mu) + \mu\Omega_{prec}(\mu) \tag{9.34}$$

here $\Omega_\theta = 2\pi/T_\theta$. When contemplating a full cycle of the photon orbit in the θ direction

$$\delta S = L_z\Delta\varphi - ET_\theta + \delta S_\theta = 0, \tag{9.35}$$

Here, $\Delta\varphi$ denotes the azimuthal change following the completion of a cycle in the given direction; it correlates with $\Delta\varphi_{prec}$ through,

$$\Delta\varphi = \Delta\varphi_{prec} + 2\pi sgn(L_z) \tag{9.36}$$

The function sgn(.) determines the sign of its argument. Regarding δS_θ, when examined alongside Eq.(9.23), it leads to the equation:

$$\delta S_\theta = 2\int_{\theta_-}^{\theta_+} \sqrt{\Theta} d\theta = 2\int_{\theta_-}^{\theta_+} \sqrt{\mathcal{D} - cos^2\theta\left(\frac{L^2}{sin^2\theta} - a^2E^2\right)} d\theta = 2\pi(L - L_z) \tag{9.37}$$

By merging equations (9.30), (9.33), (9.37), we have determined that

$$\frac{L}{E} = \frac{1}{\Omega_\theta + \mu\Omega_{prec}} = \frac{1}{\Omega_R} \tag{9.38}$$

When replacing $\mathcal{D} = A^R_{\ell m} - m^2$ into Eq.(9.28), under the condition of large ℓ, an equation arises:

$$\frac{\sqrt{\mathcal{D}+L_z^2}}{E} \approx R_s \tag{9.39}$$

Furthermore, by comparing equations (9.28), (9.31), and (9.39), we can derive:

$$\begin{aligned} \frac{L^2}{E^2} &= \frac{\mathcal{D}+L_z^2}{E^2} + \frac{a^2}{2}\left(1-\frac{m^2}{L^2}\right) \qquad (9.40) \\ &\approx R_s^2 + \frac{a^2}{2}\left(1-\frac{m^2}{L^2}\right) \qquad (9.41) \end{aligned}$$

Gathering all components, the link between the real component of the Quasinormal Modes (QNMs) and the shadow radius R_s^+ and R_s^- is depicted in [25] as

$$\omega_R = \frac{1}{2}\left(\omega_{R^+} - \omega_{R^-}\right) \tag{9.42}$$

where $\omega_{R^\pm}$ is

$$\omega_{R^\pm} = \pm\frac{\ell+\frac{1}{2}}{\sqrt{(R_s^\pm)^2+\frac{a^2}{2}(1-\mu^2)}} \tag{9.43}$$

For limit $\ell \gg 1$ and $m \pm \ell$ i.e. $\mu \to 1$ we get $\omega_{R^\pm} \approx \frac{\ell}{R_s^\pm}$

10

Conclusion

Throughout this thesis, I have delved into the intricate realm of Anti-de Sitter (AdS) black holes, focusing particularly on the significant role played by quasinormal modes (QNMs) in understanding their dynamic behavior. My exploration has encompassed both analytical and numerical investigations, shedding light on various aspects of AdS black holes and their astrophysical implications.

The analytic calculation of QNMs has been a central focus of our research. By discussing both high overtones and low frequencies, I have elucidated the profound connections between perturbations of black holes in asymptotically AdS space and the dynamics of strongly coupled gauge theories.

Of particular interest are the quasinormal frequencies associated with gravitational perturbations of Kerr black holes, which have been extensively studied due to their astrophysical significance. My research has introduced a novel technique for computing these frequencies, circumventing the challenges posed by traditional numerical methods. However, a viable method involves thoroughly plotting the complete zero contours of all system functions, which comprise an unspecified quantity of separate closed curves. The points where these curves intersect represent the roots. The new technique consists of a new numerical way to evaluate the angular eigenvalues of the Teukolsky angular equation, which is independent of the solution of the radial part of the problem. By accurately evaluating the angular eigenvalues of the Teukolsky angular equation, my approach offers insights into the behavior of rotating black holes across a range of parameters.

Furthermore, I have explored the intriguing connections between the shadow radius and the real part of QNMs of Kerr-Sen black holes in the eikonal limit. Through a comprehensive analysis of massless scalar field perturbations and the Hamilton-Jacobi function, I have established a correspondence relation between QNMs and shadow radius, facilitating the calculation of QNMs through shadow radius. My findings support earlier conclusions and suggest opportunities for future investigation, such as expanding numerical computations to higher modes or formulating analytical expressions for the asymptotic tendencies of Kerr QNFs.

In conclusion, my research contributes to a deeper understanding of AdS black holes and their implications for theoretical physics and astrophysics. By uncovering new insights into the behavior of quasinormal modes and their connections with fundamental physical phenomena, I pave the way for future explorations in this captivating field.

A

Appendix A

A.1 $S_P = S_{NG}$ at Classical Level

To see Polyakov's action is equivalent to Nambu-Goto's action at the classical level, note that the world-sheet stress-energy tensor is defined as:

$$T_{ab} = -4\pi \frac{\delta S_P}{\sqrt{-\gamma}\delta\gamma^{ab}} \tag{A.1}$$

Since $\delta S_P = 0$ for variations around the classical solution (on-shell), the equation of motion for γ^{ab} is $T_{ab} = 0$. Using:

$$\delta\sqrt{-\gamma} = -\frac{1}{2}\sqrt{-\gamma}\gamma_{ab}\delta\gamma^{ab} \tag{A.2}$$

then the stress-energy tensor can be found:

$$\begin{aligned}\left(\int_\Sigma d^2\sigma\right)^{-1}\delta S_P &= -\frac{1}{4\pi\alpha'}\left(\delta\sqrt{-\gamma}\gamma^{ab}h_{ab} + \sqrt{-\gamma}\delta\gamma^{ab}h_{ab}\right)\\ &= \frac{1}{4\pi\alpha'}\sqrt{-\gamma}\left(\frac{1}{2}\gamma_{ab}\gamma^{cd}h_{cd} - h_{ab}\right)\delta\gamma^{ab}\end{aligned} \tag{A.3}$$

$$\Rightarrow T_{ab} = \frac{1}{\alpha'}\left(\frac{1}{2}\gamma_{ab}\gamma^{cd}h_{cd} - h_{ab}\right) \tag{A.4}$$

$$= \frac{1}{\alpha'}G_{\mu\nu}\left(\frac{1}{2}\gamma_{ab}\gamma^{cd}\partial_c X^\mu\partial_d X^\nu - \partial_a X^\mu\partial_b X^\nu\right) = 0 \tag{A.5}$$

This means $\gamma^{ab} = Bh^{ab}$, with $B = B(\sigma,\tau)$ can be arbitrary. Integrate out the world-sheet intrinsic metric field γ^{ab}:

$$\begin{aligned}S_P\left[\gamma^{ab} = Bh^{ab}, X^\mu\right] &= \frac{1}{4\pi\alpha'}\int_\Sigma d^2\sigma\left(B^{-1}\sqrt{-h}\right)\left(Bh^{ab}\right)\left(h_{ab}\right)\\ &= \frac{1}{2\pi\alpha'}\int_\Sigma d^2\sigma\sqrt{-h} = S_{NG}\left[X^\mu\right]\end{aligned} \tag{A.6}$$

B

Appendix B

B.1 Asymptotic Limit of Bessel Functions

We may consider the following asymptotic expansion of Bessel functions

$$J_{\frac{j}{2}}(y) \sim \sqrt{\frac{2}{\pi z}}\cos(y \mp \alpha_{+}) \quad , \quad N_{\frac{j}{2}}(y) \sim \sqrt{\frac{2}{\pi z}}\sin(y \mp \alpha_{+}) \quad , \quad y \gg \pm 1, \tag{B.1}$$

where $\alpha_{\pm} = \frac{\pi}{4}(1 \pm j)$.

B.2 Appendix B.2

We evaluated the relevant limit $j \to 0, 2$ whenever it was clear, aiming to streamline the notation. Employing

$$\int_0^\infty dx\; x^{-\lambda} J_\mu(x) J_\nu(x) = \frac{\Gamma(\lambda)\Gamma\left(\frac{\nu+\mu+1-\lambda}{2}\right)}{2^\lambda \Gamma\left(\frac{-\nu+\mu+1+\lambda}{2}\right)\Gamma\left(\frac{\nu-\mu+1+\lambda}{2}\right)\Gamma\left(\frac{\nu+\mu+1+\lambda}{2}\right)}\ , \tag{B.2}$$

C

Appendix C

The Hamilton-Jacobi equation governing the geodesics of the Kerr-Sen black hole is described as

$$\frac{\partial S}{\partial \sigma} = -\frac{1}{2}\frac{\partial S}{\partial x^{\mu}}\frac{\partial S}{\partial x^{\nu}}, \tag{C.1}$$

In this context, S represents the principal function, while σ denotes an affine parameter. Referring to null geodesics, the associated principal function S is outlined in

$$S(t, r, \theta, \varphi) = -Et + S_r(r) + S_\theta(\theta) + L_z\varphi \tag{C.2}$$

By merging Eq.(C.1) and Eq.(C.2), we obtain two distinct components of the Hamilton-Jacobi equation,

$$S_r(r) = \pm \int \frac{R(r)}{\Delta_{KS}} dr, \quad S_\theta(\theta) = \pm \int \sqrt{\Theta(\theta)} d\theta \tag{C.3}$$

where,

$$R(r) = (aL_z - E(r(r+2b)+a^2))^2 - \Delta_{KS}((L_z - aE)^2 + \mathcal{D}) \tag{C.4}$$

$$\Theta(\theta) = \mathcal{D} - cos^2\theta \left(\frac{L_z^2}{sin^2\theta} - a^2E^2 \right) \tag{C.5}$$

C.1 Shadow Radius of Kerr Sen Black Hole

Shadow radii for KS Black hole [26] can be expressed as

$$\overline{R}_s = \frac{1}{2}(x(r_0^+) - x(r_0^-)) \tag{C.6}$$

where $x(r_0^\pm)$ is unstable photon orbits [25, 26] But shadow radii of a black hole can be expressed as $R_s = L_z/E$ so we get [25]

$$R_s^\pm = a \pm \sqrt{\frac{4b^3 + 8b^2 r_0^\pm + 5b(r_0^\pm)^2 + (r_0^\pm)^3}{M}} \tag{C.7}$$

Bibliography

1. Birmingham, D. Topological black holes in anti-de Sitter space. *Classical and Quantum Gravity* **16,** 1197–1205. ISSN: 1361-6382. doi:10.1088/0264-9381/16/4/009. `http://dx.doi.org/10.1088/0264-9381/16/4/009` (Jan. 1999).
2. Bizoń, P. & Rostworowski, A. Weakly Turbulent Instability of Anti–de Sitter Spacetime. *Physical Review Letters* **107.** ISSN: 1079-7114. doi:10.1103/physrevlett.107.031102. `http://dx.doi.org/10.1103/PhysRevLett.107.031102` (July 2011).
3. Musiri, S. & Siopsis, G. Asymptotic form of quasi-normal modes of large AdS black holes. *Physics Letters B* **576,** 309–313. ISSN: 0370-2693. doi:10.1016/j.physletb.2003.10.015. `http://dx.doi.org/10.1016/j.physletb.2003.10.015` (Dec. 2003).
4. Natario, J. & Schiappa, R. *On the Classification of Asymptotic Quasinormal Frequencies for d-Dimensional Black Holes and Quantum Gravity* 2005. arXiv: `hep-th/0411267 [hep-th]`.
5. Musiri, S., Ness, S. & Siopsis, G. Perturbative calculation of quasinormal modes of AdS Schwarzschild black holes. *Physical Review D* **73.** ISSN: 1550-2368. doi:10.1103/physrevd.73.064001. `http://dx.doi.org/10.1103/PhysRevD.73.064001` (Mar. 2006).
6. Cardoso, V., Konoplya, R. & Lemos, J. P. S. Quasinormal frequencies of Schwarzschild black holes in anti–de Sitter spacetimes: A complete study of the overtone asymptotic behavior. *Physical Review D* **68.** ISSN: 1089-4918. doi:10.1103/physrevd.68.044024. `http://dx.doi.org/10.1103/PhysRevD.68.044024` (Aug. 2003).
7. Kodama, H. & Ishibashi, A. A Master Equation for Gravitational Perturbations of Maximally Symmetric Black Holes in Higher Dimensions. *Progress of Theoretical Physics* **110,** 701–722. ISSN: 1347-4081. doi:10.1143/ptp.110.701. `http://dx.doi.org/10.1143/PTP.110.701` (Oct. 2003).
8. Regge, T. & Wheeler, J. A. Stability of a Schwarzschild Singularity. *Phys. Rev.* **108,** 1063–1069. doi:10.1103/PhysRev.108.1063. `https://link.aps.org/doi/10.1103/PhysRev.108.1063` (4 Nov. 1957).
9. Teukolsky, S. A. Rotating Black Holes: Separable Wave Equations for Gravitational and Electromagnetic Perturbations. *Phys. Rev. Lett.* **29,** 1114–1118. doi:10.1103/PhysRevLett.29.1114. `https://link.aps.org/doi/10.1103/PhysRevLett.29.1114` (16 Oct. 1972).
10. Chandrasekhar, S. The Mathematical Theory of Black Holes (1983).
11. Vishveshwara, C. V. Scattering of Gravitational Radiation by a Schwarzschild Black-hole. *Nature* **227,** 936–938. doi:10.1038/227936a0 (1970).
12. Press, W. H. Long Wave Trains of Gravitational Waves from a Vibrating Black Hole. *Astrophys. J. Lett.* **170,** L105–L108. doi:10.1086/180849 (1971).
13. Chandrasekhar, S. & Detweiler, S. The Quasi-Normal Modes of the Schwarzschild Black Hole. *Proceedings of the Royal Society of London. Series A, Mathematical and Physical Sciences* **344,** 441–452. ISSN: 00804630. `http://www.jstor.org/stable/78902` (2024) (1975).
14. Leaver, E. W. An Analytic representation for the quasi normal modes of Kerr black holes. *Proc. Roy. Soc. Lond. A* **402,** 285–298. doi:10.1098/rspa.1985.0119 (1985).

15. Onozawa, H. Detailed study of quasinormal frequencies of the Kerr black hole. *Phys. Rev. D* **55,** 3593–3602. doi:`10.1103/PhysRevD.55.3593`. `https://link.aps.org/doi/10.1103/PhysRevD.55.3593` (6 Mar. 1997).
16. Mino, Y., Sasaki, M., Shibata, M., Tagoshi, H. & Tanaka, T. Chapter 1. Black Hole Perturbation. *Progress of Theoretical Physics Supplement* **128,** 1–121. ISSN: 0375-9687. doi:`10.1143/ptps.128.1`. `http://dx.doi.org/10.1143/PTPS.128.1` (1997).
17. W. H. Press S. A. Teukolsky, B. P. F. & Vetterling, W. T. Numerical Recipes, The Art of Scientific Computing (Cambridge University Press, New York, 1986).
18. Abramowitz, M. Handbook of Mathematical Functions (Dover Publications, inc., New York, 1965).
19. Nollert, H.-P. Quasinormal modes of Schwarzschild black holes: The determination of quasinormal frequencies with very large imaginary parts. *Phys. Rev. D* **47,** 5253–5258. doi:`10.1103/PhysRevD.47.5253`. `https://link.aps.org/doi/10.1103/PhysRevD.47.5253` (12 June 1993).
20. Kokkotas, K. D. & Schmidt, B. G. Quasi-Normal Modes of Stars and Black Holes. *Living Reviews in Relativity* **2.** ISSN: 1433-8351. doi:`10.12942/lrr-1999-2`. `http://dx.doi.org/10.12942/lrr-1999-2` (Sept. 1999).
21. Sen, A. Rotating charged black hole solution in heterotic string theory. *Physical Review Letters* **69,** 1006–1009. ISSN: 0031-9007. doi:`10.1103/physrevlett.69.1006`. `http://dx.doi.org/10.1103/PhysRevLett.69.1006` (Aug. 1992).
22. Yang, H. *et al.* Quasinormal-mode spectrum of Kerr black holes and its geometric interpretation. *Physical Review D* **86.** ISSN: 1550-2368. doi:`10.1103/physrevd.86.104006`. `http://dx.doi.org/10.1103/PhysRevD.86.104006` (Nov. 2012).
23. Berti, E., Cardoso, V. & Casals, M. Eigenvalues and eigenfunctions of spin-weighted spheroidal harmonics in four and higher dimensions. *Phys. Rev. D* **73.** [Erratum: Phys.Rev.D 73, 109902 (2006)], 024013. doi:`10.1103/PhysRevD.73.109902`. arXiv: `gr-qc/0511111` (2006).
24. Yang, H. Relating Black Hole Shadow to Quasinormal Modes for Rotating Black Holes. *Phys. Rev. D* **103,** 084010. doi:`10.1103/PhysRevD.103.084010`. arXiv: `2101.11129 [gr-qc]` (2021).
25. Jusufi, K. Connection Between the Shadow Radius and Quasinormal Modes in Rotating Spacetimes. *Phys. Rev. D* **101,** 124063. doi:`10.1103/PhysRevD.101.124063`. arXiv: `2004.04664 [gr-qc]` (2020).
26. Feng, X.-H. & Lü, H. On the size of rotating black holes. *The European Physical Journal C* **80.** ISSN: 1434-6052. doi:`10.1140/epjc/s10052-020-8119-z`. `http://dx.doi.org/10.1140/epjc/s10052-020-8119-z` (June 2020).